GEOCHEMICAL ASSESSMENT AND RESOURCE POTENTIAL OF THE CRITICAL MINERALS IN SARDHAI FORMATION, PUNJAB, PAKISTAN

UMAR ZAMAN

09-262242-021

BAHRIA UNIVERSITY ISLAMABAD

GEOCHEMICAL ASSESSMENT AND RESOURCE POTENTIAL OF THE CRITICAL MINERALS IN SARDHAI FORMATION, PUNJAB, PAKISTAN

A thesis is submitted in fulfillment of the requirement for the award of the degree of Master of Science (Geology)

UMAR ZAMAN

09-262242-021

Department of Earth and Environmental Sciences

BAHRIA UNIVERSITY ISLAMABAD

JULY 2026

Bahria University

Department of Earth & Environmental Sciences
Islamabad Campus, Islamabad

Date: July 17, 2026

Certificate

A thesis submitted by **Mr. Umar Zaman** to the Department of Earth & Environmental Sciences, Bahria University, Islamabad in partial fulfillment of the requirements for the degree of **Master of Science in Geology** (Session **2024-2026**).

Committee Member	Name	Signature
Supervisor	Dr. Mumtaz Ali Khan	
Internal Examiner	Dr. Urooj Shakir	
External Examiner	Dr. Asghar Ali	
Post Graduate Coordinator	Dr. Muhammad Raiees Amjad	
Head of Department (E&ES)	Dr. Syed Umair Ullah Jamil	

APPROVAL OF EXAMINATION

Scholar's Name: "Umar Zaman"

Registration No: "72006"

Program of Study: MS Geology

Thesis Title: "GEOCHEMICAL ASSESSMENT AND RESOURCE POTENTIAL OF THE CRITICAL MINERALS IN SARDHAI FORMATION, PUNJAB, PAKISTAN"

It is to certify that the above scholar's thesis has been completed to my satisfaction and to my belief, its standard is appropriate for submission for examination. I have also conducted plagiarism test of this thesis using HEC prescribed software and found similarity index 7% that is within the permissible limit set by the HEC for the MS degree thesis. I have also found the thesis in a format recognized by the BU for the MS thesis.

NOTE: The Plagiarism report is attached at the end of thesis.

Supervisor's Signature:_____

Date:

Name: Dr. Mumtaz Ali Khan

AUTHOR'S DECLERATION

I, "Mr. Umar Zaman" is hereby stating that my MS thesis titled "GEOCHEMICAL ASSESSMENT AND RESOURCE POTENTIAL OF THE CRITICAL MINERALS IN SARDHAI FORMATION, PUNJAB, PAKISTAN" is my own work and has not been submitted previously by me of taking any degree from this university "Bahria University Islamabad Campus" or anywhere else in the country/world.

At any time if my statement is found to be incorrect even after my graduation, the University has the right to withdraw/cancel my MS degree.

Scholar Name: Umar Zaman

Sign: _____

Date:

PLAGIARISM UNDERTAKING

I solemnly declare that research work presented in the thesis titled "GEOCHEMICAL ASSESSMENT AND RESOURCE POTENTIAL OF THE CRITICAL MINERALS IN SARDHAI FORMATION, PUNJAB, PAKISTAN" is solely my research work with no significant contribution from any other person. Small contribution/help wherever taken has been duly acknowledged and that complete thesis has been written by me.

I understand the zero-tolerance policy of HEC and Bahria University towards plagiarism. Therefore, I as an Author of the above titled thesis declared that no portion of my thesis has been plagiarized, and any material used as reference is properly referred/ cited.

I understand that if, I am found guilty of any formal plagiarism in the above titled thesis even after award of MS degree, the university reserves the right to withdraw, revoke my MS degree and that HEC and the University has the right to publish my name on the HEC/University website on which names of the scholars are placed who submitted plagiarized thesis.

Scholar/Author's

Sign: _____

Name of the Scholar: Umar Zaman

DEDICATION

"This thesis is dedicated to my parents, who have always supported me through thick and thin".

ACKNOWLEDGEMENT

All glory and gratitude belong to Almighty Allah, the Most Gracious and the Most Merciful, whose boundless blessings, mercy, and divine guidance made the successful completion of this research possible. Without His grace, none of this work would have come to fruition.

I wish to extend my profound and sincere appreciation to my supervisor, Dr. Mumtaz Ali Khan, Associate Professor in the Department of Earth and Environmental Sciences at Bahria University, H-11 Campus, Islamabad, whose expert guidance, scholarly mentorship, and sustained intellectual support were instrumental at every stage of this research. His thoughtful feedback, patient counsel, and deep commitment to academic excellence not only shaped the direction of this thesis but also significantly broadened my understanding of the discipline in ways that will remain with me throughout my career.

I extend my sincere thanks to Mr. Imtiaz Khan, Environmental Sciences lab in charge, and Mr. Sajid, lab assistant, for their help in sample preparation.

I also appreciate Allama Iqbal Open University for providing access to analytical facilities and technical guidance that were essential to the sample analysis component of this study.

My deepest and most heartfelt gratitude is reserved for my parents and family, whose unconditional love, steadfast prayers, and unwavering moral support have been the foundation upon which every achievement of my academic journey has been built.

ABSTRACT

This study presents a geochemical characterization and mineral potential of the Sardhai Formation, an Early Permian clay dominated unit of the Nilawahan Group exposed within the Salt Range fold and thrust belt of Pakistan. Twenty-two clay samples collected from two outcrop localities near Kallar Kahar were analyzed by inductively coupled plasma mass spectrometry to evaluate the formation's critical mineral inventory. Because the unit is lithologically uniform, the dataset offers a controlled framework in which elemental variability can be attributed primarily to post depositional processes rather than primary depositional differences. Results show mean values of; lithium (0.26398 ppm), vanadium (1.06501 ppm), manganese (2.19484 ppm), beryllium (0.04840 ppm), gallium (0.12050 ppm), niobium (0.07946 ppm), nickel (0.11183 ppm), chromium (0.34034 ppm), zirconium (0.03512 ppm), hafnium (0.00723 ppm), titanium (0.35212 ppm), the light rare earth elements (0.56496 ppm), and lastly uranium at (0.28650 ppm), they occur at the highest and are most consistently quantifiable concentrations. Non oxidized samples consistently retain higher concentrations of these elements than their oxidized counterparts, indicating that oxidative weathering, structurally driven fluid rock interaction, and the formation's position within the fold and thrust belt, rather than original sedimentary composition, govern present day critical mineral distribution. One sample constitutes a distinct multi element, rare earth enriched anomaly. Despite these detectable patterns, absolute concentrations remain below economic threshold throughout, and the dataset is best characterized as reconnaissance level rather than indicative of economic mineralization. The findings nonetheless demonstrate that fine grained clay successions in the Salt Range can act as meaningful repositories of critical elements and establish a baseline for future investigation. Recommended follow up work includes denser, non-oxidized patch focused sampling, clay phase identification, sequential extraction, fluid inclusion and isotopic studies, and structural mapping, all of which are necessary before any assessment of resource potential can be responsibly made.

TABLE OF CONTENTS

LIST OF FIGURES

LIST OF TABLES

LIST OF ABBREVEATIONS

Above Detection Limit	(ADL)
Below Detection Limit	(BDL)
Department of Energy	(DOE)
Khushab Roadside Section	(KRSS)
Peeran-e-Morjhang Roadside Section	(PMJRSS)
The International Energy Agency	(IEA)
The United Nations Environment Program	(UNEP)
Umar Sample 1-Umar Sample 22	(US1-US22)
United States Geological Survey	(USGS)

CHAPTER 1
INTRODUCTION

1.1 General statement

Lying between two major river systems, the Jhelum River to the east and the Indus River to the west, the Salt Range represents a well defined, elongated trough striking in an east west direction. Its geographic coordinates range from 32°15′ to 33°0′ N in latitude and 71°34′ to 73°45′ E in longitude. It represents the southward verging frontal thrust of the northwestern Himalayan fold and thrust belt and is considered as one of the most extensively studied and documented geological provinces in the history of Pakistan. It lies south of the Potwar Plateau, the range is a sharp rise of the Punjab plains and reveals a great range of stratigraphic successions in a timeline extending back to the Precambrian era up to the very recent. Its geological history is inseparably connected with the convergence that happened between Indian Plate and Eurasian Plate, a collision that initiated moving forward in the Paleogene time, and whose impact persists to this day to form and shape the tectonic structure of South Asia. With compressional stresses transported southward of the collision, the strain was passed on to the foreland basin creating a structurally complex (mechanically coherent) thin skinned fold and thrust system in which the sedimentary strata were stripped out along weak evaporite sequences (Gee, 1989).

The stratigraphy shows that the Salt Range has a complete set of sedimentary successions. The Precambrian evaporites are superimposed by the Cambrian shallow marine sediments and carbonates and the overburden is the Permian glacial and postglacial suites tracing the Gondwainan paleogeography. The sequence of strata of the Mesozoic era records periods of the sea and of the land, and the Paleogene and Neogene follow the sediment of the foreland basins, which are directly correlated with the uplift of the Himalayas. Significant deviations are noted in this succession, and it is the transition of trends in tectonic reorganizations and changes in depositional regimes. The Miocene to Pliocene molasse deposits of the Siwalik Group

are used to represent the rapid clastic influx in the period of peak uplift of the Himalayas and show how a combination of tectonics and sedimentation processes occurred in foreland systems (Gee, 1989).

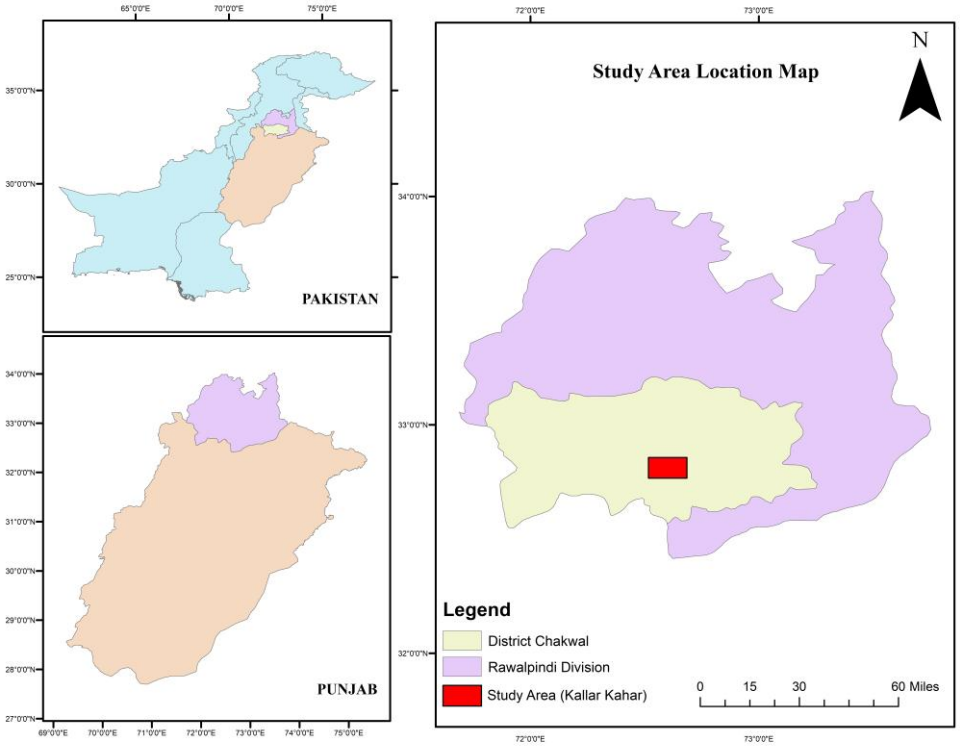

Figure 1.1. Location map of study area

Sardhai Formation of the Nilawahan Group in Salt Range, Punjab, is also of Early Permian age and mainly comprises of bluish-greenish-grey claystones with small amounts of sand and siltstone interbeds (Gee, 1964). Part of it is also covered with lavender clays, and chalcopyrite occurrences have been recorded in some parts indicating a possibility of copper mineralization. In this sequence, there is a record of the changing paleoenvironment through the Nilawahan Group (Tobra, Dandot, Warchha, and Sardhai Formations) the depositional environments ranging between glacial and shallow marine. The Sardhai Formation in particular has a near-shore marine environment, which is conducive to deposition of clay rich sediments that have the ability to adsorb and store trace and essential elements (Shah et al., 2012).

Although the Salt Range has conventionally been economically concentrated on rock salt, gypsum, limestone and coal, international trends in mineral demand are shifting towards elements that are considered critical minerals and include lithium, rare earth elements (REEs), cobalt, nickel and other technology metals, which are considered vital to renewable energy infrastructure and advanced manufacturing. More exploration models are appreciating the fact that fine grained sedimentary rocks, in particular, clays and shales, may contain a host of diverse and large concentrations of important minerals. Clay rich units can be geochemical traps and long-term store of critical minerals by adsorption, ionic exchange as well as diagenetic incorporation into mineral lattices (Hatch and Leventhal, 1992). Since the shale and mudstone intervals have been highly developed in the Paleozoic and Mesozoic stratigraphy of the Salt Range, it is scientifically valid and essential that such lithologies should be reconsidered in the critical mineral mind set in the future of progress.

The critical mineral systems located in clay and shale have become major exploration target in the world. Contrary to the traditional brine dominated systems, clay rich sedimentary sequences may also amass the important minerals by the weathering of source rocks, volcanic ash, alteration, and basin scale fluid circulation, as well as post depositional diagenesis. Otherwise, in structurally complex foreland basins like the Salt Range Potwar system, it is possible that tectonic deformation could increase the permeability and fluid rock contact and further affect the mobilization and concentration of important mineral within the basin. Thus, a geochemical based study and a systematic review of the geochemical data give a detailed structure to the possibility of using the fine-grained sedimentary units found in the Salt Range as a source of important minerals.

The 21st century has entered in an era in which the material basis of economic growth and environmental sustainability converge on an astonishingly limited number of elements collectively known as critical minerals. These elements, which include lithium, cobalt, nickel, rare earth elements, gallium, graphite and many more, are the material foundations of the clean energy technologies, advanced manufacturing process, digital technologies and medical technologies that define the technological

evolution of modern society (Graedel et al., 2015). The International Energy Agency (IEA, 2021) in its comprehensive report “The Role of Critical Minerals in Clean Energy Transitions”, projected that demand for these materials would expand by factors of four to six for most minerals and by as much as 42 times for lithium over the period 2020-2040, under a net-zero emissions scenario, confirming that solar photovoltaic panels, wind turbines, electric vehicle batteries, electrolysis and fuel cells are all far more mineral dependent than traditional fossil fuels.

The World Bank (2020), in its report Minerals for Climate Action, similarly forecasted that production of graphite, lithium and cobalt would need to grow by almost 500% by 2050 to supply clean energy demand under a 2°C warming emissions scenario, highlighting the scale of the resource mobilization challenge facing governments and industries worldwide. Graedel et al., (2015), in their assessment of the criticality of 62 metals and metalloids, confirmed that the minerals of greatest concern are those that are technologically impossible to functionally substitute in relevant time-frames, are highly geographically concentrated, and whose demand is driven by technologies whose deployment is itself essential to meeting global climate commitments attributes that together justify governmental and institutional responses at all scales from the national to international level.

In response to this, national governments have crafted increasingly institutionalized critical mineral policy infrastructures in the 2010s and 2020s. The U.S. developed its policy framework in response to Executive Order 13817 (Executive Office of the President, 2017), which instructed the U.S. Geological Survey to develop a list of critical minerals and determine federal actions to address supply chain vulnerabilities, resulting in a list of 35 minerals in 2018 that was expanded to 50 minerals under the Energy Act of 2020 (U.S. Congress, 2020; USGS, 2022), and again to 60 minerals in 2025 with rhodium, gallium, germanium, tungsten and niobium identified as the highest supply risk score minerals (USGS, 2025). In 2021 and 2022, the United States federal government allocated significant funding to support the resilience and independence of domestic critical mineral supply chains in the form of the Bipartisan Infrastructure Law (BIL) and the Inflation Reduction Act

(IRA). The scope of these legislative frameworks was to encompass targeted grant programs to support the establishment and expansion of mining and mineral processing operations within the country, structured financial incentives aimed at scaling up domestic battery manufacturing capacity, and the introduction of the Domestic Content Bonus Credit system. Which is a purpose built policy instrument designed to incentivize manufacturers of clean energy technologies to preferentially source their critical mineral inputs from within the United States rather than from foreign suppliers (DOE, 2023).

The European Union has undertaken a similarly approach in its Critical Raw Materials Action Plan (European Commission, 2020), which identified 30 critical raw materials and coordinated measures across supply diversity, the circular economy and domestic production, and culminating in the European Union's Critical Raw Materials Act of 2024 (European Parliament, 2024), which says that by 2030 the European Union extracts at least 10% of its annual consumption domestically, processes at least 40% domestically and recycles at least 25% from secondary sources. Australia, Canada, Japan, South Korea and the United Kingdom have also established national critical mineral strategies in this period, each of which is aligned with their respective resource endowments, industrial capabilities, and technology development priorities, and recognizes that critical mineral security has become highly essential for sustainable economic growth (IEA, 2023).

Multilateral organizations have also developed frameworks and collaborative research initiatives to complement national policy development and provide the necessary coordination to address global supply challenges. The International Energy Agency (IEA) has developed a Critical Minerals and Clean Energy program since its 2021 report, producing annual Critical Minerals Market Review analyses that monitor critical mineral supply and demand trends, investment and environmental performance (IEA, 2023). The United Nations Environment Program (UNEP) and International Resource Panel have included critical minerals in their broader work on sustainable resource governance. Schrijvers et al., (2020) provide an overview of

criticality assessment methods that have been used to guide harmonization of national approaches.

The World Bank (2020) has actively supported critical mineral supply chain development through its Climate Smart Mining Initiative, which has partnered with mineral resource rich developing countries to build sustainable, low-carbon, and inclusive mineral supply chains, that can support the clean energy transition while delivering economic development opportunities to the communities where critical minerals are produced. Binnemans et al., (2013) highlighted the recycling and urban mining of critical minerals from waste products as a key research and policy priority that requires coordinated international investment in collection systems, hydrometallurgical separation technologies and economic incentivization mechanisms, a message that has been incorporated into the circular economy provisions of both the EU Critical Raw Materials Act (European Parliament, 2024) and the US Department of Energy's (DOE) Critical Minerals and Materials research program (DOE, 2023). The cumulative evolution of national and multilateral responses reflects a transition in government and institutional thinking about the relationship between minerals, technology and sustainable prosperity from a reactive, market based to a proactive, and legally codified approach.

1.2 Objective

To conduct a thorough geochemical assessment and resource potential of critical minerals in the Sardhai Formation.

1.3 Significance of study

This study contributes both academically and practically. From an academic standpoint, it adds value by addressing existing gaps in the geochemical and mineralogical understanding of the Sardhai Formation, particularly with respect to its

critical minerals, which have so far received limited systematic attention in Salt Range. From an applied standpoint, the study supports economic development by identifying potential critical mineral resources within the formation that could inform future exploration efforts. Given the growing global demand for critical minerals in energy transition technologies, electronics, and advanced manufacturing, such findings may help stimulate activity within Pakistan's mining and energy sectors, while also providing a baseline geochemical dataset that can guide more targeted resource assessment in similar formations elsewhere in the region.

1.4 Expected outcome

Development of a detailed geochemical dataset and identification of critical minerals of the Sardhai Formation.

1.5 Literature review

Fine grained sedimentary rocks, in particular, shales and claystones are also becoming recognized as important sources of critical minerals. The trace elements (lithium, REEs, scandium, etc.) can be enriched in clay minerals (kaolinite, smectite and illite, etc.) by the process of adsorption on the surfaces of particles or by the elemental substitution in the crystal lattices. The shales in most of the sedimentary basins serve as geochemical catchers and over geologic time, the important minerals are concentrated. Black shales studies have demonstrated in various locations around the world that they may harbor maximum levels of vanadium, molybdenum, uranium and REEs that are commonly associated with anoxic environments and the growth and enrichment of organic matter. Though the extraction of said minerals in said shales is an expensive undertaking, geochemical enrichment of the said minerals over geologic time indicates the ability of fine-grained sediments to store critical minerals (Hatch and Leventhal, 1992). Mineral systems whereby shales are the host systems are well established in the sedimentary basins around the world. Appalachian Basin’s black shales of the Devonian to Mississippian age in Northern hemisphere of America

have unusual levels of various trace metals, such as vanadium and nickel, which are thought to have been deposited by euxinic environments and organic complexation (Leventhal, 1991).

It is also known that rare earth elements (REEs) tend to accumulate in clay rich regolith and sedimentary systems. The deposits of ionic adsorption REE in south China are found in earnestly weathered granitic landscapes where REEs are insensitively attached to kaolinite clays and can be extracted by straightforward leaching. These are mostly regolith hosted as opposed to sedimentary basin deposits, but the most important geochemical process that is the adsorption of the REEs onto the surfaces of the clay minerals certainly shows the affinity of the fine grained aluminosilicates to critical minerals. REEs are also reported to be concentrated in phosphatic shales and organic rich mudstones in the context of the sedimentary systems where redox conditions and clay mineralogy tend to affect the elemental partitioning (Chi & Tian, 2011).

Structural deformation is also one of the key players influencing the geochemical evolution of clay rich strata. Fractured networks, thrust faults, and fold hinges increase the permeability of otherwise tight lithologies, creating preferential pathways that bring basinal fluids into prolonged contact with clay rich rocks. The degree to which a deforming sequence develops this kind of permeability architecture is itself governed by its mechanical stratigraphy, that is, by how competent and incompetent layers, such as evaporites, shales, and clays, are stacked and how each responds differently to shortening. Studies in other fold-and-thrust belts illustrate this relationship clearly; in the central Zagros Mountains, variations in fold geometry along the belt are closely tied to changes in the mechanical behavior of the lithostratigraphic horizons, particularly the presence of intermediate decollement levels within the sedimentary pile (Sherkati et al., 2006). Where such decollements and their associated fracture networks develop, they act as long-lived conduits capable of channeling metal-bearing fluids toward favorable trap sites, a principle directly relevant to the Salt Range, where the Salt Range Formation evaporites already provide a basal decollement, and where diapir flanking faults and oblique structures at localities such as Kallar Kahar represent the most likely sites of enhanced fluid flux

and consequent geochemical modification of overlying clay rich units such as the Sardhai Formation.

Among the most notable occurrences of clay-hosted critical mineral mineralization is the lithium deposit of the McDermitt Caldera on the Nevada–Oregon border, where altered volcanic ash layers within lacustrine sediments host what may be the largest lithium clay resource yet identified. The caldera formed following a major eruption roughly 16.4 million years ago, after which a long-lived lake accumulated a thick pile of ash-derived sediment that was altered into lithium-bearing smectite clay. Critically, post-caldera hydrothermal fluids subsequently converted much of this smectite into illite in the southern part of the caldera, producing lithium grades of up to roughly 1 weight percent, more than double the lithium content of the unaltered smectite-rich claystones found elsewhere in the basin (Benson et al., 2023). In other words, the original volcanic glass supplied the lithium budget via initial alteration to clay, while a later hydrothermal overprint of that clay mineralogy is what concentrated it into ore-grade material. This two-stage process; initial uptake of a metal by a clay precursor, followed by a secondary mineralogical transformation that upgrades its grade, offers a useful conceptual analogue for considering how trace and critical metals incorporated into the Sardhai Formation's clays during deposition might have been subsequently modified or redistributed by later diagenetic or structurally driven fluid events.

Recent developments in critical mineral exploration increasingly favor a mineral systems approach, in which the source, transport pathway, trap, and preservation of a given metal are treated not as isolated deposit scale features but as interlinked components of a single, scale-spanning earth system (McCuaig and Hronsky, 2014). Under this framework, an economically significant mineral system requires four critical elements to combine in space and time: a favorable lithosphere-scale architecture, transient favorable geodynamics, a fertile metal source, and adequate preservation of the primary depositional zone. Applied to a sediment-hosted setting such as the Salt Range, this framework usefully reframes the components already discussed above into a single coherent system; the source is the metal budget held within redbed and evaporite-bearing strata; the pathway is the network of

decollement related thrusts and fractures; the trap is the redox boundary at lithological contacts such as that between the Warchha Sandstone and the Sardhai Formation; and preservation depends on how much subsequent uplift, weathering, and erosion has left that trap intact.

Coal formations may also serve as an important source of critical minerals, since coal seams and their associated clay partings are well documented globally as effective hosts for elements such as the rare earths, lithium, gallium, and germanium, at times at concentrations exceeding those of many conventional ore deposits. This reflects the way transported detrital sediment, volcanic ash, and circulating groundwater can each act as enrichment mechanisms in a coal-bearing basin, with the resulting metals ultimately partitioned between the organic matter and any associated mineral matter, particularly clay minerals. Khan et al., (2023) demonstrated this in a regional Pakistani context: an exploratory geochemical survey of 13 coal mines across Khyber Pakhtunkhwa found maximum concentrations of several key minerals exceeding the global average for coals, with clay minerals identified as one of the principal hosts. This finding is directly relevant to the present study, as it reinforces the broader theme that clay dominated lithologies, whether coal associated or, as with the Sardhai Formation, an independent clay-rich unit, can act as significant, and frequently under evaluated, repositories of critical and trace metals.

In a related vein, Zeb et al., (2020) carried out a synoptic geochemical analysis of the Chichali Formation in the Kohat sub basin of Khyber Pakhtunkhwa, examining the major and trace element composition of its sedimentary rocks to gain insight into provenance, paleoclimate, and depositional environment. Their analysis drew on the kind of geochemical proxies routinely used in sedimentary provenance work, weathering indices to assess the intensity of chemical alteration in the source area, discriminant element ratios to infer the nature of source lithologies, and redox-sensitive trace element behavior to reconstruct bottom-water oxygenation during deposition. While critical mineral evaluation was not a direct focus of their work, the trace element enrichment trends they identified establish an essential geochemical background framework for the formation. Such foundational sedimentary geochemical investigations, even where not explicitly framed around critical minerals,

play a crucial role in evaluating the sediment-hosted critical mineral potential of analogous geological settings, since they supply the provenance, weathering, and redox context against which any later, more targeted critical mineral signal must be interpreted, a parallel directly applicable to the present geochemical characterization of the Sardhai Formation.

Another study by Shah et al., (2020) employed an amalgamated technique of magnetic prospecting and geochemical analysis to investigate the mineral in the Mali-Dera deposits of the Kohistan Island Arc in Pakistan. The test was carried out using magnetic surveys of 77 stations, and geochemical analysis of rocks samples. In the process of comparing the geophysical and geochemical data, the authors discovered the high Fe, Mn, Cu and Ni concentration zones that were associated with high magnetic susceptibility. It was proposed that magnetite, chromite and Cu-pyrite mineralization would occur. This research demonstrated that geophysical and geochemical investigations can be used to focus mineral exploration objectives particularly in the mafic and ultramafic environments.

Furthermore, Zaheen et al., (2020) conducted mineralogy and geochemistry of the peridotites and chromites of the Jijal Complex ophiolite of the Main Mantle Thrust (Indus Suture Zone) in the northern part of Pakistan. They have employed petrological study, mineral chemistry, major and minor element geochemistry and microprobe studies of ophiolitic rocks in their approach. The results revealed high degrees of partial melting and significant change in the chemistry of chromite, and tectono-magmatic controls of mineralization. The other study revelation was the potentiality of base and strategic metal enrichment which accompanies the existence of ophiolitic complexes and the metallogenic significance of such tectonic environments in the north of Pakistan.

Abubakar et al., (2024) investigated the economic and health risks of trace elements in new phosphate deposits located at Paswal Mian, Banseri and Shahkot in Abbottabad. Their method involved systematic sampling of the phosphate rocks, major, and trace element geochemistry analysis, spatial mapping, and human health

risk assessment model. The level of P2O5 was observed to range between approximately 12-25, which showed that the sample was appropriate to make fertilizers. Trace elements such as Pb, Cr and Zn were noted to have a considerable spatial distribution across sites. It is important to note that the health risk assessment suggested overall low levels of ecological and human risks. The article is particularly significant because it exemplifies a thorough model of economic analysis, trace element geochemistry, and environmental risk analysis, which could be highly helpful in contemporary critical mineral studies.

CHAPTER 2
GEOLOGY AND TECTONICS

2.1 Regional Geology

The Salt Range occupies the southernmost structural front of an orogenic system whose history traces back roughly 130 million years, to when the Indian Plate broke away from Gondwanaland and began drifting north, setting in motion the closure of the Neo-Tethys Ocean that separated it from Eurasia (Johnson et al., 1986). Drift rates accelerated sharply after about 80 Ma, from a sluggish 3–5 cm/yr to nearly 16 cm/yr (Johnson et al., 1986; Powell, 1979; Patriat and Achache, 1984), carrying India toward intra-oceanic arc systems, mainly the Kohistan Ladakh Arc formed as the Neo-Tethys closed by subduction (Searle, 1991; Treloar and Izatt, 1993).

Collision of this arc with the Karakoram Plate along the Main Karakoram Thrust in the Late Cretaceous (Coward, 1986), followed by suturing of the Indian Plate itself to the arc along the Main Mantle Thrust during the Eocene (Tahirkheli, 1979), drove a progressive southward stepping of deformation through the Main Boundary Thrust and across the Northern and Southern Deformed Fold and Thrust Belts (Yeats and Hussain, 1987; Ahmad, 2003).

This southward front of deformation finally ceases out at the Salt Range Thrust and Trans Indus Ranges, the structures that have carried the ancient Salt Range succession, which is the focus of this study, southward over the much younger sediments of the Jhelum Plain (Gee, 1989; Lillie et al., 1987).

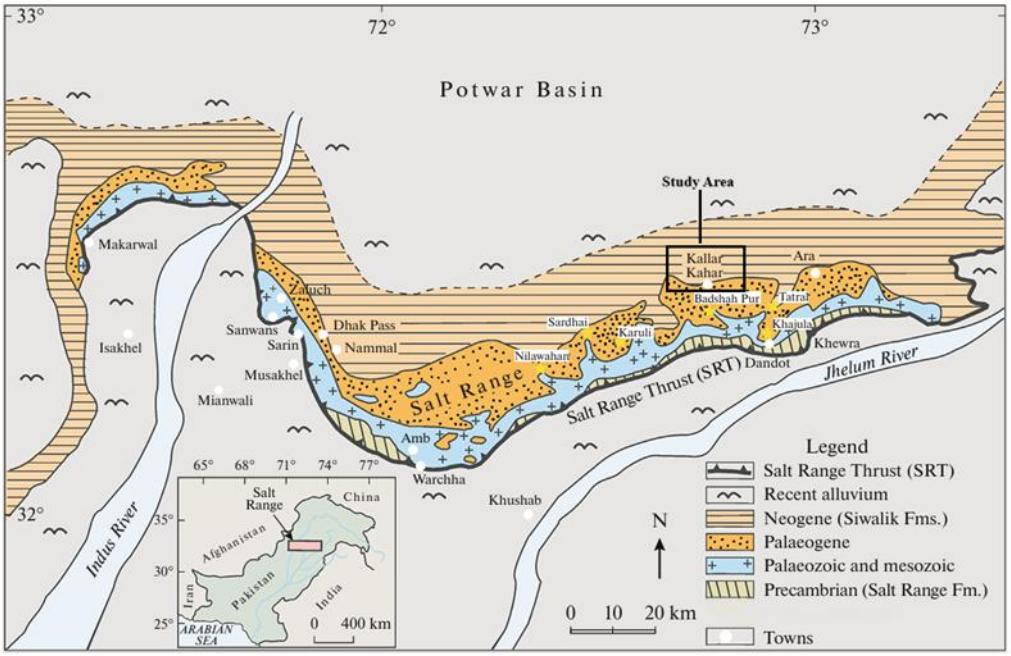

Figure 2.1. Generalized geological map of the Salt Range, northern Pakistan, showing the study area along the southern margin of the Potwar Basin. The map depicts Precambrian, Palaeozoic to Mesozoic, Palaeocene, and Neogene units alongside the Salt Range Thrust (SRT), with key towns and rivers (Indus and Jhelum rivers) for reference. The study area lies in the eastern Salt Range near Ara, Tatral, and Khewra, where exposed sections and thrust-related structures aid interpretation of the region's geological evolution (modified after Ghazi et al., 2020)

2.1.1 Structural framework of the study area

This regional history is conventionally divided into seven north to south tectonostratigraphic zones; the Main Karakoram Thrust, the Kohistan Island Arc, the Main Mantle Thrust, the Northern Deformed Fold and Thrust Belt, the Main Boundary Thrust, the Southern Deformed Fold and Thrust Belt, and, forming the southernmost and youngest element of the system, the Salt Range Thrust and Trans Indus Ranges (Gansser, 1964; Yeats and Hussain, 1987). The present study area lies entirely within this last zone, and its structural character is best understood on its own terms rather than as a simple extension of the basement involved thrusting seen further north.

The Salt Range Thrust also termed as the Himalayan Frontal Thrust, bounds the range to the south and has translated the Paleozoic to Cenozoic Salt Range succession over the younger Neogene Quaternary fill of the Jhelum Plain (Gee, 1945, 1989; Yeats et al., 1984). Critically, seismic, gravity, and paleomagnetic data converge on a single mechanism for this translation; a decollement seated within the thick, mechanically weak Precambrian evaporites of the Salt Range Formation, which underlies the entire cover sequence and has accommodated at least 20 km of shortening across the Salt Range and Trans Indus Ranges, locally rising to 29 km in the central Salt Range (Farah et al., 1977; Johnson et al., 1986; Lillie et al., 1987; Baker et al., 1988; Blisniuk, 1996). Because the overlying cover rides essentially passively on this salt detachment, the range has folded into a broad "salt pillow" type anticlinorium (Trusheim, 1960), with diapiric breakthrough developed locally at Kallar Kahar, Vasnal, Mari Indus, and Kalabagh, where high angle faults cut obliquely across the dominant east west grain of the range (Gee, 1989). Further east the range bifurcates into the Dil Jabba and Chambal Jogi Tilla ridges, while the Kalabagh Fault separates it from the Trans Indus Ranges to the west (Gee, 1989; McDougall and Khan, 1990). This thin skinned, salt cored structural style is the single most important structural fact about the study area.

2.2 Influence of tectonics on mineral deposition in area

The structural architecture described above exerts a direct control on metal distribution within the Salt Range succession, through two linked mechanisms; the lithological pairing inherited from the basin's depositional evolution, and the fluid pathways created by salt tectonics. The first mechanism is the redbed to graybed transition preserved at the Warchha–Sardhai contact. The Warchha Sandstone is an oxidized, fluvially deposited arkosic redbed sequence, overlain abruptly by the reduced, organic bearing clays and carbonaceous shale of the Sardhai Formation. This pairing of an oxidized clastic source with an overlying reduced, carbonaceous trap is the diagnostic setting in which sediment hosted stratiform copper (SSC) systems form globally; such deposits form through the movement of oxidized, copper bearing fluids across a reduction front, which precipitates copper sulfides where the fluid meets a

reduced host rock (Hitzman et al., 2010). A copper occurrence has, in fact, been documented pointing precisely at this contact, in both the Warchha Sandstone and the Sardhai Formation of the Salt Range (Qureshi, 1980).

The second mechanism is structural. Because the entire cover sequence decouples from its basement along the Salt Range Formation evaporites, the range is threaded by decollement related thrusts, oblique faults, and diapir flanking fractures (Gee, 1989; Lillie et al., 1987).

2.3 Tectonic evolution of the study area

2.3.1 Passive margin development

Before the Himalayan collisional history began, the northern margin of the Indian Plate spent a long interval as a tectonically quiescent, sediment accumulating shelf. Within the Salt Range, this phase is recorded by the transition from the rift related Nilawahan Group into the conformably overlying Zaluch Group, a well exposed succession of shallow marine to inter tidal carbonate facies deposited on a large carbonate platform developed on Gondwana continental crust close to the Indian Shield (Mertmann, 2003). This shift from the cool, clastic dominated Gondwanan facies of the Nilawahan Group to the warm, carbonate dominated Tethyan facies above, marks the point at which the northern Indian margin settled into a long lived passive margin configuration that would persist, largely undisturbed, until renewed Himalayan deformation in the Cenozoic.

2.3.2 Opening of Neo-Tethys

The ocean that this passive margin eventually faced opened during the Permian, as part of the broader rifting of Cimmerian terranes away from Gondwana's northern margin, which created the Neo-Tethys basin to their south. Within the Salt Range itself, this regional extensional episode is recorded directly in the rock record;

the Syn-Permian Rift phase of the Nilawahan Group corresponds to the outpouring of the Panjal volcanics together with deposition of the regressive fluvial facies of the Warchha Sandstone within the rift basin, during the Artinskian cool to warm climatic interval (Ahmad et al., 2018).

2.3.3 Plate subduction and arc development

As the NeoTethys widened to the south, its older oceanic lithosphere was consumed beneath the advancing margin to the north, generating a chain of intra oceanic arcs, most prominently the Kohistan Ladakh, Nuristan, and Kandahar arcs, through the Late Cretaceous (Searle, 1991; Treloar and Izatt, 1993), with arc magmatism remaining active until about 40 Ma (Petterson and Windley, 1985). Large scale Deccan Trap volcanism between 65 and 60 Ma marked the continued passage of the Indian Plate over a mantle hotspot during this transit (Duncan and Pyle, 1988). The Kohistan Ladakh Arc was itself eventually thrust beneath the Eurasian Plate, producing an Andean style margin expressed as the Main Karakoram Thrust, with collision constrained to 102–75 Ma (Coward, 1986; Powell, 1979; Patriat and Achache, 1984); the Indian Plate then collided with the arc's leading edge in turn, an event expressed as the Main Mantle Thrust and marking the end of marine sedimentation within the suture zone (Tahirkheli, 1979; Rowley et al., 1996).

2.3.4 Neogene to recent deformations

Following continent to continent suturing, compressional deformation propagated steadily southward, through the Main Boundary Thrust (Lisa and Khwaja, 2005; Kazmi and Jan, 1997) and across the Northern and Southern Deformed Fold-and-Thrust Belts (Yeats and Hussain, 1987), until it reached the foreland itself. Within the study area this final, youngest stage of deformation is expressed as thin skinned, salt detached thrusting along the Salt Range Thrust and Trans Indus Ranges, accommodating 20–29 km of shortening on a decollement within the Salt Range Formation (Lillie et al., 1987; Baker et al., 1988; Blisniuk, 1996). The Trans Indus

Ranges, where the Surghar and Khisor Ranges are actively thrust over the Indo Gangetic Foredeep, represent the current point of this deformation (Hemphill and Kidwai, 1973) and have been identified elsewhere as the youngest compressional structure of the Himalayan foreland system (Grelaud et al., 2003) confirming that the Salt Range region remains tectonically live today.

2.3.5 Sedimentary features

The progressive southward growth of the orogen is recorded sedimentologically in the molasse sequences shed from the rising mountain front. The Murree, Kamlial, and Siwalik Group sediments form a thick, coarsening and youngening southward clastic wedge of fluvial sandstone, conglomerate, and red clay that accumulated in front of the advancing Main Boundary Thrust from the Miocene onward, directly recording the unroofing history of the hinterland. This syn orogenic sedimentation continues, in attenuated form, as the alluvial and fanglomerate cover that today masks much of the Salt Range Thrust front itself (Gee, 1989), the youngest sedimentological expression of the same compressional system that produced the Salt Range anticlinorium.

2.4 Stratigraphy of The Salt Range

The Salt Range preserves a near continuous record from the Upper Proterozoic to Recent, conventionally grouped into the PreCambrian Strata, Jhelum Group, Nilawahan Group, Makarwal and Chharat Group, Rawalpindi Group, and Siwalik Group, in ascending order of age.

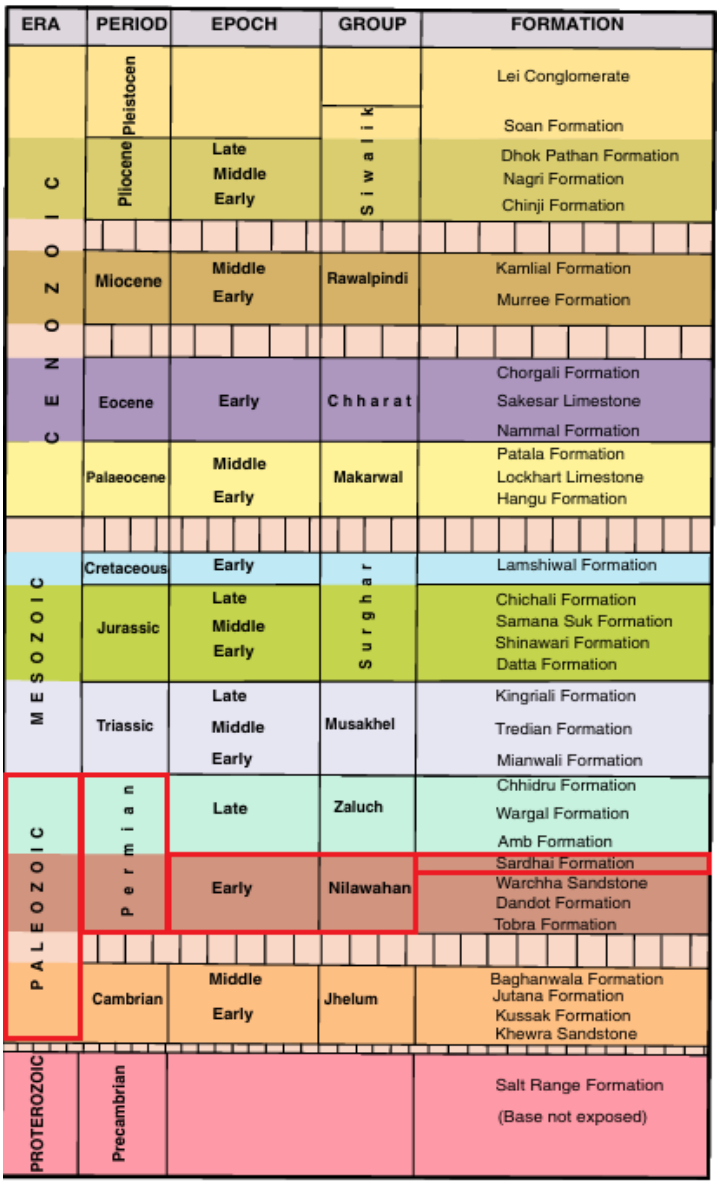

Figure 2.2. Generalized Stratigraphic Column of Salt Range showing the formations, Sardhai Formation of present study highlighted in red (modified after Ghazi et al., 2015)

2.4.1 Precambrian age

At the base of the entire succession lies the Salt Range Formation (named successively the "Saline Series" by Wynne, 1878, the "Punjab Saline Series" by Gee, 1945, and finally the Salt Range Formation by Asrarullah, 1967), comprising a lower division of red gypseous marl, salt, and gypsum and an upper division of dolomite,

greenish clay, and low-grade oil shale, divided by Asrarullah et al., (1967) into the Sahwal Marl, Bhandar Kas Gypsum, and Billianwala Salt members. As established above, this formation is far more than a stratigraphic curiosity; it is the mechanically weak detachment horizon on which the entire structural architecture of the Salt Range is built.

2.4.2 Cambrian to Cenozoic

Above the Salt Range Formation, the Khewra Sandstone and Kussak Formation (Jhelum Group, Early to Middle Cambrian) record fluvial to shallow marine deposition with notable ichnofossil and conglomeratic intervals (Noetling, 1894; Fatmi, 1973). After a long depositional hiatus, the Permian Nilawahan Group resumes the record. The succeeding Paleocene Patala Formation, Eocene Nammal Formation, Sakesar Limestone, and Chorgali Formation form a fossiliferous shale-marl-limestone sequence reflecting renewed shallow Tethyan marine conditions (Davies and Pinfold, 1937), before the Miocene-Pliocene Murree, Kamlial, and Siwalik Group sediments cap the sequence as the syn-orogenic molasse wedge.

2.4.3 The Sardhai Formation

2.4.3.1 Stratigraphic age and position

The Sardhai Formation is the uppermost of the four formations comprising the Nilawahan Group, overlying the Tobra, Dandot, and Warchha formations in turn, and was originally termed the "Lavender clays" by Wynne (1878) and regarded as the upper part of the "Warchha group" by Noetling (1901), before being formally named by Gee (Pascoe, 1959) and ratified by the Stratigraphic Committee of Pakistan. Based on faunal and floral age constraints and stratigraphic superposition, the formation is assigned to the Middle Permian (Kungurian) (Ahmad et al., 2018). At its type locality in Sardhai Gorge it is 42 m thick, thickening to 65 m in the western Salt Range and thinning to 50 m in the Khisor Range; its lower contact with the Warchha Formation and its upper contact with the overlying Amb Formation are both considered

conformable (Shah, 1977), the Amb Formation being the basal unit of the overlying Zaluch Group.

2.4.3.2 Depositional environment

Sardhai Formation deposition was triggered by an abrupt, basin wide event; a widespread marine transgression that terminated the fluvial regime of the underlying Warchha Sandstone and produced a sharp upward transition into the shallow marine Sardhai Formation. This transgression is interpreted as the eustatic sea level rise of the Post Permian Rift phase (Kungurian–Wordian), which flooded a broad, slowly subsiding "sag-type" basin under a warm hot climatic regime (Ahmad et al., 2018), in marked contrast to the very cold glacial conditions under which the lowermost Tobra Formation had accumulated. Across the Nilawahan Group as a whole, the regional paleoclimate evolved progressively from very cold-cold during Tobra deposition, through cold–cool (Dandot) and cool–warm (Warchha), to warm–hot during Sardhai deposition (Singh, 1987; Veevers and Tewari, 1995). The dominance of fine grained, largely unfossiliferous clay, interrupted only by thin sand and silt beds and occasional carbonaceous shale, points to a low energy, restricted shallow marine to lagoonal setting with periodically reducing bottom water conditions; the rare plant remains and fish scales reported from the Khisor Range suggest at least intermittent proximity to a marginal, deltaic influenced shoreline. This contrast between the cool, continental "Gondwanan" character of the Nilawahan Group and the warm, richly fossiliferous "Tethyan" character of the overlying Zaluch Group records a gradual change from marginally glacial to marginally warm water deposition across the Early to Middle Permian boundary (Wardlaw and Pogue, 1995), with the Sardhai Formation occupying the pivotal, transitional position in that change.

2.4.3.3 Lithology

The formation is dominated by bluish and greenish, lavender toned clay, with subordinate beds of fine sand and siltstone and occasional carbonaceous shale. The clay carries a copper signature, and a copper showing has been specifically documented at the Warchha–Sardhai contact (Qureshi, 1980), consistent with the formation's position immediately above an oxidized redbed source rock at a sharp lithological and redox boundary.

2.4.3.4 Basin evolution

Set against the wider stratigraphic record of southern Gondwanaland (the Indian Peninsula, Arabia, South Africa, and Australia), the Nilawahan Group is interpreted as recording three successive tectono climatic phases (Ahmad et al., 2018). The Pre-Permian Rift phase deposited the glaciogenic Tobra Formation and tidally influenced Dandot Formation within a young intra cratonic basins under a very cold to cold climate; the SynPermian Rift phase saw outpouring of the Panjal volcanics together with regressive fluvial deposition of the Warchha Sandstone within the actively rifting basin under a cool to warm climate; and the Post Permian Rift phase, during the Kungurian–Wordian, was marked by a eustatic sea level rise that deposited the Sardhai Formation in a sag-type shallow marine basin under a warm to hot climate (Ahmad et al., 2018). The Sardhai Formation therefore represents the waning, thermal subsidence stage of this rift cycle, the point at which active extension and Panjal volcanism had ceased and the basin was simply subsiding and filling under rising sea level. In doing so, it forms the direct stratigraphic and tectonic bridge between the syn rift, Gondwana affinity clastics below and the fully passive margin, Tethyan carbonate platform of the Zaluch Group above, closing out the Permian rift history of the Salt Range before nearly 300 million years of relative quiescence elapsed until the onset of Himalayan related deformation.

CHAPTER 3
METHODOLOGY

3.1 Methodology workflow

This study follows a six-stage workflow for geochemically characterizing the Sardhai Formation. Fieldwork and sampling yielded 22 specimens (US1–US22) from two localities within area of Kallar Kahar. After sample preparation (crushing, pulverizing, homogenization), specimens underwent ICP-MS analysis to quantify critical minerals including trace elements, uranium, phosphorus, REEs, and other base metals as shown in chapter (4) four. Results compiled during data acquisition into a 22-sample dataset, then evaluated in data interpretation to identify formation wide geochemical baselines. The final stage being results and conclusions to assess the critical mineral potential. The following methodology workflow has been adopted for this study;

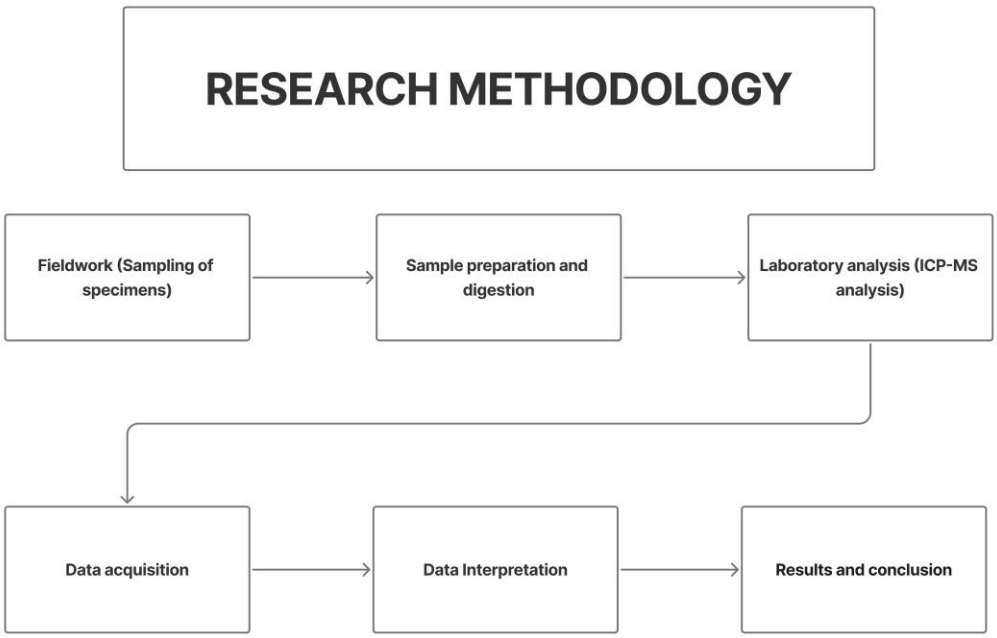

Figure 3.1. Methodology workflow adapted for current study

3.1.1 Fieldwork and sampling

The Sardhai Formation in Punjab, Pakistan was sampled perpendicular to the dip. The choice of sampling this specific formation was due to its clay rich nature and the possibility of containing critical minerals. The fieldwork for sampling the formation was carried out in such a manner that the representative samples of the formation could be extracted from the exposed outcrop. The selection of field sites was done after a thorough assessment of site suitability, location, and minimum weathered conditions.

Twenty-two (22) clay specimens were sampled from the outcrops within the vicinity of Kallar Kahar region, one site being the Peeran-e-Morjang roadside section and the other being Khushab roadside section. Four (4) representative samples from the only approachable outcrop were taken at Peeran-e-Morjhang roadside section (PMJRSS) being US1-US4, and eighteen (18) representative samples being US5-US22, were taken from Khushab roadside section (KRSS) as the area was more approachable and the variety in outcrop exposure was significant. Out of the eighteen samples taken from the KRSS, samples (US7-8, US10-11, US13, and US18-19) were from patches on the outcrop that showed visible signs of oxidation, whereas the rest were taken from non-oxidation patches. Fresh surface was targeted during the sampling process to avoid effects of erosion and weathering. Extraction was done after the removal of weathered surfaces from outcrop exposure using a geological hammer and chisel. All samples were weighed and ranged from 500gm to 900gm.

The samples were put and stored in clean high density polyethylene sample packs after they had been labeled properly to avoid mistakes in numbering. The shape and structure of the sample containers being nonmetallic helped in avoiding the cross contamination of samples during the trace metal analysis. All the samples were marked with GPS coordinates, lithological description and mineralogical observation noted along with field photographs taken for archiving of sites.

Figure 3.2. Field photograph of a weathered exposure of the Sardhai Formation at KRSS, Salt Range, showing its characteristic fine-grained, thinly bedded clay dominated lithology. A geological hammer is placed for scale along a fresh surface. Representative specimens from fresh surface were collected from this section for subsequent ICP-MS geochemical analysis, camera facing (NE)

Figure 3.3. Field photograph of a weathered exposure of the Sardhai Formation at KRSS, Salt Range, showing its characteristic fine-grained, thinly bedded clay dominated lithology along with a patch of oxidation below the hammer. A geological hammer is placed for scale. Representative specimens from fresh surface were collected from this section for subsequent ICP-MS geochemical analysis, camera facing (NE)

Figure 3.4. Field photograph of a weathered exposure of the Sardhai Formation at KRSS, Salt Range, showing its characteristic fine-grained, thinly bedded clay dominated lithology. A geological hammer is placed for scale and being used for collection of clay specimens. Representative specimens from fresh surface were collected from this section and stored in bags as shown for subsequent ICP-MS geochemical analysis, camera facing (NE)

Figure 3.5. Field photograph of a weathered exposure of the Sardhai Formation at PMJRSS, Salt Range, showing its characteristic fine-grained, clay dominated lithology. A marker is placed for scale. Representative specimens from fresh surface were collected from this section for subsequent ICP-MS geochemical analysis, camera facing (NE)

Figure 3.6. Sample specimens stored in bags taken from PMJRSS and KRSS

Table 3.1. Coordinates of samples for Peeran-e-Morjhang roadside section

Sr. no	Name	Latitude	Longitude
1	US1	32.667932	72.71447
2	US2	32.668012	72.71452
3	US3	32.668041	72.714567
4	US4	32.667973	72.714579

Table 3.2. Coordinates of samples for Khushab Roadside section

Sr. No.	Name	Latitude	Longitude
5	US5	32.767245	72.695968
6	US6	32.767245	72.695980
7	US7	32.767249	72.695993
8	US8	32.767252	72.696007
9	US9	32.767266	72.696019
10	US10	32.767280	72.696027
11	US11	32.767281	72.696048
12	US12	32.767285	72.696079
13	US13	32.767294	72.696096
14	US14	32.767310	72.696115
15	US15	32.767324	72.696133
16	US16	32.767344	72.696154
17	US17	32.767362	72.696167
18	US18	32.767373	72.696194

19	US19	32.767640	72.696352
20	US20	32.767656	72.696431
21	US21	32.767670	72.696469
22	US22	32.767694	72.696497

Figure 3.7. Peeran-e-Morjhang roadside sampling location map

Figure 3.8. Khushab roadside sampling location map

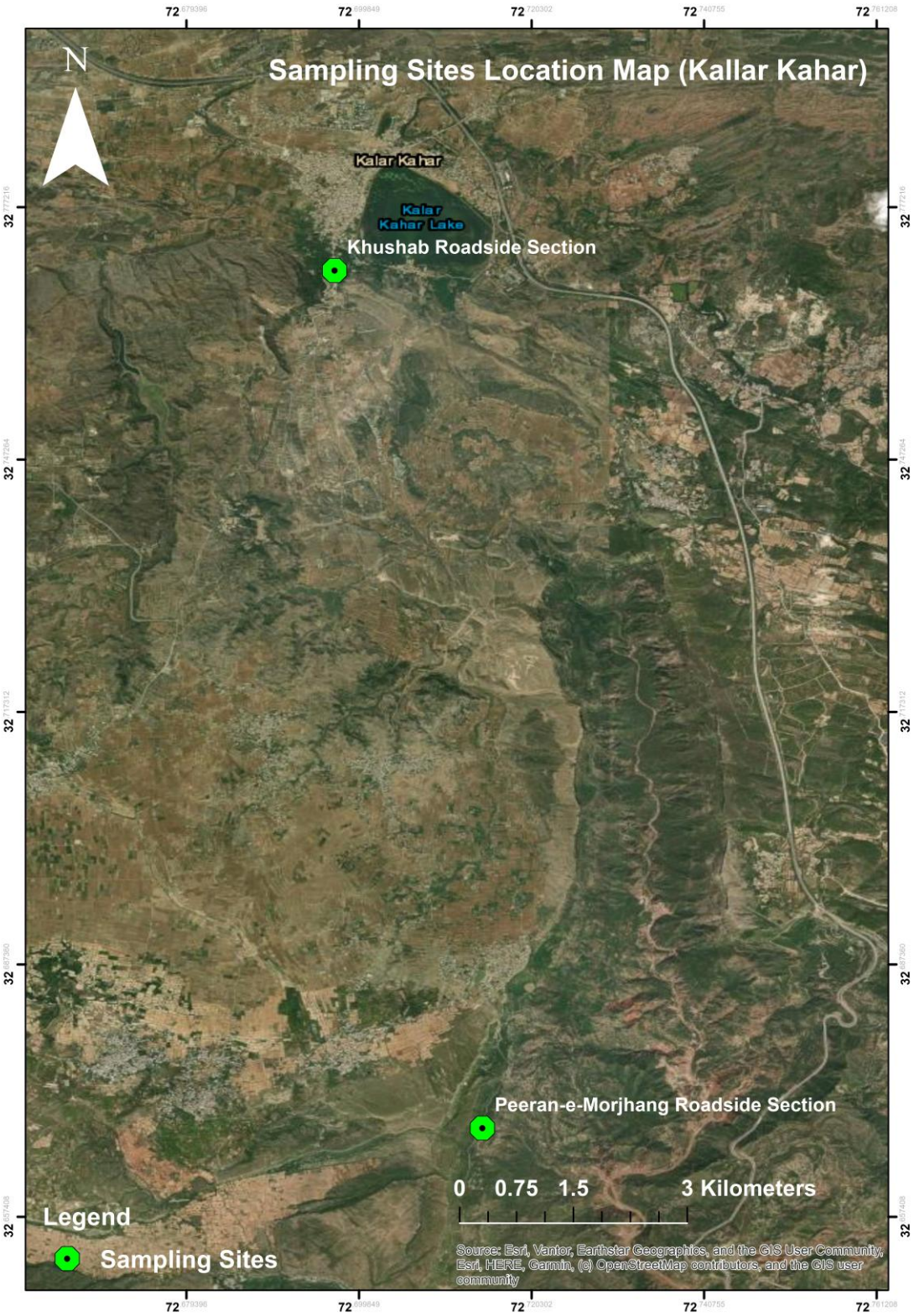

Figure 3.9. Sampling sites location map (Kallar Kahar)

3.1.2 Sample preparation

Solid samples were dried in room temperature for the elimination of remnant moisture. For the preservation of the critical minerals which themselves are quite volatile, thermal drying was avoided. The samples were sieved through meshes of different sizes 30 and 100 to retain fines from the samples taken. After that the sample fines were weighed on a weighing scale for the acid digestion process in line with the procedure presented by Zhang and Hu (2019).

Figure 3.10. Weighing balance used for fines

Geological materials have a great importance in the determination of critical minerals including the trace native elements present therein using the Inductively Coupled Plasma Mass Spectrometry technique or (ICPMS). The choice of aqua regia as the digestion reagent was based on its strong oxidizing and dissolving properties, which are formed by the formation of free chlorine (Cl2) and nitrosyl chloride (NOCl) as oxidizing and dissolving reagents, respectively, which in turn allow the breakdown

of carbonates, sulphides, and organic matter phases, as well as dissolve noble and base metals (Robinson, 2025). Approximately 0.5g of material was used for the digestion process on hot plate, available laboratory flasks were used as vessels for the acid and clay fines mixture and were then heated on a hot plate, in line with procedures mentioned by Gaudino et al., (2017).

Thus, all procedural SOPs like lab coats, gloves, googles, and KN95 masks were used during this procedure while under the supervision of lab scientist. Clean flasks, beakers, and spatulas were used which were cleaned with distilled water, they were also labeled properly with permanent markers so the ink might not dissipate during the process of heating on a hot plate. The bottles used for the storage of final solution for ICPMS were also cleaned with distilled water. The beakers were then taken off the hot plate and 30ml of distilled water was added for dilution of concentrated samples and having them let cool off, procedure that is in line with Gaudino et al., (2017).

Figure 3.11. Heating sample solution for digestion of specimen fines in aqua regia

The chemical reactions which take place are the oxidation of metals through acids and creation of chloro-complexes through the action of chloride ions with the metals present therein.

$$3HCl+HNO3 \rightarrow NOCl+Cl2+2H2O$$

The samples were then filtered for the first time through normal filters into bottles, after which the bottles were left for some time to wait for the final syringe filtration which removed the left-over TDS particles left in the solutions while following SOP's for avoiding sample contamination.

Figure 3.12. Sample filtration process

Figure 3.13. Syringe filtration processes

Figure 3.14. Final digested samples in bottles

3.1.3 Inductively Coupled Plasma Mass-Spectrometry (ICPMS)

3.1.3.1 Components of ICP-MS

Inductively coupled plasma mass spectrometry (ICP-MS) analysis was conducted at the science laboratory of Allama Iqbal Open University, Islamabad. It is the analytical method of choice for multi-element, trace and ultra-trace element geochemical analysis, where it can simultaneously measure more than 70 elements of the periodic table at concentrations from parts-per-million (ppm) to parts-per-trillion (ppt) levels (Thomas, 2013). The technique was pioneered by (Houk et al., 1980), who were able to couple an argon inductively coupled plasma (ICP) ionization source to a quadrupole mass spectrometer (QMS), with the first commercially available ICP-MS introduced in 1983 by Sciex, after which the technique quickly became the method of choice for global geological trace element analysis (Schönbächler, 2016). The sample preparation begins at the sample introduction system, in which a liquid digest is introduced via a pneumatic nebulizer, which produces an aerosol that is then size-selected by a spray chamber (typically a Scott or cyclonic double-pass type) cooled to 2°C such that only droplets with diameters of less than about 8 μm enter the plasma torch (Thomas, 2013). The plasma torch itself is composed of three concentric quartz tubes through which argon flows at 12-18 L/min, and a radio-frequency (RF) induction coil at 27 MHz and up to 1600W in energy, which maintains an argon plasma between 6,000 K and 10,000K that is capable of vaporizing, atomizing, desolvating and ionizing all elements of the periodic table to singly charged positive ions (M^+) with nearly 100% efficiency for elements that have first ionization energies below approximately 8eV (Shimadzu, 2024; Houk et al., 1980).

3.1.3.2 Working principle of ICP-MS

The Ions which exit the atmospheric pressure plasma are transmitted into the high vacuum mass spectrometer via a two stage, differentially pumped interface comprising a nickel, sampling cone and a skimmer cone whose aperture is around 0.5 mm, through which gas pressure is maintained at 1-2 mbar by a rotary pump,

followed by an electrostatic ion lens system that focuses and accelerates the ion beam into the mass analyzer (Linge, 2024). The quadrupole mass analyzer, four parallel rods, to which DC and RF voltage is applied, is a variable mass filter that selectively transmits ions of selected mass-to-charge (m/z) ratios to the detector and repels all other ions (Thomas, 2013). The quadrupole-transmitted ions are detected by an electron multiplier in both pulse-counting and analogue modes, that allows simultaneous measurement of major and ultra-trace elements from single, diluted solution (Ammann, 2007). A significant analytical challenge for the technique is spectroscopic interference, particularly from polyatomic ions. such as 40Ar16O+ that interfere with 56Fe+, which are formed by combinations of argon carrier gas, solvent, and matrix species, which are reduced in contemporary instruments via collision-reaction cell technology, in which a multipole reaction cell filled with high-pressure helium or reactive gases either reduces the kinetic energy of polyatomic ions or chemically reacts interfering species to produce different species before transmission to the quadrupole (Sader & Ryan, 2020). Matrices that persistently suppress analytical signals are normalized using internal standards, and instrumental drift is corrected by analysis of certified geological reference materials in each batch (Balaram, 2021). These features make ICP-MS, as Schönbächler (2016) concluded, the pre-eminent workhorse of modern geochemical analysis.

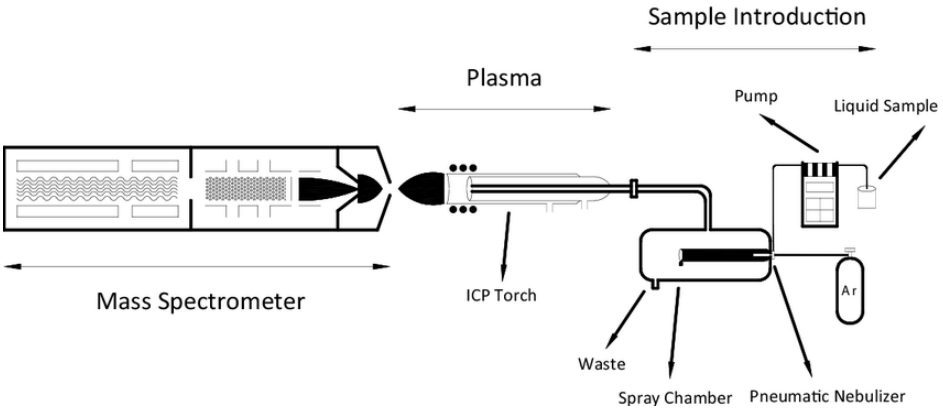

Figure 3.15. Schematic Diagram of ICP-MS (Kashani & Mostaghimi, 2010)

CHAPTER 4
RESULTS AND INTERPRETATION

4.1 Introduction

The Sardhai Formation is part of the Nilawahan Group in the Salt Range, Punjab. It is dated as Early Permian and is dominantly composed of bluish to greenish-grey claystones with minor sand and siltstone interbeds (Gee, 1964). Some exposures also include lavender clays, and chalcopyrite occurrences have been reported in certain sections.

4.2 Data Interpretation

After the laboratory analysis of clay samples through the Inductively Coupled Plasma Mass Spectrometry machine, a Datasheet set has been received, containing more than sixty elements of the periodic table and their concentrations in each of the samples, a signal below the instrument detection limit were reported as BDL (Below Detection Limit) and those above the upper calibration point were reported as ADL (Above Detection Limit), as per the reporting conventions outlined by Zhang and Hu (2019). Their concentration in terms of ppm is interpreted and visualized in form of bar charts.

4.3 Critical Minerals

Critical Minerals present within the datasheet set have been discussed below and are as follows:

4.3.1 Aluminium (Al)

Aluminium is detected across all 22 samples as elaborated in figure 4.1., though its distribution is characterized by ADL readings in US1 and US2, indicating concentrations exceeding the instrument's upper calibration limit, and quantifiable concentrations ranging from 0.7475 ppm (US4) to 9.6654 ppm (US21) across the remaining 20 samples. The ADL readings in US1 and US2 indicate that aluminium concentrations there are extremely elevated. The comparison between (PMJRSS) and (KRSS) for aluminium is complicated by the ADL readings in US1 and US2, the (PMJRSS) samples almost certainly contain the highest absolute aluminium concentrations in the dataset, well above the 9.665 ppm maximum quantified in US21. The two quantified (PMJRSS) values (US3 at 1.967 ppm and US4 at 0.747 ppm) yield a mean of 1.357 ppm considerably lower than the (KRSS) mean of 4.804 ppm across 18 quantified samples. The (KRSS) section shows broad and relatively uniform aluminium distribution, with concentrations ranging from 1.130 ppm (US20) to 9.665 ppm (US21), oxidized samples yield a mean aluminium of 3.883 ppm compared to 5.540 ppm in non-oxidized samples. US21 shows the concentration of 9.665 ppm.

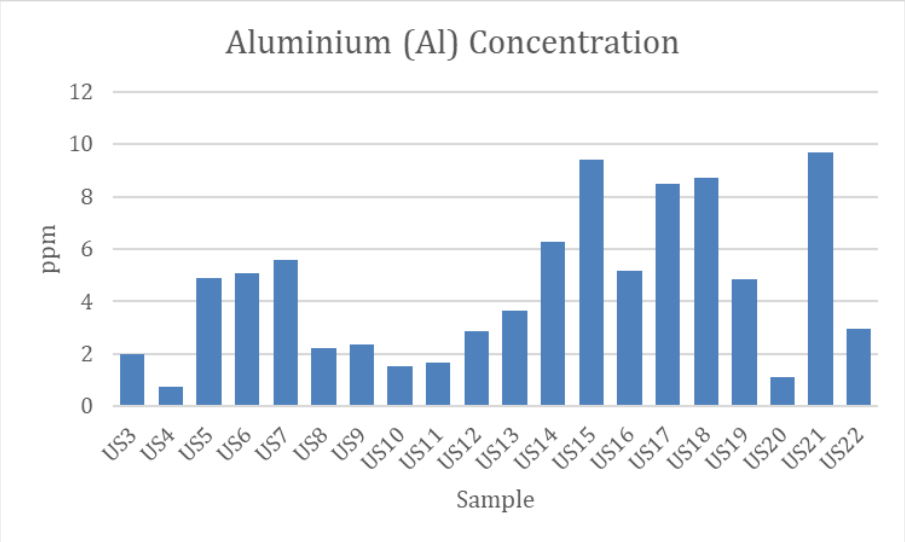

Figure 4.1. Aluminium concentration in samples

4.3.2 Antimony (Sb)

Antimony is detected in 17 of 22 samples as shown in figure 4.2., with concentrations that are relatively consistent across both localities, ranging from BDL in a few samples to a maximum of 0.1313 ppm in US2. The (PMJRSS) mean of 0.0721 ppm is nearly identical to the (KRSS) mean of 0.0728 ppm. Within the Khushab road section, however, the oxidized samples average 0.0785 ppm compared to 0.0678 ppm in the non-oxidized group, whereby oxidized samples show slightly higher antimony concentrations.

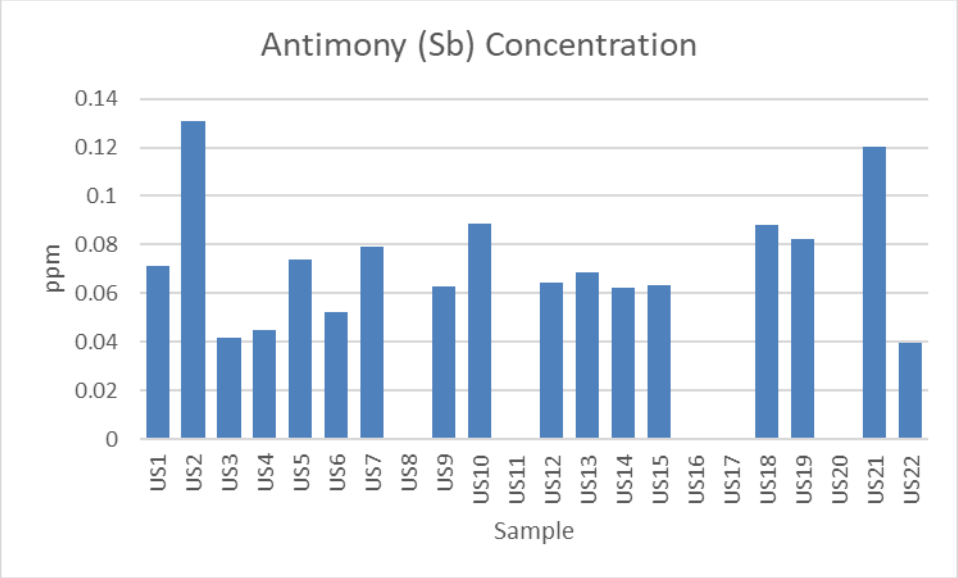

Figure 4.2. Antimony concentration in samples

4.3.3 Arsenic (As)

Arsenic presents the most restricted detection pattern of any industrial element in this dataset, with only a single quantifiable concentration across all 22 samples as shown in figure 4.3., US21 (KRSS non-oxidized) at 0.0745 ppm, while all other 21 samples return BDL.

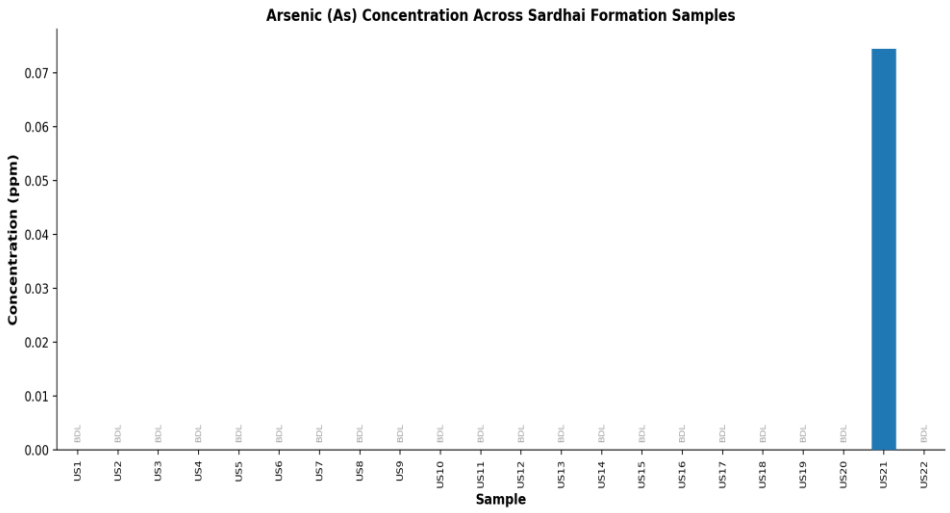

Figure 4.3. Arsenic concentration in samples

4.3.4 Barium (Ba)

Barium presents one of the most geochemically heterogeneous distributions among industrial minerals in this dataset, with concentrations spanning more than three orders of magnitude from BDL (US4, and US11) to a maximum of 3.4720 ppm in US21. The (PMJRSS) section shows US1 (2.3179 ppm) and US2 (2.1375 ppm) being by far the highest barium values in that locality, while US3 (0.0020 ppm) and US4 (BDL) are near or below detection. The (PMJRSS) section yields a mean barium of 1.4858 ppm (three detections in US1, US2, US3 and US4 BDL) which is 6.4 times higher than the (KRSS) mean of 0.2320 ppm across 17 detections. Within the Khushab road section, the contrast between oxidized and non-oxidized samples is the most extreme of any critical mineral in the dataset, oxidized samples average just 0.0197 ppm compared to 0.3806 ppm for non-oxidized samples. US21's extreme barium value (3.472 ppm) which dominates the non-oxidized mean considerably, and excluding US21, the non-oxidized background mean would be approximately 0.087 ppm as shown in figure 4.4.

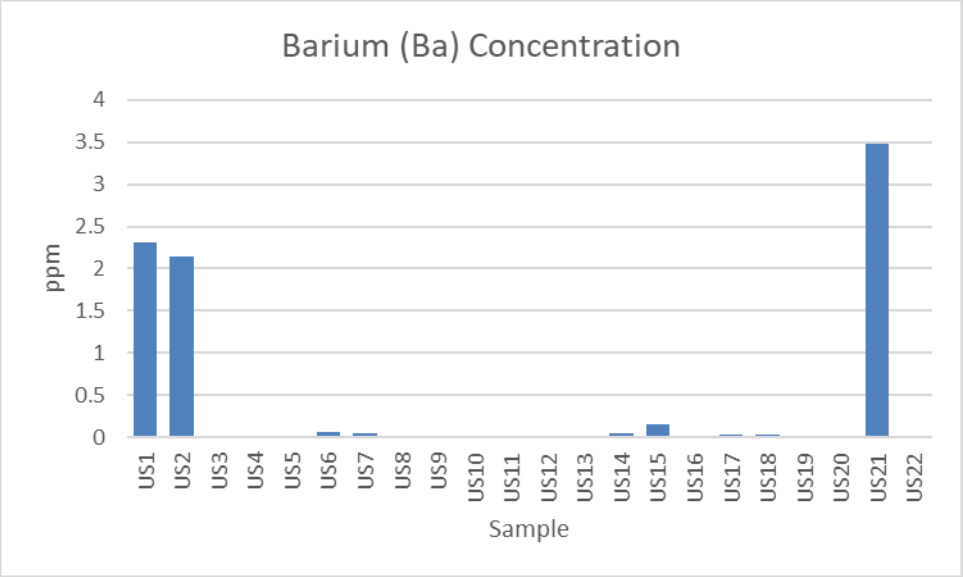

Figure 4.4. Barium concentration in samples

4.3.5 Beryllium (Be)

Beryllium is detected in all 22 samples as shown in figure 4.5., making it along with lithium one of the two critical minerals with a 100% detection rate throughout the dataset. Concentrations range from 0.0039 ppm in US16 to 0.4800 ppm (US1), with a very strong differentiation between the two sampling localities. There are particularly elevated values in US1 (0.4800 ppm) and US2 (0.3294 ppm) from (PMJRSS). The trace level but consistent detection of beryllium across Khushab road samples suggests a background beryllium content inherited from the source terrains of the regional sedimentary succession. The contrast in beryllium concentrations between (PMJRSS and KRSS) is the most pronounced of any critical mineral in the entire dataset. The PMJRSS mean of 0.2165 ppm is approximately 20 times higher than the KRSS mean of 0.0110 ppm. The markedly higher beryllium values in US1 and US2 (compared to US3 and US4) also suggest localized enrichment at the lower or middle part of the Sardhai section. Within the Khushab road section, beryllium shows a moderate difference between oxidized (mean = 0.0080 ppm) and non-oxidized (mean = 0.0135 ppm). US21, registers the highest beryllium value (0.0706 ppm) within the entire Khushab road section.

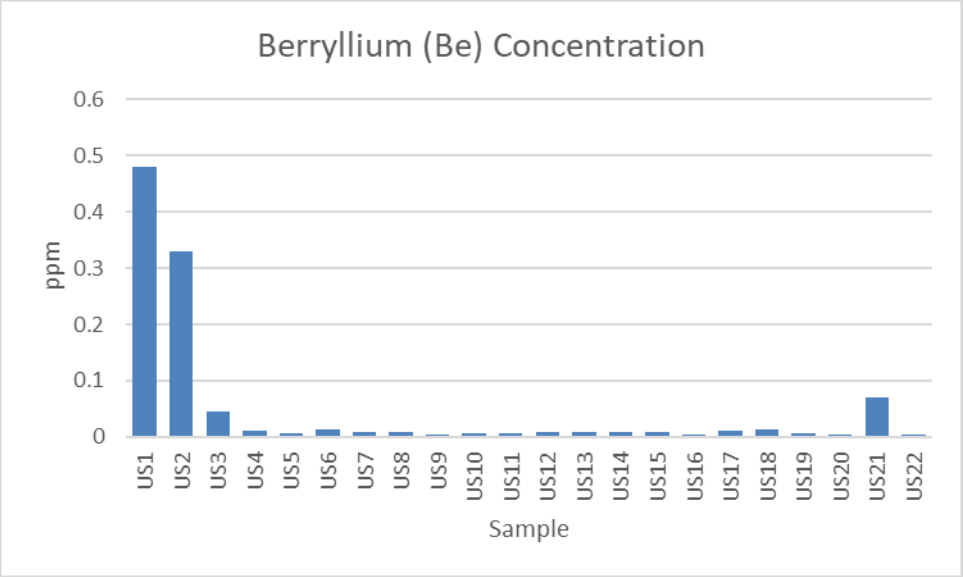

Figure 4.5. Beryllium concentration in samples

4.3.6 Bismuth (Bi)

It is detected in only one of the 22 samples as shown in figure 4.6., US21 (Khushab road, non-oxidized), at a concentration of 0.4115 ppm, while all other 21 samples return BDL.

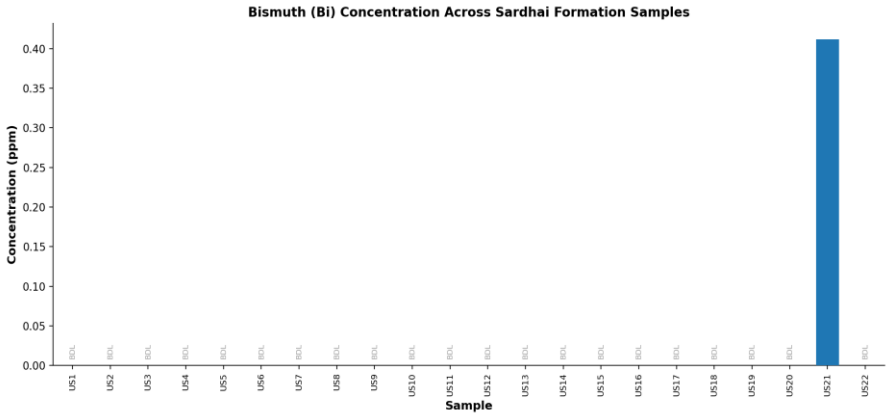

Figure 4.6. Bismuth concentration in samples

4.3.7 Boron (B)

Boron is one of only a handful of elements detected in all 22 samples as shown in figure 4.7., without a single BDL or ADL reading in this dataset, making it one of the most analytically complete elements across the entire geochemical suite. Concentrations range from a minimum of 0.0091 ppm (US4) to a maximum of 1.0557 ppm (US21), with the PMJRSS mean of 0.4585 ppm substantially higher than the KRSS mean of 0.2184 ppm. The PMJRSS section shows a mean boron concentration of 0.4585 ppm, approximately 2.1 times higher than the KRSS mean of 0.2184 ppm. The PMJRSS enrichment is concentrated in the upper two samples (US1 at 0.788 ppm and US2 at 0.974 ppm), while US3 (0.064 ppm) and US4 (0.009 ppm). Within the KRSS section, the oxidized samples yield a mean boron of 0.1453 ppm compared to 0.2768 ppm for non-oxidized samples. US21 (1.056 ppm) is the most boron-enriched KRSS sample.

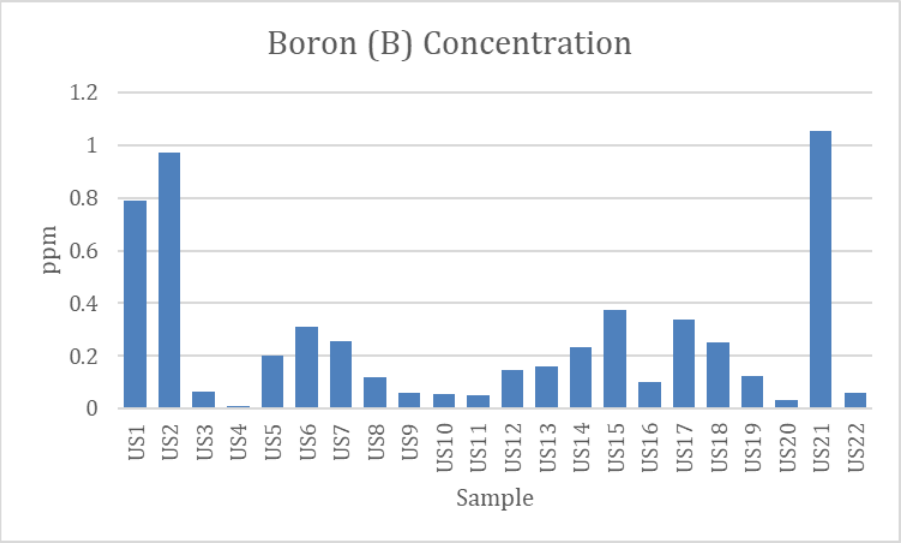

Figure 4.7. Boron concentration in samples

4.3.8 Cerium (Ce)

US1 registers an (ADL) reading, signaling an anomalously elevated concentration that exceeds the instrument's upper calibration range. US2 yields a quantified value of 10.5675 ppm, which is among the highest absolute concentrations of any critical mineral across the entire dataset. By contrast, US3 and US4 drops to 0.0928 ppm and 0.0822 ppm respectively. Within the Khushab road section, cerium is detected in all 18 measurable samples, ranging from 0.0165 ppm (US9) to 4.8843 ppm (US21), with most samples falling in the 0.04–0.31 ppm range. PMJRSS detections (excluding the ADL US1 but including US2's 10.5675 ppm) yield a mean of 3.5808 ppm across three quantified samples, approximately ten times higher than the KRSS mean of 0.3576 ppm. Even discounting the outlier values of US1 (ADL) and US2, US3 and US4 still align broadly with the lower range of KRSS values, Within the Khushab road section, the oxidized samples exhibit a mean cerium concentration of 0.0808 ppm compared to 0.5791 ppm in non-oxidized samples. US21 non-oxidized sample shows 4.8843 ppm as shown in figure 4.8.

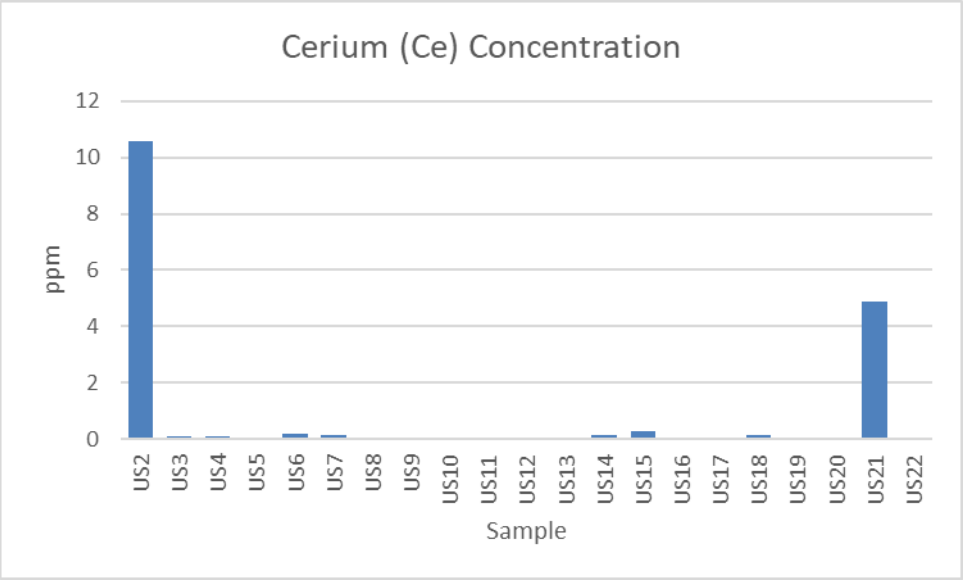

Figure 4.8. Cerium concentration in samples

4.3.9 Chromium (Cr)

Chromium shows a selective detection pattern in this dataset, with quantifiable values in only 5 of the 22 samples as shown in figure 4.9., US1 (0.2657 ppm), US2 (0.7461 ppm) from (PMJRSS) and US14 (0.0009 ppm), US15 (0.0658 ppm), and US21 (0.6233 ppm) from the (KRSS) non-oxidized group. All oxidized KRSS samples are BDL for chromium. The BDL status of most KRSS samples and all oxidized samples indicates that chromium is below analytical detection in most clay dominant facies. PMJRSS section demonstrates distinctly elevated chromium concentrations, with US1 (0.2657 ppm) and US2 (0.7461 ppm) yielding a mean of 0.5059 ppm. KRSS with only three detections giving a mean of 0.2300 ppm.

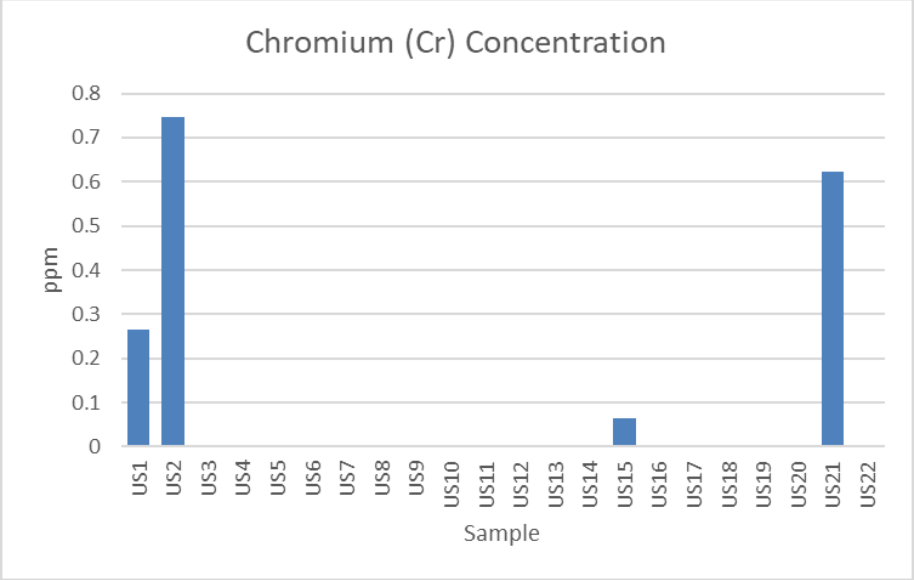

Figure 4.9. Chromium concentration in samples

4.3.10 Copper (Cu)

Copper is detected in all 22 samples without exception as shown in figure 4.10. Concentrations range from 0.0109 ppm (US11, KRSS) to 0.8944 ppm (US21), with the PMJRSS mean of 0.2440 ppm and the KRSS mean of 0.1066 ppm. The

Sardhai Hills section exhibits a mean copper concentration that is 2.3 times higher than the KRSS mean of 0.1066 ppm. The PMJRSS copper distribution is internally heterogeneous, with US3 (0.4255 ppm) and US2 (0.4144 ppm) being the dominant indicators, while US1 (0.0994 ppm) and US4 (0.0367 ppm) are considerably lower. Within the Khushab road section, the oxidized samples yield a mean copper of 0.0616 ppm compared to 0.1426 ppm in non-oxidized samples.

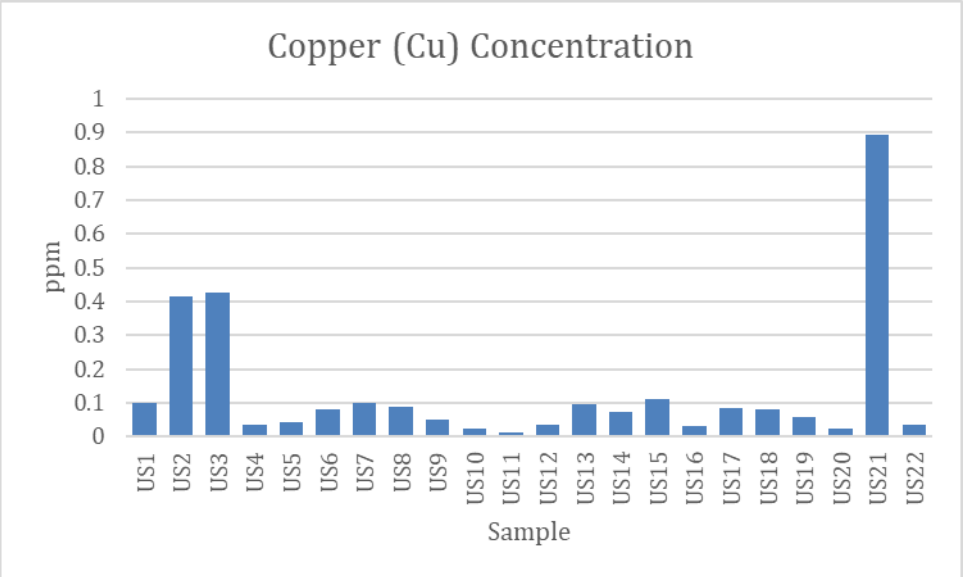

Figure 4.10. Copper concentration in samples

4.3.11 Dysprosium (Dy)

It is detected in 14 of the 22 samples as shown in figure 4.11. Concentrations span from BDL in 8 samples to a maximum of 0.1912 ppm in US1 (PMJRSS), which is the highest Dy value in the entire dataset. US2 contributes 0.0773 ppm, while US3 and US4 are 0.0030 and BDL respectively. Within KRSS, dysprosium is detected in 11 of 18 samples ranging from 0.0014 ppm to 0.1052 ppm (US21). PMJRSS yields a mean dysprosium of 0.0905 ppm across three detections, compared to the KRSS mean of 0.0137 ppm across 11 detections. Within the Khushab road section, oxidized samples yield a mean dysprosium of 0.0052 ppm compared to 0.0185 ppm in non-oxidized samples. The BDL readings in oxidized samples US7, US13, US19 (three of

seven oxidized samples) versus BDL in only two of ten non-oxidized samples quantitatively illustrates the preferential preservation of dysprosium in reducing or geochemically stable environments.

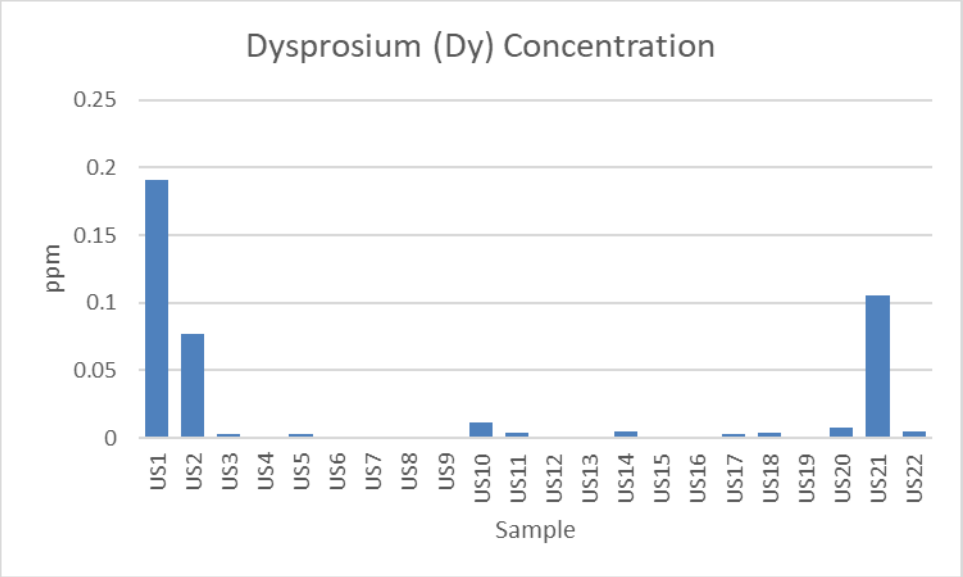

Figure 4.11. Dysprosium concentration in samples

4.3.12 Erbium (Er)

It has quantifiable concentrations in 19 of the 22 samples as shown in figure 4.12., only US3, US19, and US20 return BDL readings. The concentration range spans from BDL to a maximum of 0.1571 ppm in US1 (PMJRSS), with US2 yielding 0.0686 ppm. Within the Khushab road section, erbium ranges from 0.0035 ppm (US22) to 0.1044 ppm (US21), with most samples falling in the 0.004–0.017 ppm range. PMJRSS shows a mean erbium of 0.0770 ppm (three detections), compared to KRSS mean of 0.0159 ppm across 16 detections. Within the KRSS section, the oxidized samples yield a mean erbium of 0.0099 ppm compared to 0.0206 ppm for non-oxidized samples. The persistent detection of erbium in oxidized samples, ranging from 0.0056 to 0.0169 ppm confirms that erbium's host phase in the Kallar Kahar oxidized zone is comparatively resistant to oxidative weathering.

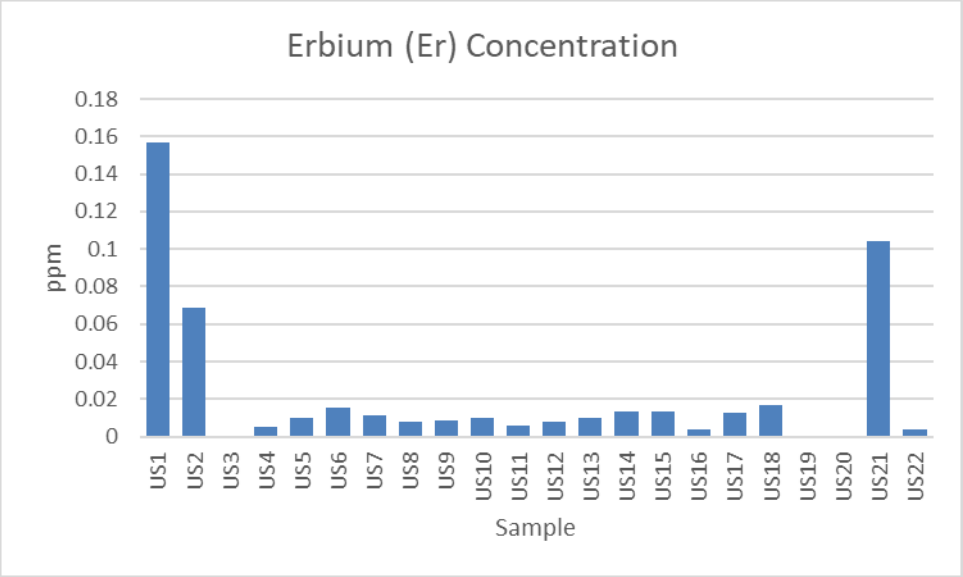

Figure 4.12. Erbium concentration in samples

4.3.13 Europium (Eu)

In this dataset, europium is detected in 20 of 22 samples (BDL only in US11 and US16) as shown in figure 4.13, with concentrations ranging from 0.0017 ppm (US14, KRSS non-oxidised) to 0.1791 ppm (US1, PMJRSS). The PMJRSS mean of 0.0731 ppm is significantly higher than the KRSS mean of 0.0083 ppm. PMJRSS mean europium concentration of 0.0731 ppm, is approximately 8.8 times higher than the KRSS mean of 0.0083 ppm.

There is elevated europium in US1 (0.1791 ppm) and US2 (0.1037 ppm) compared to US3 (0.0046 ppm) and US4 (0.0048 ppm). Within the Khushab road section, oxidized samples average 0.0044 ppm compared to the non-oxidized mean of 0.0114 ppm.

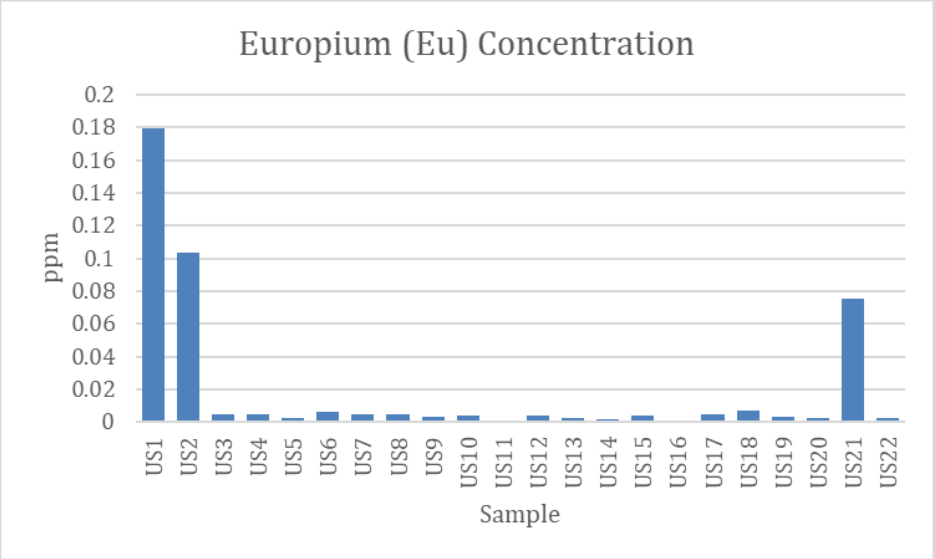

Figure 4.13. Europium concentration in samples

4.3.14 Gadolinium (Gd)

In this dataset, gadolinium is detected in all 22 samples without a single BDL result as shown in figure 4.14. Concentrations range from a minimum of 0.0080 ppm (US4) to a maximum of 1.8099 ppm (US1), with US2 also registering a markedly elevated 0.9676 ppm. The PMJRSS mean of 0.7013 ppm stands in stark contrast to the KRSS mean of 0.0803 ppm. Within the Khushab road section, the oxidized samples yield a mean gadolinium of 0.0301 ppm compared to 0.1206 ppm in non-oxidized samples.

While the contrast is real and consistent with oxidizing conditions, the fact that gadolinium remains detectable in all oxidized samples (ranging from 0.0105 to 0.0487 ppm) confirms that it is comparatively more resistant to oxidative leaching, pointing to a more stable host phase.

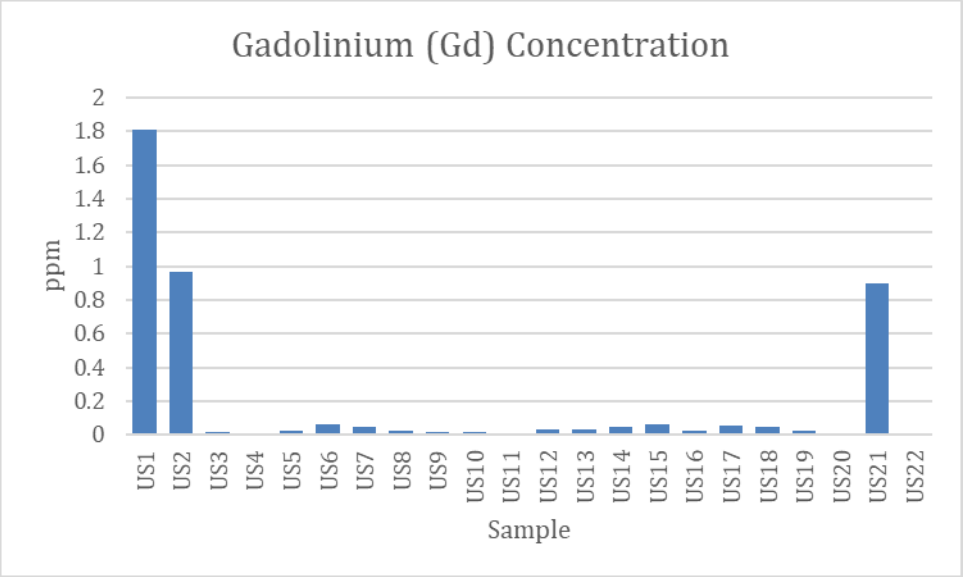

Figure 4.14. Gadolinium concentration in samples

4.3.15 Gallium (Ga)

Gallium is detected in 17 out of 22 samples as shown in figure 4.15, with concentrations ranging from below detection in several KRSS samples to a maximum of 0.4360 ppm in the US21 sample. The PMJRSS samples average 0.1998 ppm gallium, more than twice the KRSS mean of 0.0961 ppm, a pattern broadly consistent with the higher aluminium enrichment noted in the PMJRSS clays (confirmed by the aluminium values in the broader dataset, which are ADL for US1 and US2).

Within the Khushab road section, the oxidized samples yield a mean gallium concentration of 0.0601 ppm compared to 0.1381 ppm in the non-oxidised samples. The oxidized sample (US13) shows BDL gallium.

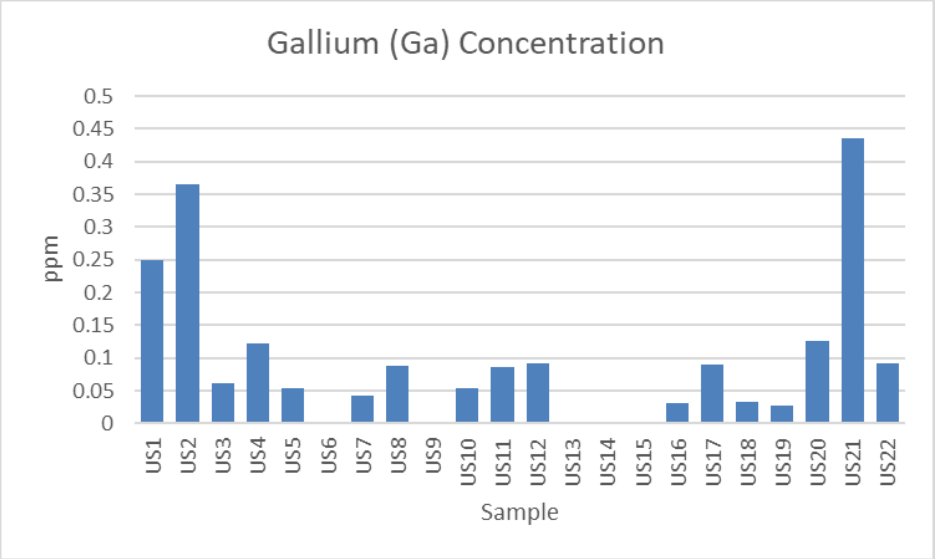

Figure 4.15. Gallium concentration in samples

4.3.16 Hafnium (Hf)

Hafnium is detected in 15 of the 22 samples as shown in figure 4.16, with concentrations generally low and ranging from 0.0021 ppm (US12) to 0.0228 ppm (US2). Higher Hf values in US1 (0.0136 ppm) and US2 (0.0228 ppm) from PMJRSS. The relatively uniform and low hafnium concentrations across KRSS samples indicate a sparse but consistent back.

The PMJRSS samples yield a mean hafnium concentration of 0.0131 ppm, compared to 0.0055 ppm for KRSS, a 2.4-fold enrichment in PMJRSS. Within Khushab road section, the oxidized (mean = 0.0056 ppm) and non-oxidized (mean = 0.0053 ppm) samples show a very low difference in hafnium concentrations.

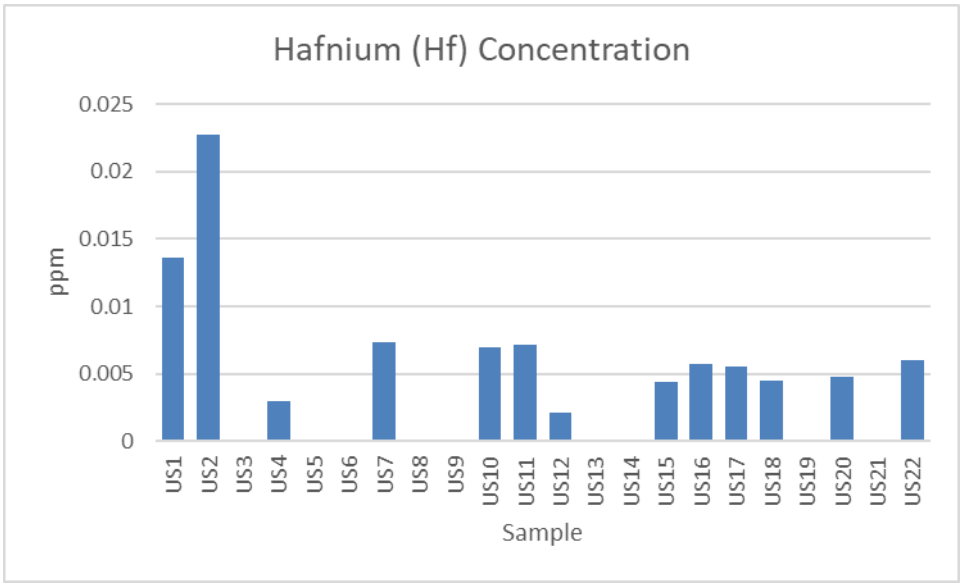

Figure 4.16. Hafnium concentration in samples

4.3.17 Holmium (Ho)

Holmium occupies a unique position in this dataset as the only critical mineral that is detected exclusively in the PMJR section, with complete BDL readings across all 18 KRSS samples as shown in figure 4.17. Concentrations in PMJRSS are detected in three of four samples: US1 at 0.0120 ppm, US2 at 0.0001 ppm, and US4 at 0.0064 ppm, while US3 returns BDL. The PMJRSS mean of 0.0062 ppm across the three detections is low but analytically meaningful.

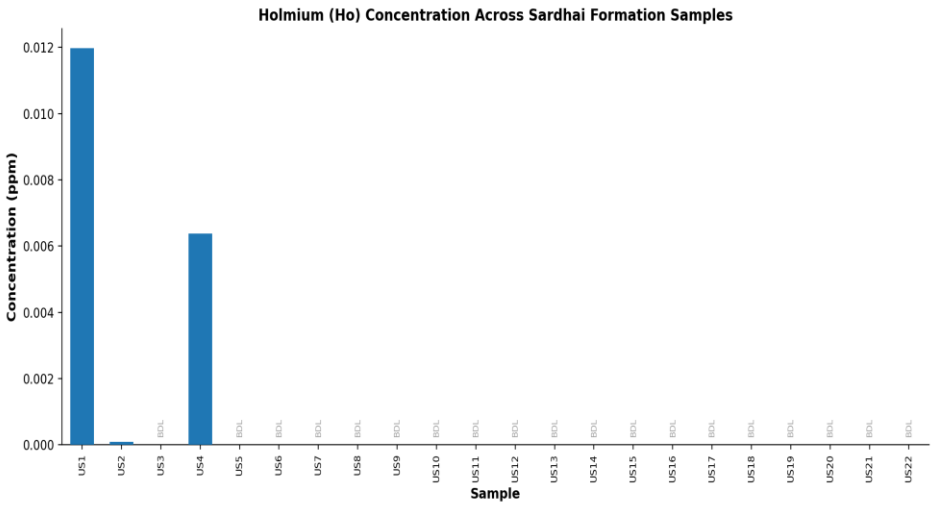

Figure 4.17. Holmium concentration in samples

4.3.18 Iridium (Ir)

It is detected in 17 of the 22 samples as shown in figure 4.18, with BDL readings in US1, US8, US17, US20, and US22, and concentrations ranging from 0.0058 ppm (US4) to 0.0472 ppm (US21, KRSS non-oxidized). The overall concentration range is remarkably compressed with 15 of the 17 detected values falling between 0.0131 and 0.0288 ppm.

The PMJRS section yields three iridium detections (US2 at 0.0288 ppm, US3 at 0.0289 ppm, US4 at 0.0058 ppm; US1 BDL) for a mean of 0.0212 ppm, nearly identical to the KRSS mean of 0.0216 ppm across 14 detections making iridium one of the few elements to show near-perfect equivalence between both localities. Within the Khushab road section, the oxidized samples yield a mean iridium of 0.0194 ppm compared to 0.0238 ppm in non-oxidized samples.

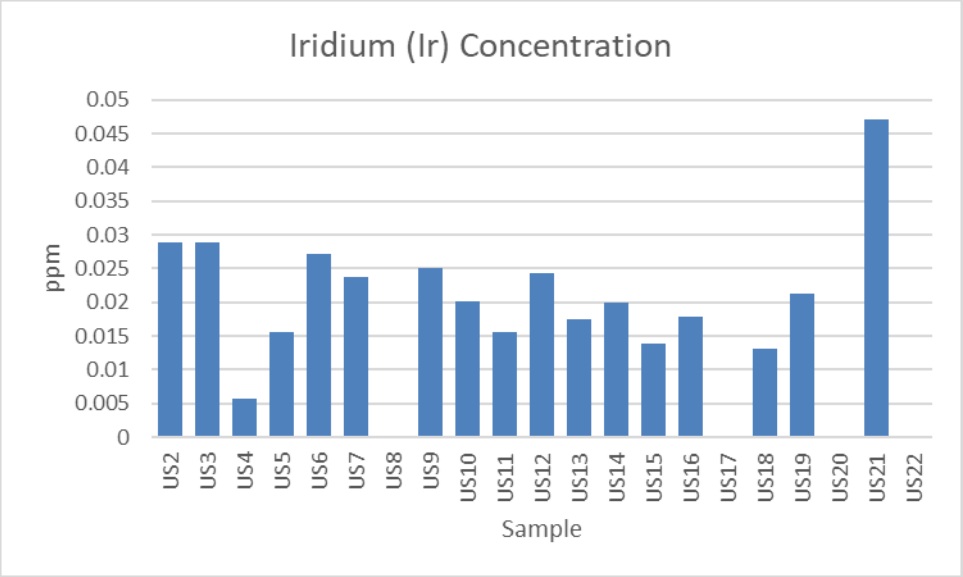

Figure 4.18. Iridium concentration in samples

4.3.19 Lanthanum (La)

Concentrations span from 0.0022 ppm (US4) to 8.0116 ppm (US1), with the PMJR section yielding a mean of 2.9969 ppm across all four samples. In the Khushab road section, lanthanum is detected in all 18 samples, ranging from 0.0108 ppm (US5) to 1.3868 ppm (US21), with most of the samples clustering in the 0.02–0.09 ppm range.

The PMJRSS mean of 2.9969 ppm is approximately 27 times higher than the KRSS mean of 0.1104 ppm. Within the Khushab road section, the comparison between oxidized and non-oxidized samples reveals a substantial 5.9-fold difference with the oxidized samples average just 0.0298 ppm compared to 0.1748 ppm in non-oxidized samples. US21 shows a value of 1.3868 ppm as shown in figure 4.19.

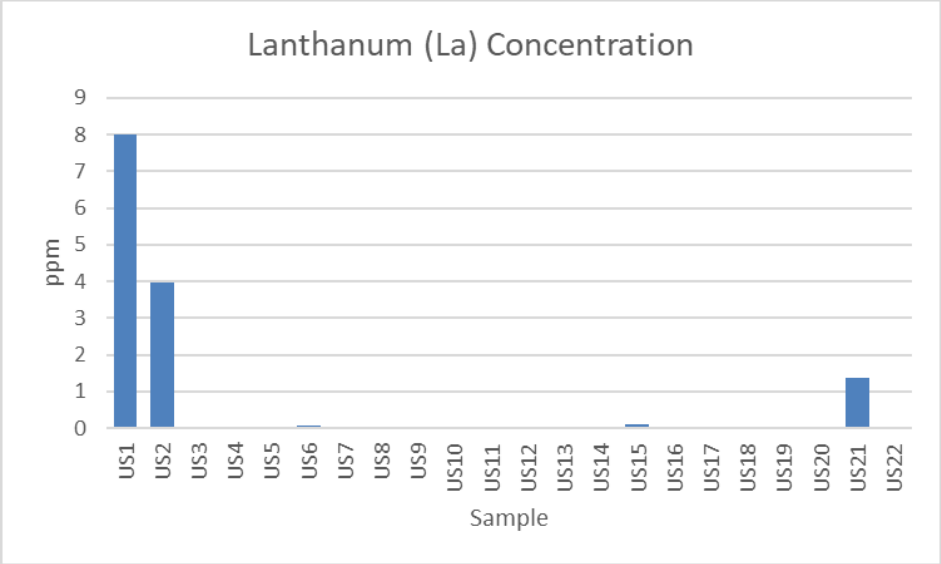

Figure 4.19. Lanthanum concentration in samples

4.3.20 Lead (Pb)

Lead displays one of the most restricted detection patterns of any economic element in the dataset, with quantifiable concentrations in only 5 of the 22 samples as shown in figure 4.20., US1 (0.4701 ppm) and US2 (0.3655 ppm) from PMJRSS, US7 (0.0123 ppm) from the KRSS oxidized group, US15 (0.0275 ppm) from the KRSS non-oxidized group, and US21 (0.6550 ppm).

The PMJRSS section yields a mean lead concentration of 0.4178 ppm across the two detections in US1 and US2. Within the Khushab road section, the detection pattern is prominent, the oxidized group yields only one detection (US7 at 0.0123 ppm), while the non-oxidized group yields two detections (US15 at 0.0275 ppm and US21 at 0.6550 ppm). The non-oxidized mean of 0.3413 ppm (dominated by US21) far exceeds the single oxidized detection of 0.0123 ppm.

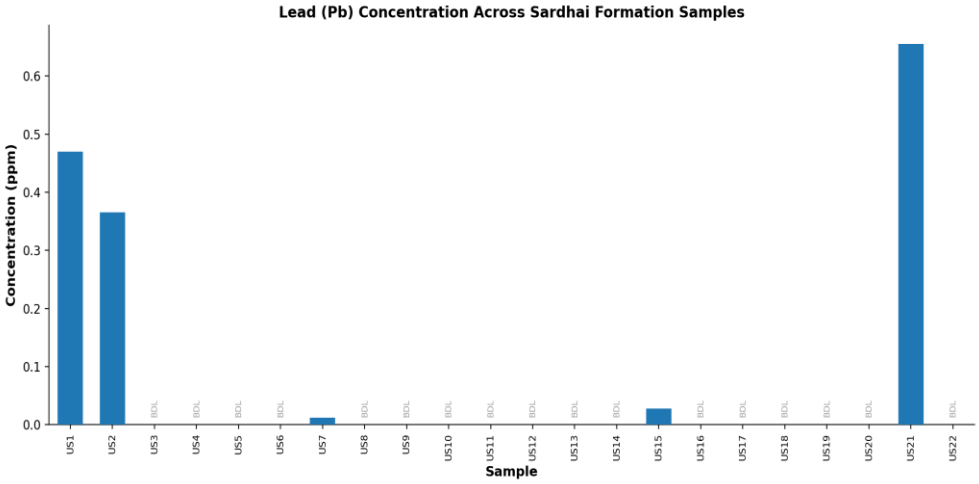

Figure 4.20. Lead concentration in samples

4.3.21 Lithium (Li)

Lithium is one of the most analytically significant critical minerals in this dataset, being the only element to register quantifiable values across all 22 samples without a single Below Detection Limit (BDL) result as shown in figure 4.21. Concentrations range from as low as 0.0314 ppm US4 Peeran-e-Morjung roadside section (PMJRSS), to as high as 1.8435 ppm US21, Khushab roadside section (KRSS), with the PMJRSS samples averaging 0.4978 ppm and KRSS samples averaging 0.2120 ppm. The presence of lithium across both localities suggests that it is structurally incorporated into the clay mineral lattice. There are elevated concentrations in US1 (0.6389 ppm) and US2 (1.2320 ppm) from PMJRSS, and particularly in US21 (1.8435 ppm) from KRSS. The PMJRSS samples (US1–US4) exhibit a notably higher mean lithium concentration of 0.4978 ppm compared to the Khushab section (US5–US22) mean of 0.2120 ppm, suggesting that the clay-rich lithologies of PMJRSS are more lithium-enriched, possibly reflecting differences in provenance, depositional environment, or degree of clay mineralogy maturation. Within PMJRSS, a marked internal heterogeneity is apparent, with US1 and US2 showing values approximately 7–40 times higher than US3 and US4, hinting at spatial variability in lithium incorporation across the section. Concerning the oxidized versus

non-oxidized subsets within the Khushab road section, the oxidized samples (US7, US8, US10–US13, US18, US19) average a substantially lower 0.0990 ppm compared to the non-oxidized samples (US5, US6, US9, US14–US17, US20–US22) which average 0.3024 ppm. This suggests that oxidizing diagenetic conditions may have caused lithium to leach from clay structures. In contrast, the reducing or chemically stable conditions of the non-oxidized samples appear to have preserved lithium within the clay matrix more effectively.

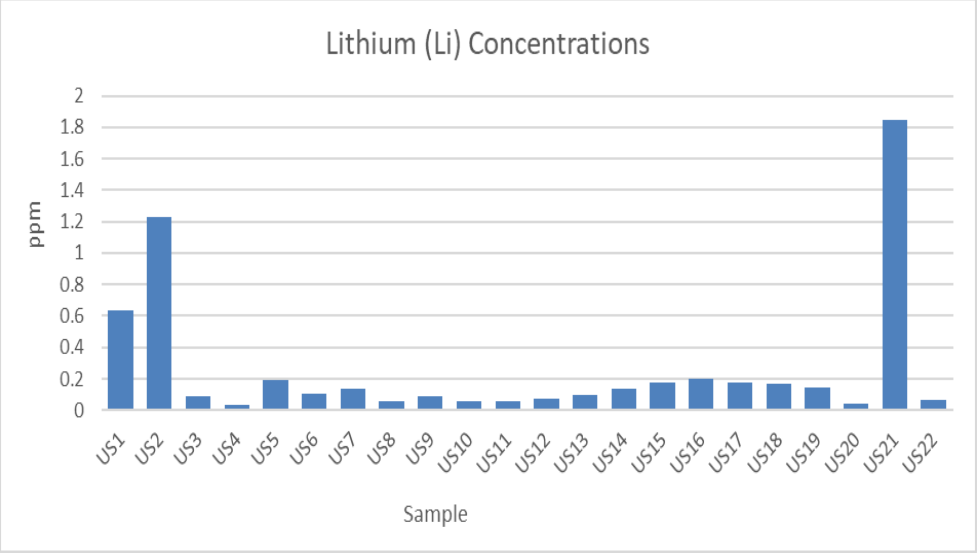

Figure 4.21. Lithium concentrations in samples

4.3.22 Lutetium (Lu)

It is detected in 21 of the 22 samples in this dataset (only US9 returns BDL) as shown in figure 4.22. Concentrations range from a minimum of 0.0007 ppm (US8, oxidized) to a maximum of 0.0977 ppm (US2), with US1 yielding 0.0931 ppm and the PMJRSS mean reaching 0.0489 ppm. Khushab road section samples average 0.0128 ppm across 17 detections, ranging from near-detection limit values in the oxidized samples to 0.1298 ppm in US21. The PMJRSS mean lutetium concentration of 0.0489 ppm is approximately 3.8 times higher than the KRSS mean of 0.0128 ppm. Within the Khushab road section, the oxidized samples yield a mean lutetium of 0.0044 ppm compared to the non-oxidized mean of 0.0204 ppm. Notably, lutetium is

detected in all oxidized samples (ranging from 0.0007 to 0.0080 ppm), indicating a persistent residual lutetium signal in the oxidized zone despite significant overall depletion. This persistent detection in oxidized samples, combined with the comparatively moderate enrichment ratio between non-oxidized and oxidized samples (4.7-fold), reflects lutetium's status as geochemically immobile. US21 of non-oxidized group shows 0.1298 ppm, an exceptional value that is approximately 9 times the next highest non-oxidized sample (US15 at 0.0132 ppm).

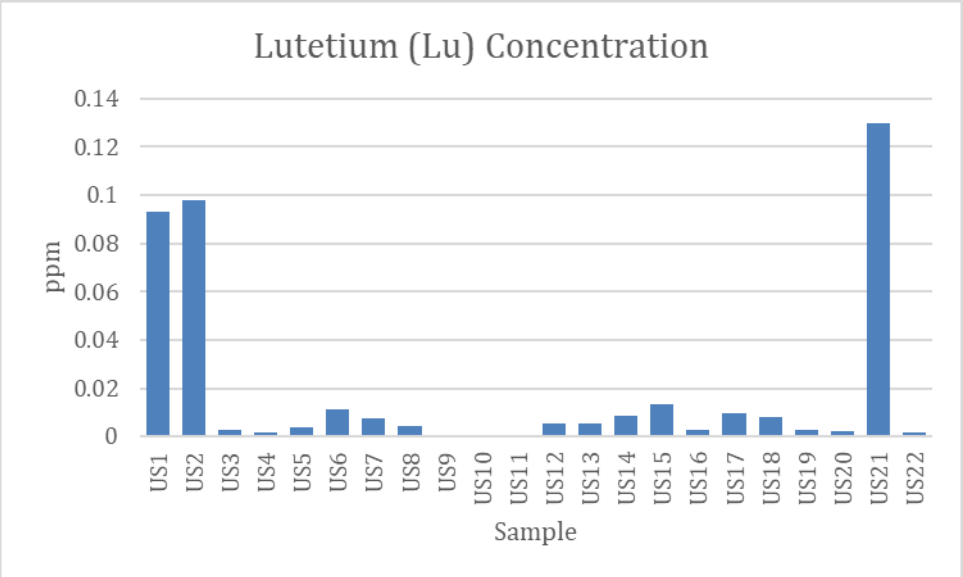

Figure 4.22. Lutetium concentration in samples

4.3.23 Magnesium (Mg)

Magnesium follows the same pattern of near-universal ADL enrichment as calcium and potassium, with 20 of the 22 samples exceeding the instrument's upper calibration limit as shown in figure 4.23. The only quantifiable magnesium values in the entire dataset are US3 (0.9228 ppm) and US4 (0.4051 ppm).

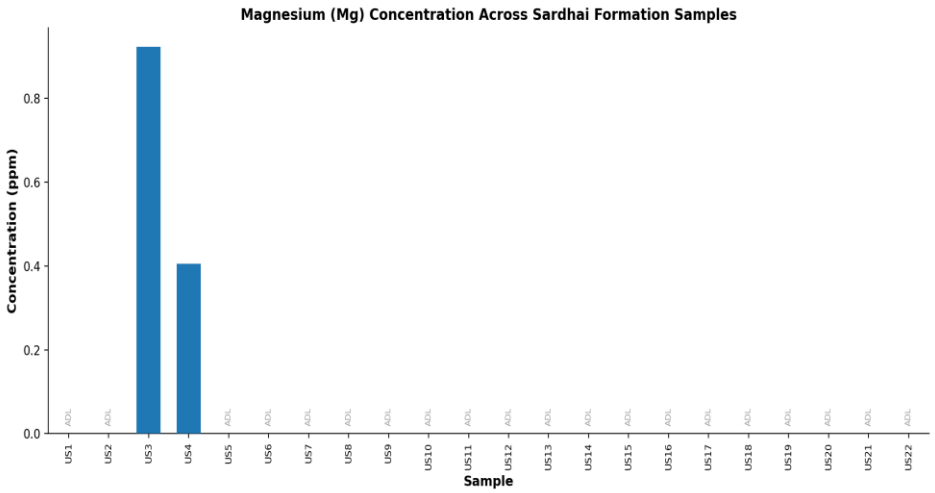

Figure 4.23. Magnesium concentration in samples

4.3.24 Manganese (Mn)

Manganese is one of the most geochemically dynamic critical minerals in this dataset, with the highest absolute value among all detected critical minerals. Concentrations are available for 21 of the 22 samples (US21 registering ADL) as shown in figure 4.24., ranging from 0.0232 ppm (US4) to 8.8176 ppm (US2). There is a significant spike in values in PMJRSS (particularly US1 at 4.5800 ppm and US2 at 8.8176 ppm) compared to most Khushab roadside section samples.

The PMJRSS samples register a mean manganese concentration of 3.3675 ppm, substantially elevated compared to the KRSS mean of 1.9189 ppm. Within the Khushab road section, the oxidized samples average 1.4820 ppm compared to 2.3073 ppm in the non-oxidized samples.

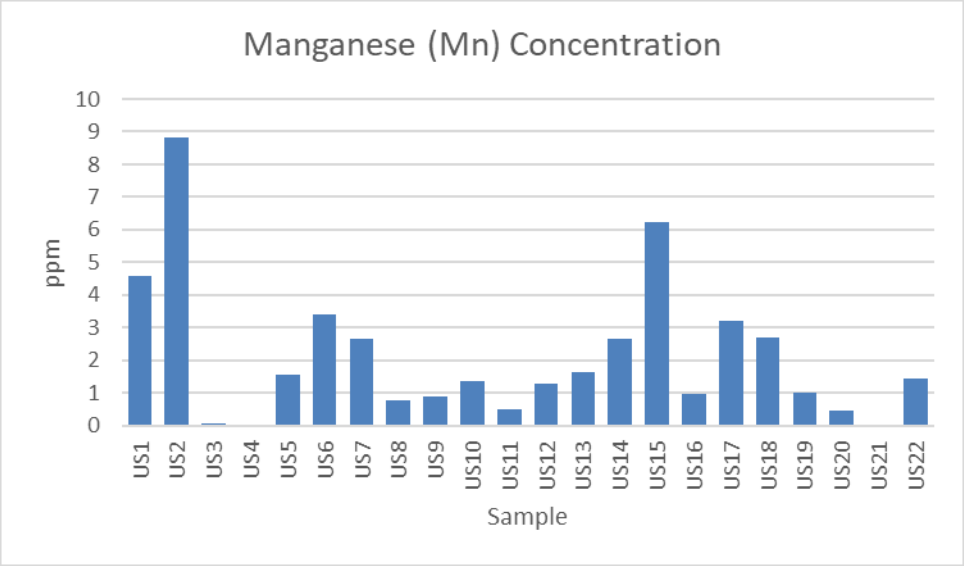

Figure 4.24. Manganese concentration in samples

4.3.25 Neodymium (Nd)

Quantifiable concentrations range from below detection in US4 and several KRSS samples to a maximum of 4.9012 ppm in US1, with US2 also elevated at 2.8157 ppm. In the KRSS, neodymium is detected in 15 of 18 samples (US11, US19, US20 being BDL), with concentrations ranging from 0.0114 ppm (US5) to 1.5335 ppm (US21).

The PMJRS section exhibits a mean neodymium concentration of 2.5757 ppm (based on three detections in US1, US2, and US3 whereas US4 is BDL), compared to the KRSS mean of 0.1283 ppm. Within the KRS section, the comparison between oxidized and non-oxidized subsets is particularly pronounced for neodymiun where oxidized samples average 0.0216 ppm across 6 detections, while non-oxidized samples average 0.1994 ppm across 9 detections as shown in figure 4.25.

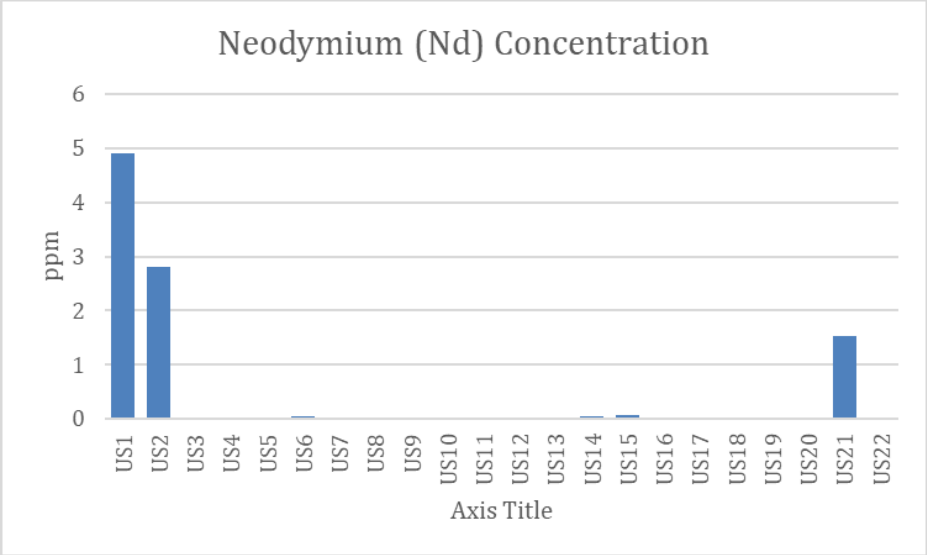

Figure 4.25. Neodymium concentration in samples

4.3.26 Nickel (Ni)

Nickel is detected in 11 of the 22 samples as shown in figure 4.26, with concentrations spanning from below detection in many samples to a notable maximum of 0.4195 ppm in US21. Within the PMJR section, US1 and US2 register 0.2556 ppm and 0.3789 ppm respectively, while US3 and US4 are BDL. The PMJRSS samples show elevated nickel, with a mean of 0.3173 ppm across the two detections (US1 and US2), considerably higher than the KRSS mean of 0.0662 ppm.

Within the Khushab road section, the contrast between oxidized and non-oxidized samples is striking, oxidized samples average only 0.0192 ppm compared to the non-oxidized mean of 0.0897 ppm.

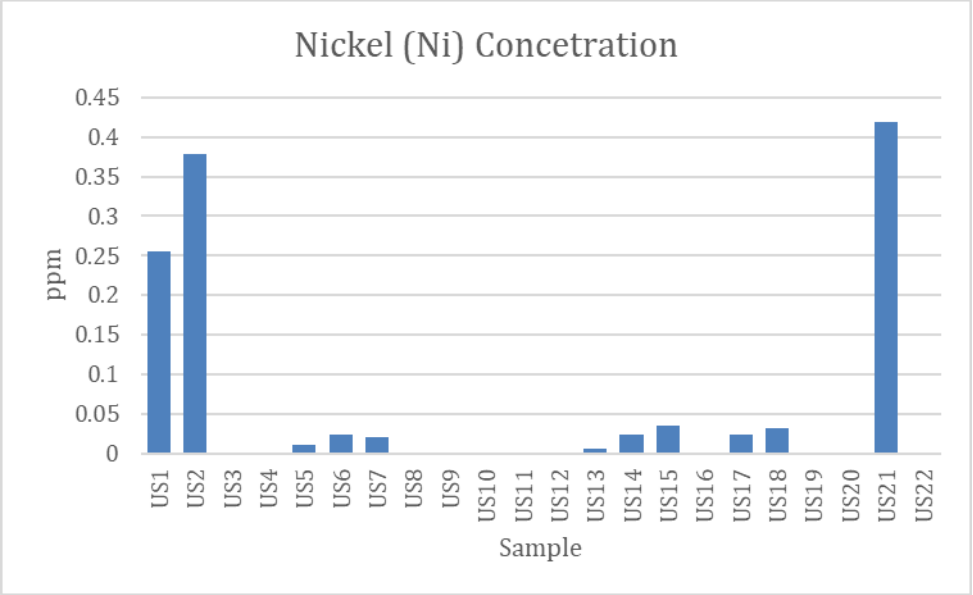

Figure 4.26. Nickel concentration in samples

4.3.27 Niobium (Nb)

Niobium is detected in 11 of the 22 samples as shown in figure 4.27, reflecting a more selective geochemical distribution compared to the more pervasive critical minerals discussed above. Detected concentrations range from a minimum of 0.0028 ppm (US13) to a maximum of 0.4247 ppm in US21 (non-oxidized), with the PMJRSS samples (US1 at 0.1499 ppm and US2 at 0.1694 ppm) registering among the highest values alongside US21. The PMJRSS samples yield a mean niobium concentration of 0.1596 ppm (based on two detections in US1 and US2), which is considerably higher than the KRSS mean of 0.0616 ppm.

The remaining two PMJRSS samples (US3 and US4) are BDL. Within the Khushab road section, the oxidized samples display a mean of just 0.0083 ppm, which is significantly lower than the non-oxidized mean of 0.0883 ppm, with only 3 detections in the oxidized group versus 6 in the non-oxidized group. US21 remains the single highest-niobium sample in the entire Kushab road section with 0.4247 ppm.

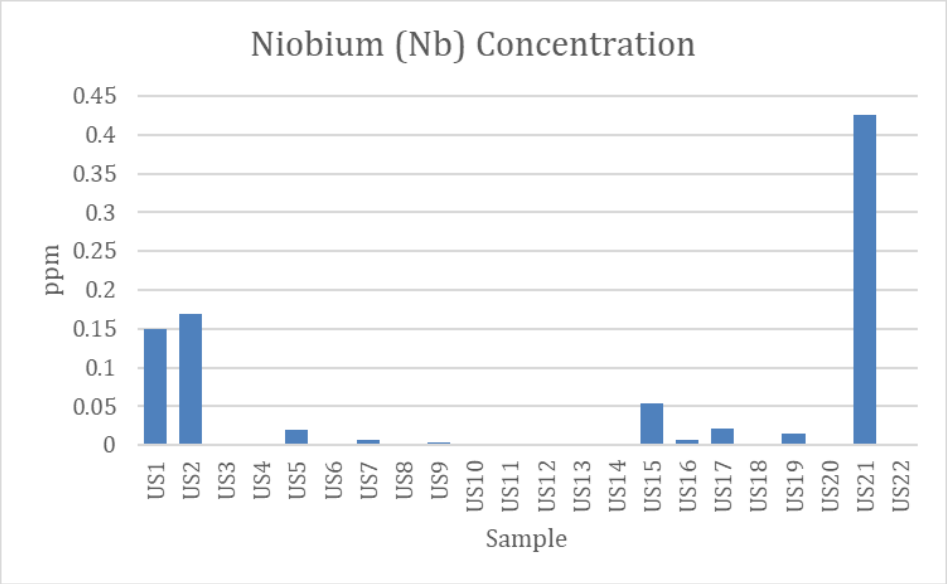

Figure 4.27. Niobium concentration in samples

4.3.28 Palladium (Pd)

Palladium is detected in 11 of the 22 samples as shown in figure 4.28, with concentrations ranging from BDL in 11 samples to a maximum of 1.9802 ppm. The background palladium concentrations in samples showing detection excluding US21, fall in the range 0.0394–0.1202 ppm. The PMJRS section yields two detections for palladium, US3 (0.0935 ppm) and US4 (0.0779 ppm) for a mean of 0.0857 ppm, while the Khushab road section shows a mean of 0.2830 ppm across 9 detections, dominated by the US21 value of 1.9802 ppm.

Excluding US21, the KRSS background palladium mean (US5, US6, US7, US8, US9, US11, US16, US20) averages 0.0793 ppm. Within the Khushab road section, the oxidized samples yield a mean of 0.0468 ppm (3 detections: US7, US8, US11) compared to the non-oxidized mean of 0.4011 ppm (6 detections: US5, US6, US9, US16, US20, US21).

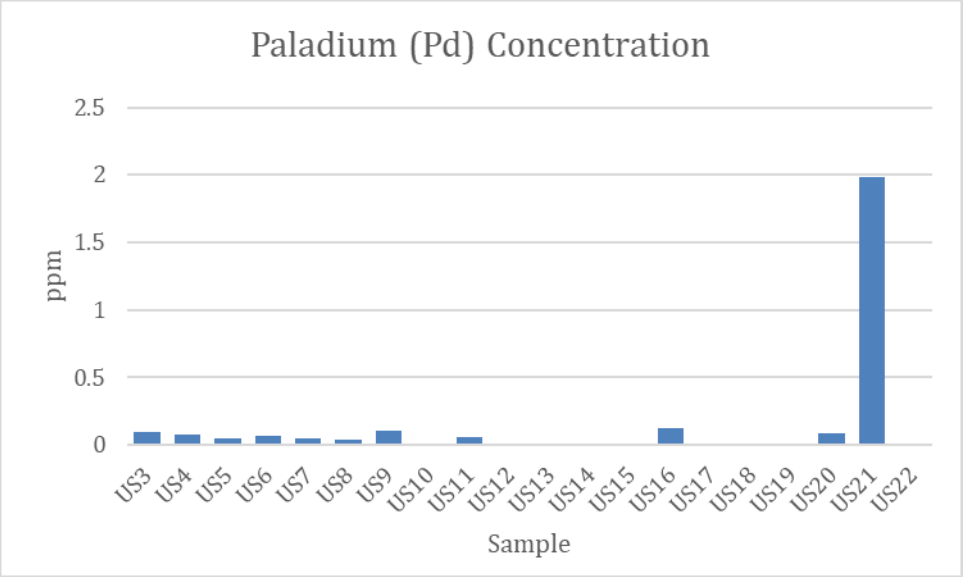

Figure 4.28. Palladium concentration in samples

4.3.29 Phosphorus (P)

Phosphorus is detected in 19 of the 22 samples as shown in figure 4.29, with ADL readings in US6, US17, and US21. Concentrations range from a minimum of 1.9467 ppm (US11, KRSS oxidized) to 10.4009 ppm (US15, KRSS non-oxidized), with the PMJRSS mean of 5.4963 ppm and the KRSS mean of 5.5789 ppm being remarkably similar.

The near identical means for phosphorus in PMJRSS (5.4963 ppm) and KRSS (5.5789 ppm) is one of the most geochemically informative patterns in the entire dataset. Within the Khushab road section, oxidized samples yield a mean phosphorus of 5.410 ppm compared to 5.771 ppm for non-oxidized samples.

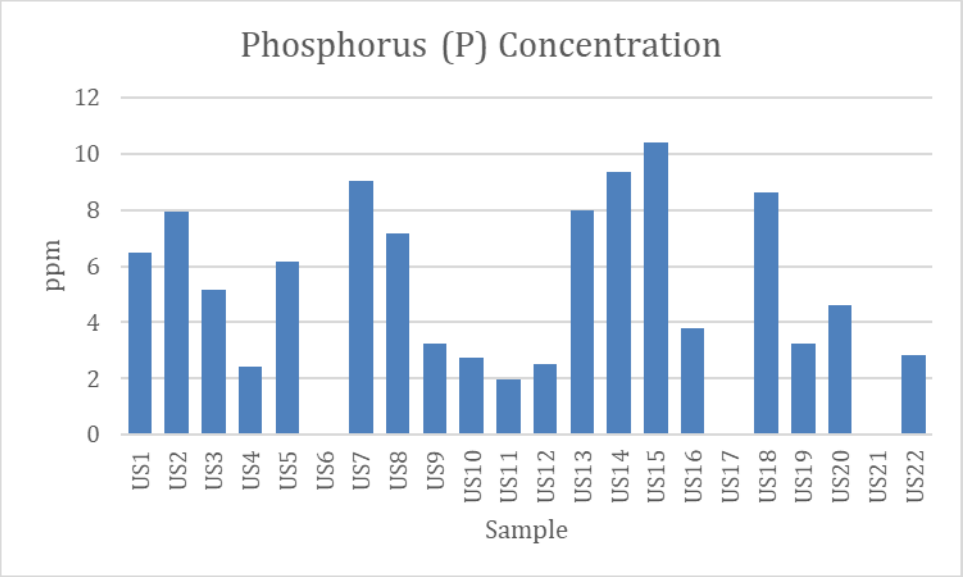

Figure 4.29. Phosphorus concentration in samples

4.3.30 Platinum (Pt)

Platinum is the scarcest economically important element in this dataset, detected in only 3 of the 22 samples as shown in figure 4.30., US9 (0.0099 ppm, KRSS non-oxidized), US19 (0.0089 ppm, KRSS oxidized), and US22 (0.0111 ppm, KRSS non-oxidized). All other samples return BDL.

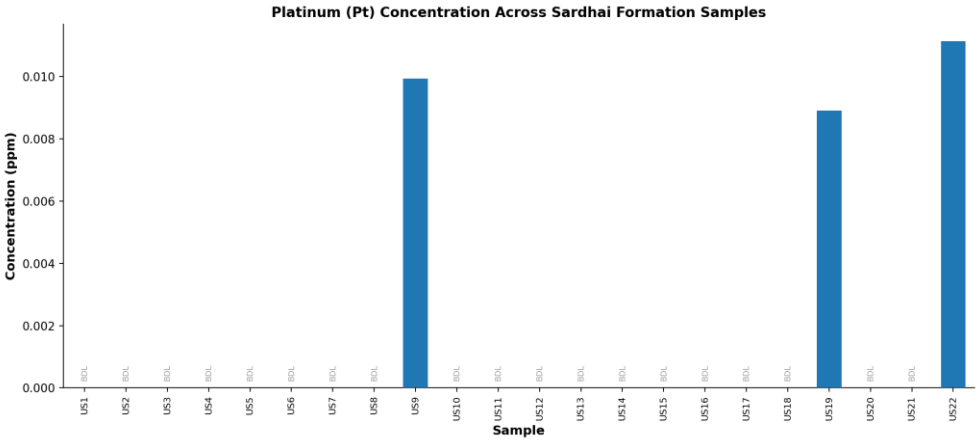

Figure 4.30. Platinum concentration in samples

4.3.31 Potassium (K)

Potassium, like calcium, is almost entirely characterized by ADL readings across the dataset, 21 of the 22 samples exceed the instrument's upper calibration limit, with only US22 yielding a quantifiable concentration of 2.6944 ppm. This overwhelming ADL dominance indicates that potassium concentrations throughout the sections are extremely elevated and relatively uniform as shown in figure 4.31.

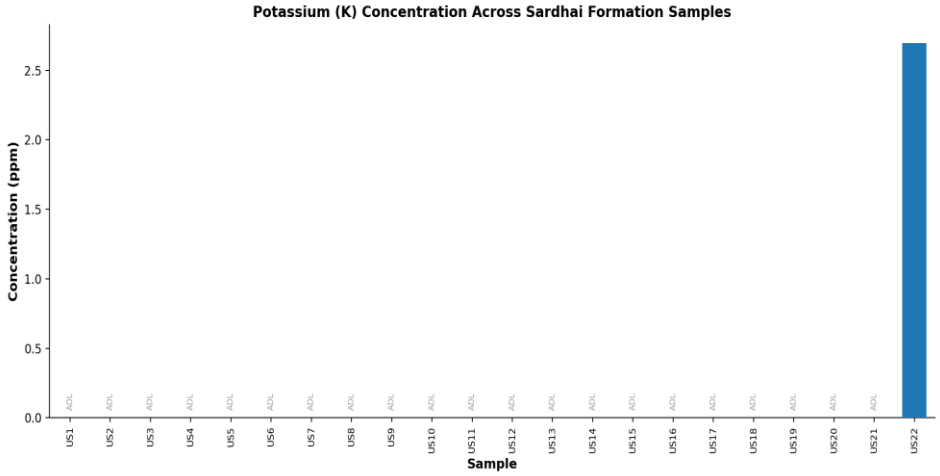

Figure 4.31. Potassium concentration in samples

4.3.32 Praseodymium (Pr)

Concentrations range from a maximum of 4.3866 ppm in US21 (non-oxidised) to a minimum of 0.0437 ppm in US20, with praseodymium detected in all 18 KRSS samples. PMJRSS mean for praseodymium is 1.1298 ppm across three samples. The PMJRSS versus KRSS comparison for praseodymium yields a mean of (1.1298 ppm versus 0.5833 ppm). Within the Khushab road section, the oxidized samples average 0.2927 ppm compared to the non-oxidized mean of 0.8158 ppm. The high individual values in non-oxidized samples such as US15 (1.0100 ppm), US21 (4.3866 ppm), US14 (0.6170 ppm), and US17 (0.4137 ppm) confirm that praseodymium enrichment

within the non-oxidized group is broadly distributed rather than concentrated in a single anomalous horizon as shown in figure 4.32.

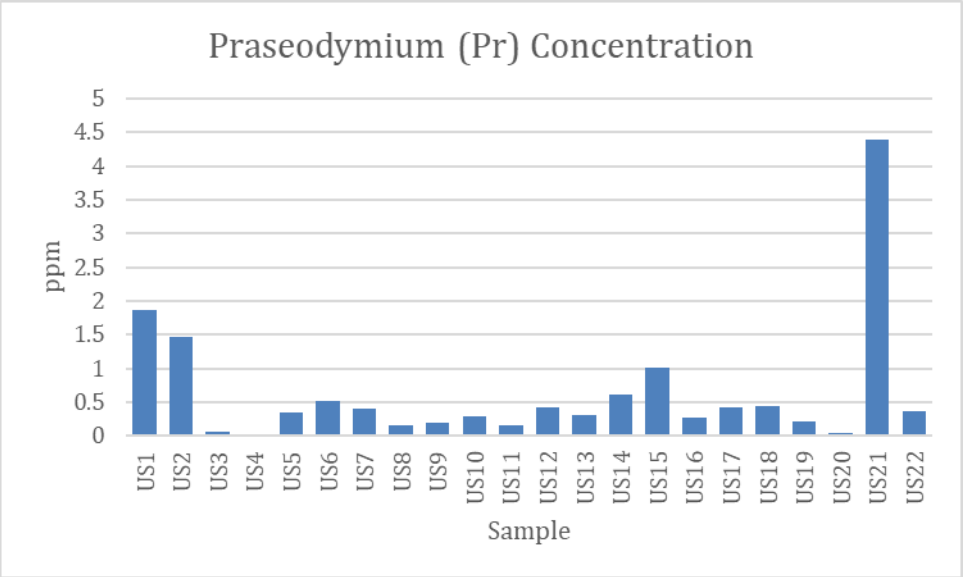

Figure 4.32. Praseodymium concentration in samples

4.3.33 Rhodium (Rh)

Rhodium is entirely absent from all 22 samples, returning BDL readings across the complete dataset, with no exceptions.

4.3.34 Rubidium (Rb)

Rubidium is detected in 18 of the 22 samples (BDL in US5, US6, US15, US21) as shown in figure 4.33., with concentrations ranging from 0.0283 ppm (US7) to 0.7886 ppm (US2). The PMJR section yields a mean of 0.3994 ppm across all four quantified samples, the highest and most consistently detected of any locality, and substantially above the KRSS mean of 0.1664 ppm across 14 detections. The PMJRSS mean rubidium of 0.3994 ppm is 2.4 times higher than the KRSS mean of 0.1664 ppm. The internal PMJRSS pattern shows US2 (0.7886 ppm) and US4 (0.4917

ppm) as the most rubidium-enriched samples, with US3 (0.2611 ppm) and US1 (0.0564 ppm) lower. Within the Khushab road section, oxidized samples yield a mean rubidium of 0.1554 ppm compared to 0.1812 ppm for non-oxidized samples.

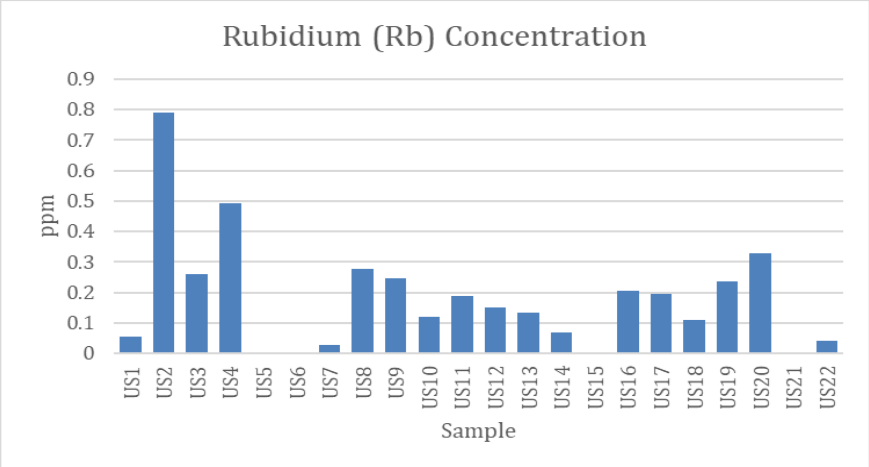

Figure 4.33. Rubidium concentration in samples

4.3.35 Ruthenium (Ru)

Ruthenium is a platinum group element detected in 12 of the 22 samples as shown in figure 4.34., with concentrations spanning from BDL in 10 samples to a maximum of 0.4214 ppm for US2. The PMJRS section shows detections in US1 (0.1667 ppm) and US2 (0.4214 ppm), yielding a mean of 0.2940 ppm, while US3 and US4 are BDL. The Khushab road section yields 10 detections with a mean of 0.0541 ppm, dominated by the US21 anomaly at 0.3736 ppm. The PMJRSS mean is approximately 5.4 times higher than the KRSS mean. Within the Khushab Road section, the oxidized samples yield detections in US7 (0.0183 ppm), US13 (0.0108 ppm), and US18 (0.0157 ppm) for a mean of 0.0149 ppm, while the non-oxidized group shows 7 detections (US5, US6, US14, US15, US16, US17, US21) for a mean of 0.0709 ppm.

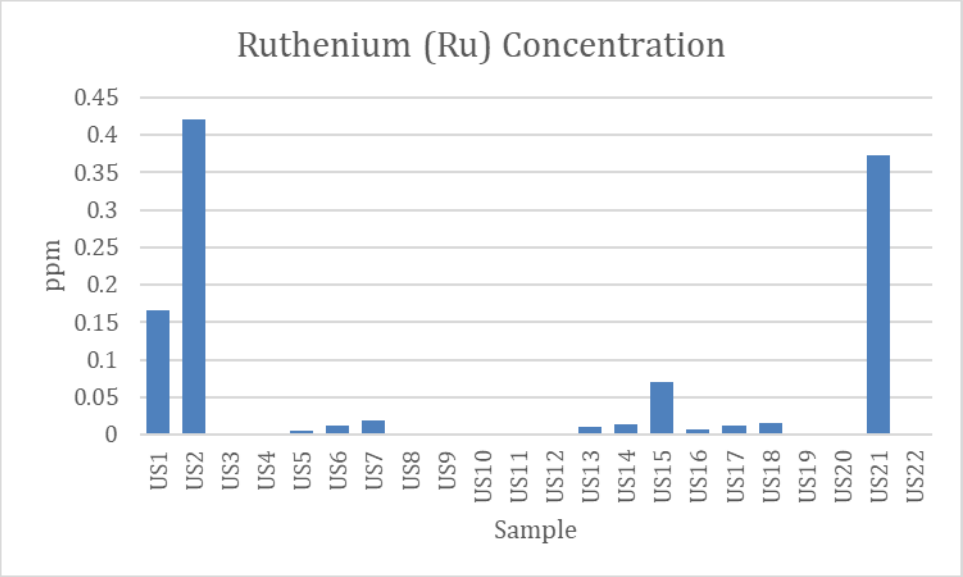

Figure 4.34. Ruthenium concentration in samples

4.3.36 Samarium (Sm)

Samarium is detected in 18 of the 22 samples as shown in figure 4.35., with concentrations ranging from BDL in US4, US9, US11, US19 to a maximum of 0.7671 ppm in US1. The PMJRS section yields a mean of 0.4243 ppm (from three detections), while KRSS averages 0.0353 ppm (across 15 detections). The PMJRSS mean of 0.4243 ppm is approximately 12 times higher than the KRSS mean of 0.0353 ppm. The internal variability within PMJRSS is again very large with US1 (0.7671 ppm) and US2 (0.4968 ppm) being dramatically higher than US3 (0.0090 ppm), while US4 is BDL. Within the Khushab road section, the oxidized samples yield a mean samarium concentration of 0.0145 ppm (6 detections), compared to 0.0491 ppm for the non-oxidized samples (9 detections) suggesting a 3.4-fold depletion in oxidized samples. The BDL readings in oxidized samples US11 and US19 and non-oxidized US9 contribute to the lower detection rates overall.

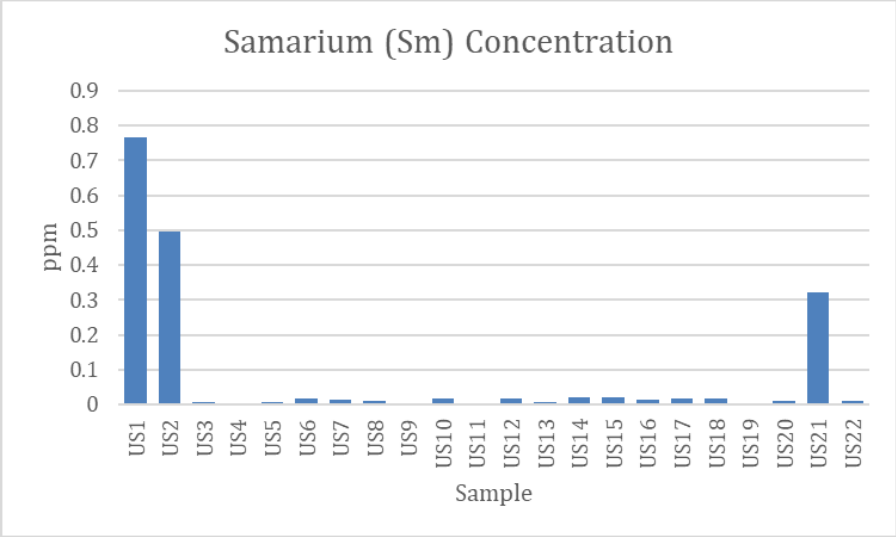

Figure 4.35. Samarium concentration in samples

4.3.37 Scandium (Sc)

Scandium is detected in 21 of 22 samples (BDL only in US11) as shown in figure 4.36., with concentrations ranging from 0.0010 ppm (US16) to 0.3479 ppm (US2). The PMJRSS yields a mean of 0.1475 ppm which substantially higher than the KRSS mean of 0.0166 ppm. Within the Khushab road section, the oxidized samples yield a mean scandium of 0.0035 ppm compared to 0.0257 ppm for non-oxidized samples.

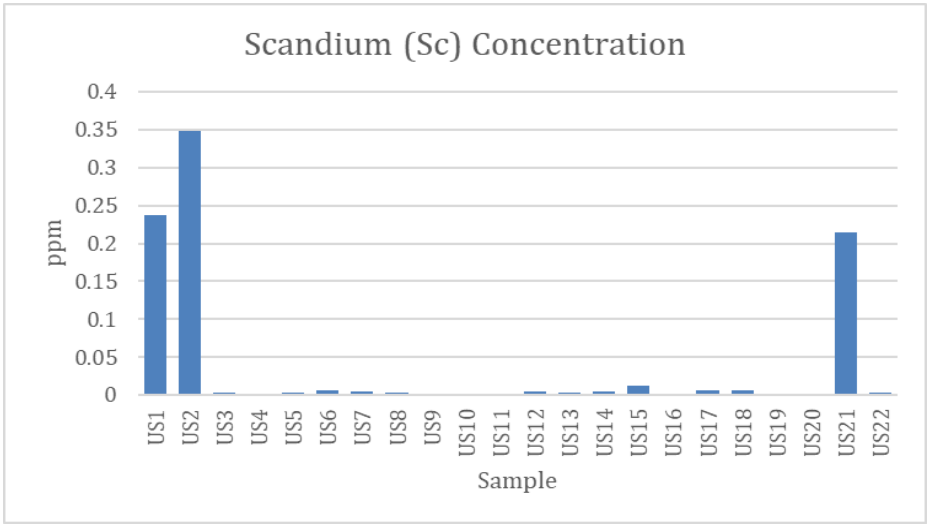

Figure 4.36. Scandium concentration in samples

4.3.38 Silicon (Si)

Silicon is detected in only 14 of the 22 samples as shown in figure 4.37., with BDL readings in 8 samples (US3, US4, US6, US10, US13, US14, US16, US19). Concentrations range from 0.0360 ppm (US5) to 3.4721 ppm (US21), with the PMJRS section showing moderate values in US1 (1.7075 ppm) and US2 (3.4721 ppm) while US3 and US4 are BDL. The PMJRS section yields a mean of 2.5898 ppm for detected samples. The Khushab road section shows 12 detections across both oxidized and non-oxidized samples with a mean of 0.5079 ppm. Within the Khushab road section, oxidized samples yield a mean silicon of 0.3947 ppm compared to 0.5888 ppm in non-oxidised samples. US21 shows high silicon concentration at 3.459 ppm.

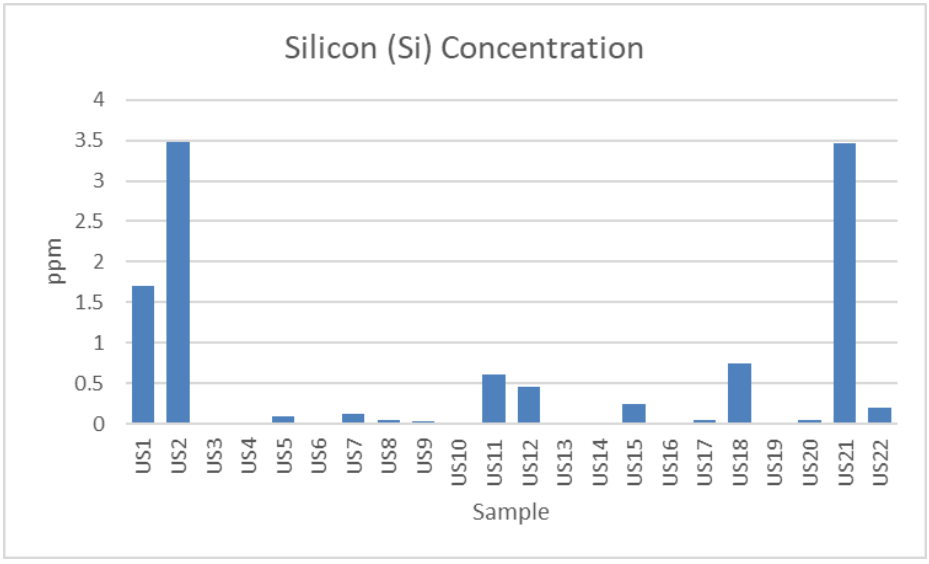

Figure 4.37. Silicon concentration in samples

4.3.39 Silver (Ag)

The element is detected in 19 of the 22 samples as shown in figure 4.38., with US1, US2, and US13 returning BDL. Concentrations across all detected samples fall in the tight range of 0.0023–0.0127 ppm, with the singular and spectacular exception

of US21, which yields a silver concentration of 1.2383 ppm. This US21 value is approximately 100–500 times higher than the background concentrations observed in all other samples and represents the most dramatic single-sample anomaly of any element in the dataset. The comparison for silver being that PMJRSS yields only two detections (US3 at 0.0130 ppm and US4 at 0.0040 ppm, with US1 and US2 BDL) for a mean of 0.0085 ppm, while the Khushab road section shows a mean of 0.0771 ppm. Excluding US21, the KRSS background mean would be approximately 0.0049 ppm which slightly lower than the PMJRSS mean. Within the Khushab road section, the comparison between oxidized and non-oxidized samples provides a clear pattern, oxidized samples yield a mean of 0.0054 ppm compared to 0.1273 ppm for non-oxidized samples.

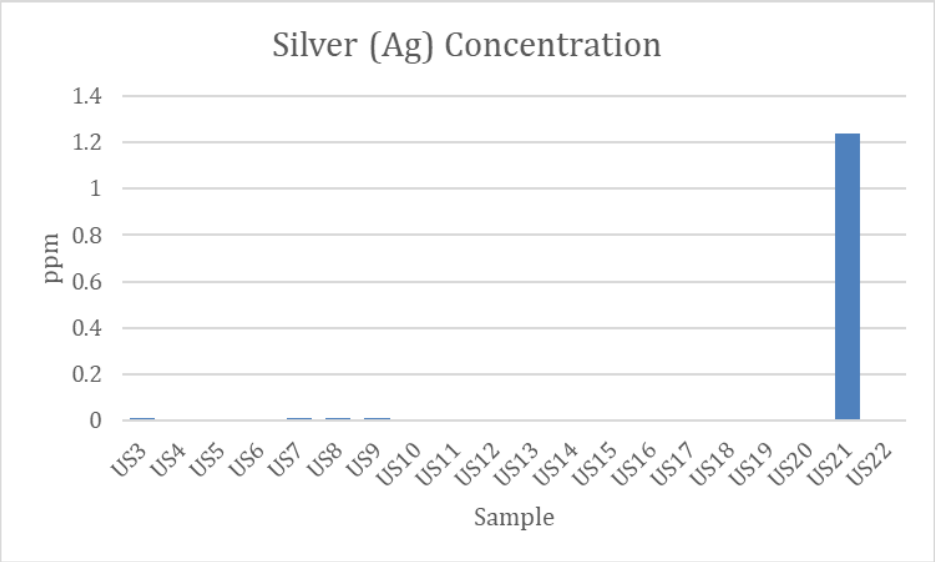

Figure 4.38. Silver concentration in samples

4.3.40 Tantalum (Ta)

Tantalum is detected in only 5 of the 22 samples as shown in figure 4.39., US2 (0.0111 ppm, US9 (0.0034 ppm), US11 (0.0084 ppm), US18 (0.0065 ppm), and US21 (0.0200 ppm). Tantalum shows extremely limited but interpretable data across the dataset. In the Khushab road section, the four detections yield a mean of 0.0096 ppm, broadly like the PMJRSS value. Within the KRSS redox comparison, the two

oxidized detections (US11 and US18) yield a mean of 0.0075 ppm, while the two non-oxidized detections (US9 and US21) yield 0.0117 ppm, a modest difference showing slightly higher tantalum in non-oxidised samples. The highest single value in the Kallar Kahar section belongs to US21 (0.0200 ppm).

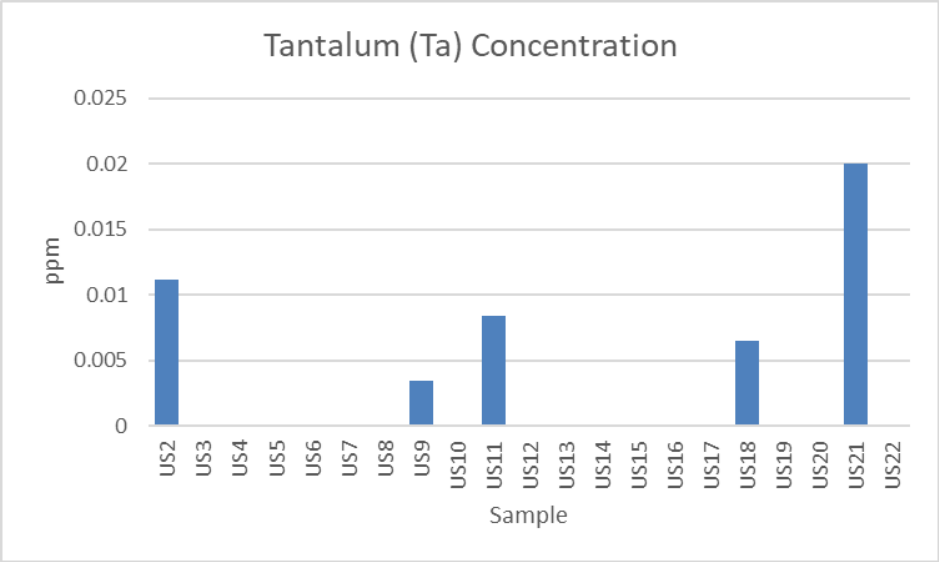

Figure 4.39. Tantalum concentration in samples

4.3.41 Tellurium (Te)

Tellurium is detected in 7 of the 22 samples as shown in figure 4.40., US1, US2, US3 and US10, US15, US18, US20, with concentrations ranging from 0.0083 ppm (US18) to 0.0765 ppm (US1). The PMJRS section exhibits a mean tellurium concentration of 0.0529 ppm compared to a mean of 0.0170 ppm for the four detections in the Khushab road section, a three-fold enrichment in PMJRSS. The consistent detection of tellurium across three of the four samples of PMJRSS points to a systematic enrichment of this element. Within the Khushab rad section, the distinction between oxidized and non-oxidized samples is subtle with detections in oxidized samples yielding a mean of 0.0158 ppm, while the detections in non-oxidized samples give 0.0182 ppm.

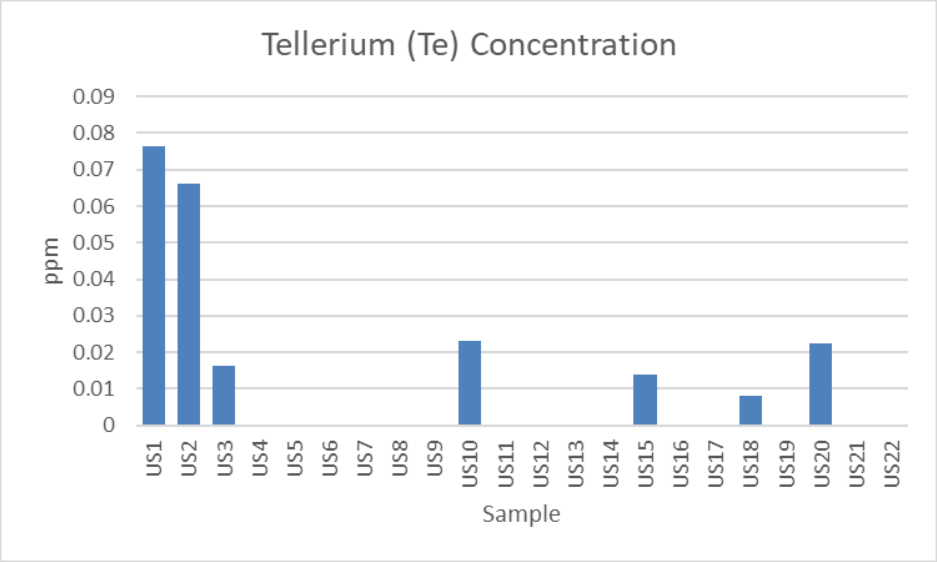

Figure 4.40. Tellurium concentration in samples

4.3.42 Terbium (Tb)

It is detected in 15 of the 22 samples as shown in figure 4.41., with concentrations ranging from BDL in six samples (US5, US11, US12, US16, US19, US20, US22) to a maximum of 0.0828 ppm (US1). The PMJRS section yields a mean of 0.0373 ppm across all four detections, substantially above the KRSS mean of 0.0114 ppm across 11 detections.

The PMJRSS mean terbium concentration of 0.0373 ppm is approximately 3.3 times higher than the KRSS mean of 0.0114 ppm. Within the Khushab road section, oxidized samples yield a mean terbium of 0.0056 ppm compared to 0.0163 ppm in non-oxidized samples.

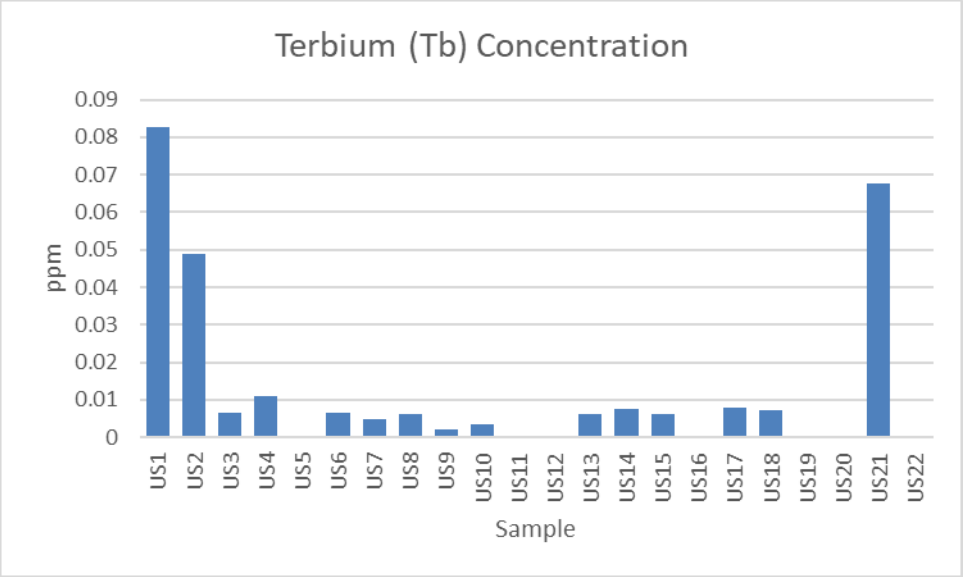

Figure 4.41. Terbium concentration in samples

4.3.43 Thulium (Tm)

Concentrations range from 0.0024 ppm (US5) to 0.0517 ppm (US1), with the PMJRSS mean of 0.0222 ppm substantially exceeding the KRSS mean of 0.0049 ppm. The PMJRSS section yields a mean thulium of 0.0222 ppm which is approximately 4.6 times higher than the KRSS mean of 0.0049 ppm. Within the Khushab road section, the contrast between oxidized (mean = 0.0043 ppm) and non-oxidized (mean = 0.0053 ppm) samples is the smallest of any critical mineral in this dataset as shown in figure 4.42.

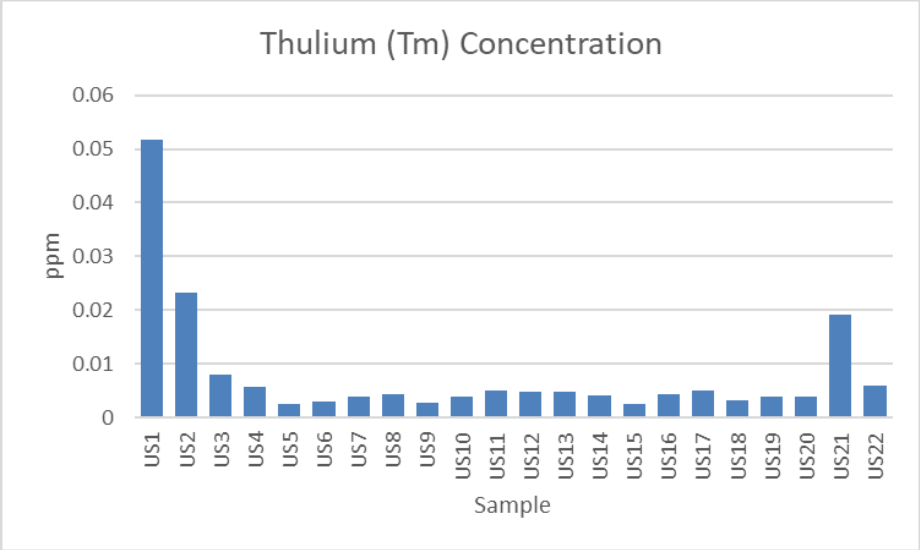

Figure 4.42. Thulium concentration in samples

4.3.44 Titanium (Ti)

Titanium is well detected throughout the dataset, with quantifiable values in 20 of the 22 samples, US10 and US12 registering BDL. Concentrations range from a minimum of 0.0021 ppm (US4) to a maximum of 3.1877 ppm (US21), with a clear concentration gradient between the two study areas. The elevated values in US1 (0.9813 ppm) and US2 (1.5790 ppm), and the particularly high value in US21 (3.1877 ppm), may reflect local concentrations of heavy mineral grains. The PMJRSS samples exhibit a mean titanium concentration of 0.6416 ppm versus 0.2798 ppm for KRSS, indicating roughly 2.3 times greater titanium enrichment.

Within the Khushab road section, the oxidized samples reveal a dramatically lower mean of just 0.0604 ppm compared to the non-oxidized samples mean of 0.4114 ppm. US21 stands out as by far the richest titanium sample in the Kallar Kahar non-oxidized group, suggesting a unique heavy mineral enrichment as shown in figure 4.43.

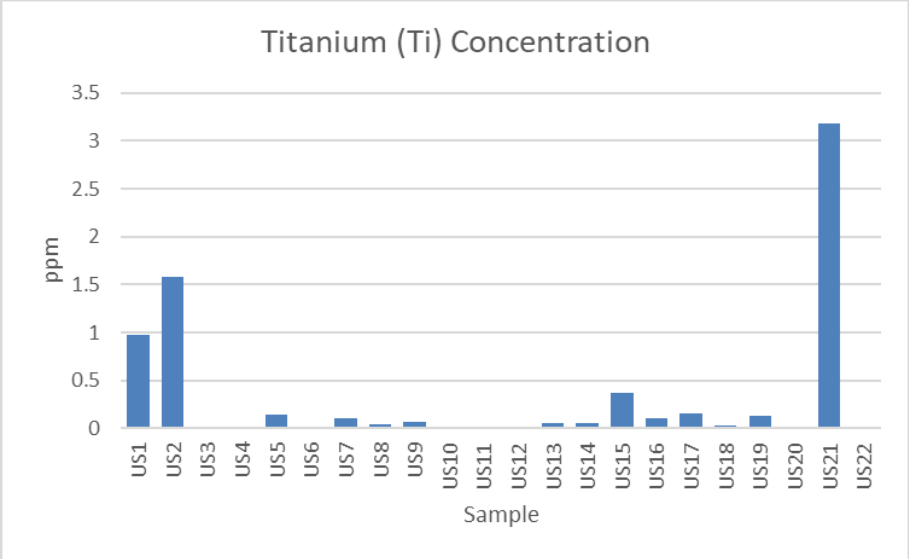

Figure 4.43. Titanium concentration in samples

4.3.45 Uranium (U)

Uranium is one of the most analytically remarkable economic elements in this dataset because, unlike every other element analyzed, it is detected in all 22 samples without a single BDL or ADL reading as shown in figure 4.44., making it the most consistent and evenly distributed economic mineral across the entire study sections. Concentrations range from 0.0644 ppm (US4) to 0.5811 ppm (US21, non-oxidized), with the PMJRSS mean of 0.2940 ppm and the KRSS mean of 0.2848 ppm being remarkably similar. The particularly elevated values in US1 (0.4697 ppm), US2 (0.5334 ppm), and US21 (0.5811 ppm) may reflect localized concentrations of organic matter or phosphatic material that serve as preferential uranium traps. The uniform distribution of uranium across all samples, however, indicates that low-level uranium is pervasively incorporated throughout the clay matrix of both localities. The comparison between PMJRSS (mean = 0.2940 ppm) and KRSS (mean = 0.2848 ppm) for uranium is the closest of any critical mineral in the dataset. Within the Khushab road section, the oxidized samples yield a mean uranium of 0.2409 ppm compared to 0.3200 ppm in non-oxidized samples.

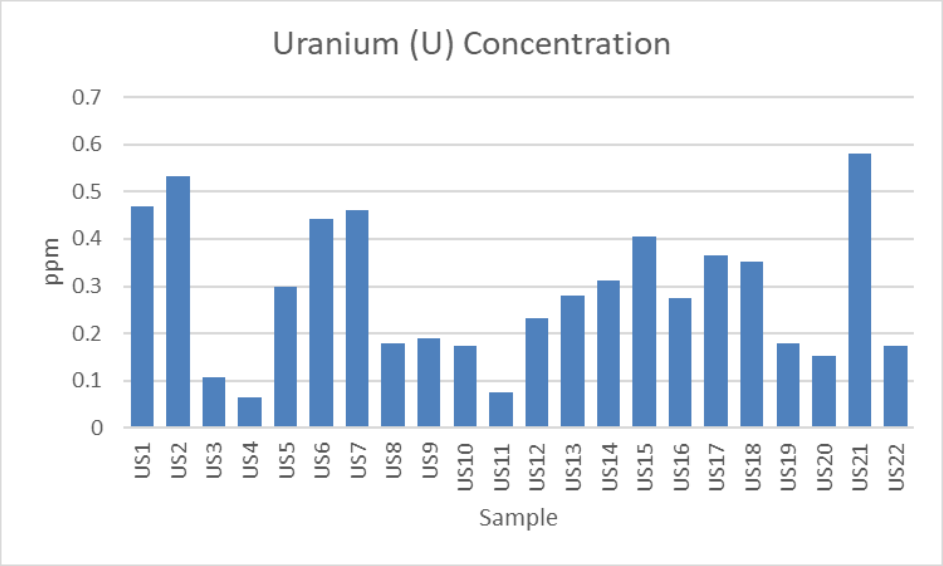

Figure 4.44. Uranium concentration in samples

4.3.46 Vanadium (V)

Vanadium emerges as the second most consistently detected critical mineral in this dataset, with quantifiable concentrations present in 21 out of 22 samples US21 registering ADL (Above Detection Limit) indicating an especially elevated concentration beyond the instrument's calibration range) as shown in figure 4.45. The concentrations span from 0.0677 ppm (US4) to 9.9536 ppm (US2), making vanadium one of the most variable elements in the dataset. The notably high values in the PMJRSS samples are particularly in the US1 (4.7710 ppm) and US2 (9.9536 ppm) samples. In the Khushab road section, vanadium is generally lower but still consistently detectable, pointing to a background vanadium enrichment in the regional clay stratigraphy. The PMJRSS samples yield a mean vanadium concentration of 3.7457 ppm which is more than eight times higher than the KRSS mean of 0.4343 ppm. Within the Khushab road section, the comparison between oxidized and non-oxidized samples reveals a near-identical mean of 0.4348 ppm for oxidized and 0.4345 ppm for non-oxidized samples. The ADL reading in US21 is noteworthy as an outlier that departs significantly from this pattern.

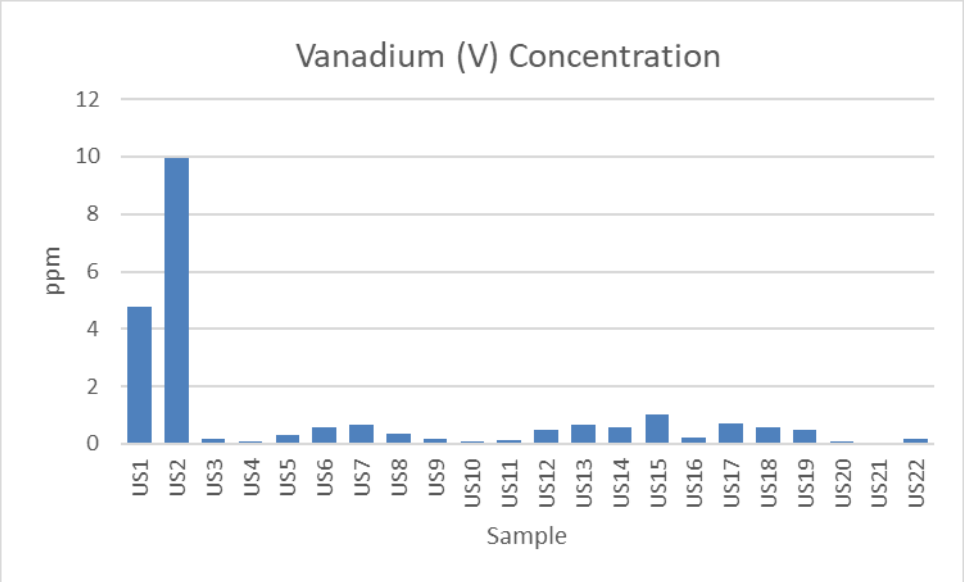

Figure 4.45. Vanadium concentration in samples

4.3.47 Ytterbium (Yb)

Ytterbium is a heavy rare earth element detected in 19 of the 22 samples (BDL only in US9, US20, US22) as shown in figure 4.46., with concentrations ranging from 0.0003 ppm (US10, US16) to 0.0503 ppm (US1). The PMJRSS mean of 0.0219 ppm significantly exceeds the KRSS mean of 0.0048 ppm being 6 times. Within the Khushab road section, the oxidized samples return a mean of just 0.0010 ppm, compared to 0.0091 ppm for the non-oxidized samples.

The fact that all oxidized samples yield very low but detectable ytterbium values (0.0003–0.0018 ppm), while the non-oxidized mean is pulled up by values such as US21 (0.0538 ppm), US15 (0.0025 ppm), and US17 (0.0019 ppm), confirms that oxidative weathering has been highly effective at stripping ytterbium from the oxidized horizons.

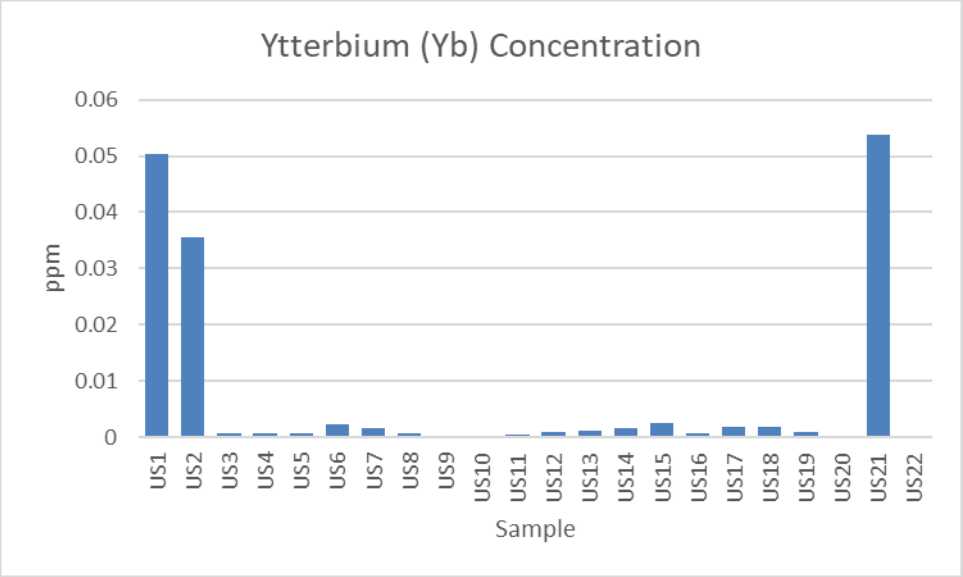

Figure 4.46. Ytterbium concentration in samples

4.3.48 Yttrium (Y)

It is detected in all 22 samples in this dataset as shown in figure 4.47. Concentrations span from a minimum of 0.0009 ppm (US4) to a maximum of 1.3024 ppm (US1), with the PMJRSS mean reaching 0.4409 ppm substantially exceeding the KRSS mean of 0.0474 ppm. Within KRSS, yttrium ranges from 0.0029 ppm US4 to 0.6766 ppm (US21).

The PMJRSS section shows marked intra-section heterogeneity (US1 at 1.3024 ppm, US2 at 0.4566 ppm, but US3 and US4 at only 0.0040 and 0.0009 ppm respectively). Within the KRSS section, the redox comparison reveals a very striking contrast, oxidized samples average just 0.0082 ppm (all detected) compared to 0.0787 ppm for non-oxidized.

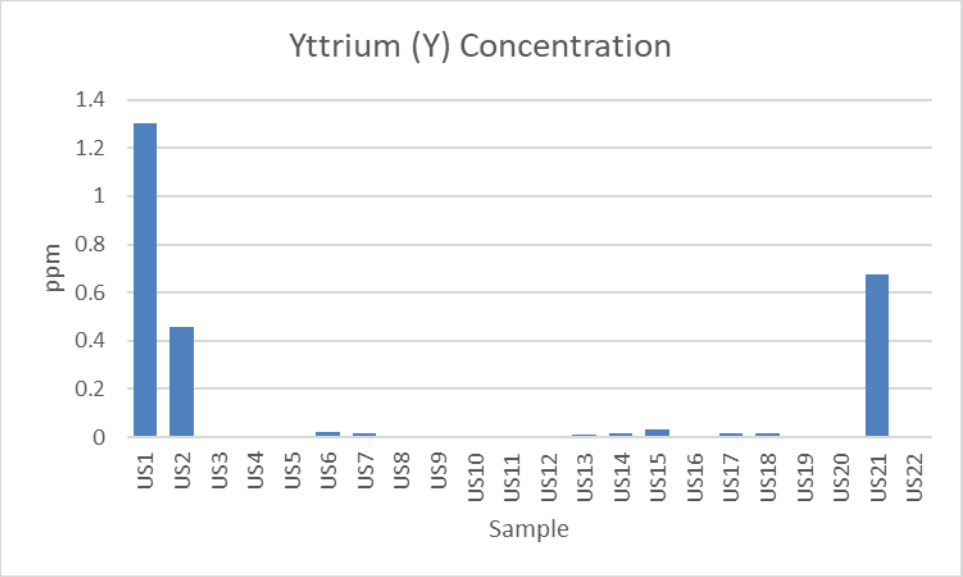

Figure 4.47. Yttrium concentration in samples

4.3.49 Zinc (Zn)

Zinc is detected in all 22 samples and displaying the largest single-sample anomaly of any base metal as shown in figure 4.48., US8 returning a remarkable 8.1598 ppm. The overall concentration range spans from 0.0288 ppm (US4) to 8.1598 ppm (US8) Khushab roadside section, oxidized samples yield a mean of 1.127 ppm compared to just 0.384 ppm in non-oxidized samples.

This geochemically anomalous pattern is dominated by the extraordinary US8 value of 8.1598 ppm, which alone accounts for most of the oxidized group's mean.

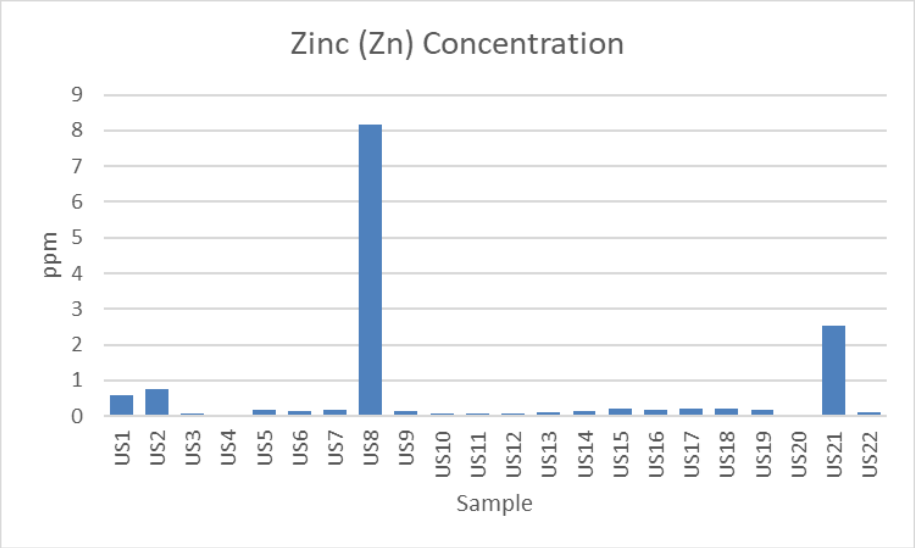

Figure 4.48. Zinc concentration in samples

4.3.50 Zirconium (Zr)

Zirconium is detected in 12 of the 22 samples as shown in figure 4.49., with concentrations ranging from 0.0015 ppm (US4) to 0.1462 ppm (US1). The highest concentrations in the dataset are concentrated in PMJRSS (US1 at 0.1310 ppm and US2 at 0.1462 ppm), with most KRSS samples showing much lower values. The elevated Zr in US21 (0.1430 ppm) within the KRSS section is anomalous relative to surrounding samples and may reflect a discrete horizon with locally elevated heavy mineral content.

The contrast between the two localities is the most dramatic for zirconium among all critical minerals, the PMJRSS mean of 0.0929 ppm is more than five times higher than the KRSS mean of 0.0178 ppm. Within the Khushab road section, the oxidized samples exhibit a mean of only 0.0028 ppm compared to 0.0328 ppm for non-oxidized samples, approximately an 11-fold difference that is one of the largest redox-related contrasts in the entire dataset for this element.

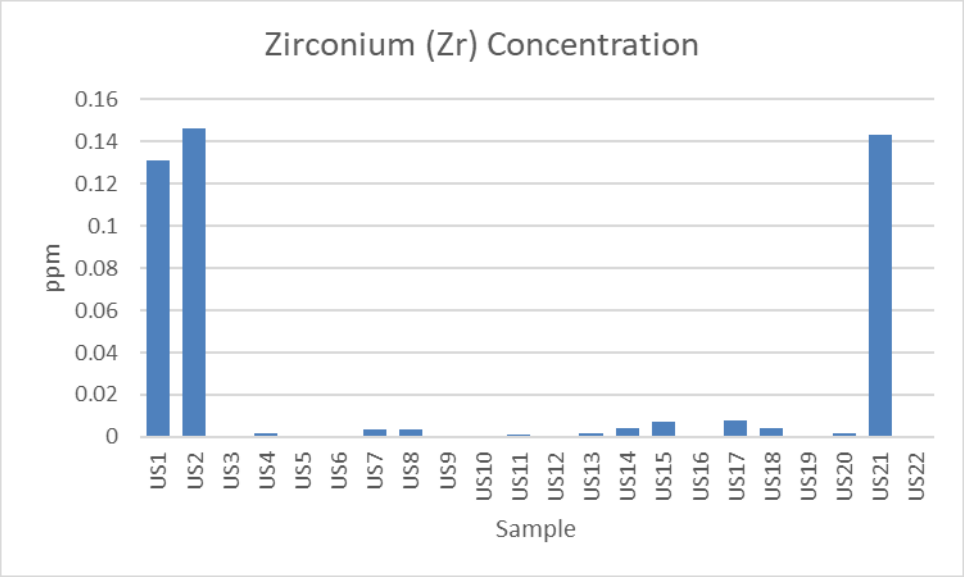

Figure 4.49. Zirconium concentration in samples

4.3.51 Uses of critical minerals in the industry

Critical minerals collectively make the material foundation of modern technological and industrial civilization. Their applications span clean energy, advanced manufacturing, defense, electronics, and medicine. The U.S. Geological Survey (USGS, 2025) defines critical minerals as those essential to the economy and national security whose supply chains are vulnerable to great disruption, a designation that reflects their functionality across sectors where there are no other viable substitutes. The International Energy Agency (IEA, 2021) reported that the clean energy transition is highly mineral intensive, with lithium, cobalt, nickel, manganese, and graphite being irreplaceable in lithium-ion batteries for electric vehicles and large grid scale energy storage. Neodymium, dysprosium, and terbium are essential components of the permanent magnets powering wind turbine generators and electric vehicle traction motors. Gallium nitride and gallium arsenide semiconductors enable high frequency transistors, 5G communications infrastructure, and high-efficiency solar cells that define the digital and low-carbon economy. Titanium, chromium, vanadium, and niobium are irreplaceable alloying materials in the high strength steels, and aerospace structural materials that forms the global infrastructure, transportation, and defense manufacturing (Graedel et al., 2015). Beryllium's unique nature of being

low in density, high in stiffness, and near-transparency to X-rays makes it irreplaceable in nuclear systems, aerospace instruments, and X-ray equipment. Hafnium oxide has become the standard gate dielectric in advanced semiconductor transistors while zirconium alloys serve as the primary nuclear reactor fuel rod protection material, and tantalum capacitors are found in all of the modern electronic devices (USGS, 2025). The World Bank (2020) further projected that production of critical minerals would need to increase by up to 500% by 2050 to meet clean energy demand, underscoring that the strategic importance of these materials extends across every dimension of sustainable industrial development thus making their secure and sustainable supply a resource challenge of the modern age (Graedel et al., 2015; IEA, 2021).

4.4 Other minerals

Minerals other than the critical minerals, which were identified in the datasheet set that have prominent to negligible concentrations values are as follows:

4.4.1 Cadmium (Cd)

Cadmium is detected in 18 of the 22 samples as shown in figure 4.50., with BDL readings limited to US4 and US8, US11, US22. Its concentrations are among the lowest of any detected element in the dataset, ranging from 0.0005 ppm (US19) to 0.0201 ppm (US21). The PMJRS section yields three detections for cadmium (US1 at 0.0057 ppm, US2 at 0.0082 ppm, US3 at 0.0012 ppm; US4 BDL) for a mean of 0.0051 ppm that is slightly higher than the KRSS mean of 0.0037 ppm across 15 detections. Within the Khushab road section, the oxidized samples yield a mean of 0.0022 ppm compared to 0.0047 ppm in non-oxidized samples.

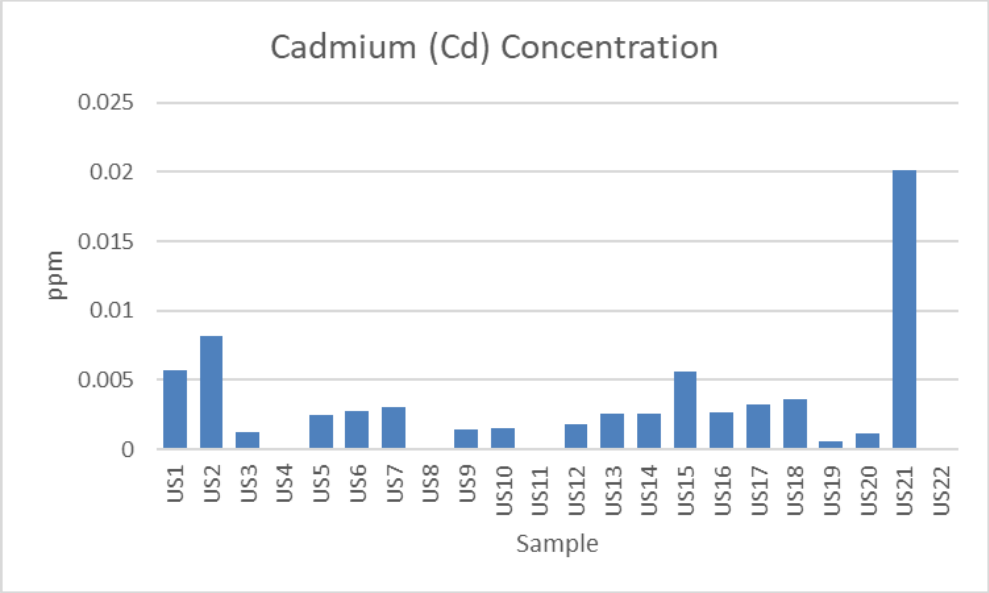

Figure 4.50. Cadmium concentration in samples

4.4.2 Calcium (Ca)

Calcium is one of the most analytically constrained elements in this dataset, due to ADL readings dominate overwhelmingly, with 21 of the 22 samples exceeding the instrument's upper detection limit and only US4 yielding a quantifiable concentration of 5.2191 ppm as shown in figure 4.51. This near-universal ADL status indicates that calcium concentrations throughout two sections are extremely elevated and broadly comparable in magnitude, far exceeding the calibration range of the ICP-MS instrument as for this multi-element survey.

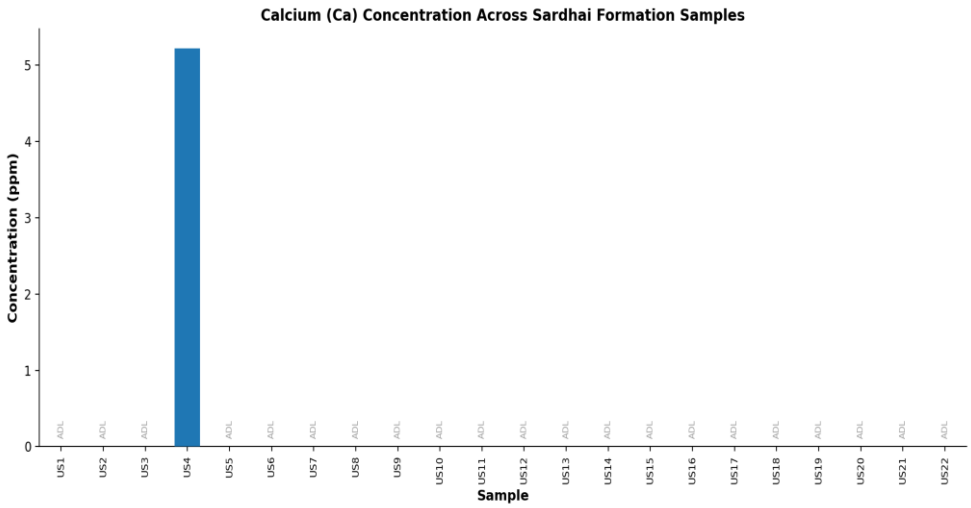

Figure 4.51. Calcium concentration in samples

4.4.3 Gold (Au)

Gold is detected in 6 of the 22 samples as shown in figure 4.52., with all four PMJRSS samples returning BDL and the KRSS section yielding detections in US5 (0.0068 ppm), US7 (0.0102 ppm), US10 (0.0070 ppm), US15 (0.0132 ppm), US20 (0.0102 ppm), and the multi-element anomalous US21 (0.1333 ppm). Within the Khushab road section, the oxidized samples yield detections in only two samples (US7 at 0.0102 ppm and US10 at 0.0070 ppm) for an oxidized mean of 0.0086 ppm, compared to four non-oxidized detections (US5, US15, US20, US21) for a non-oxidized mean of 0.0409 ppm. The higher non-oxidized gold means is dominated by US21's anomalous 0.1333 ppm value; excluding US21, the non-oxidized background gold (US5, US15, US20 averaging 0.0100 ppm) is broadly comparable to the oxidized values.

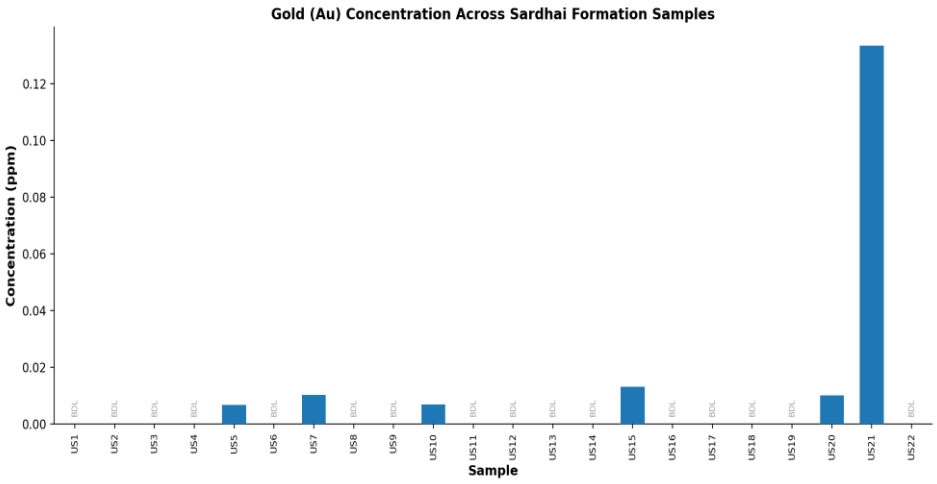

Figure 4.52. Gold concentration in samples

4.4.4 Iron (Fe)

Iron registers ADL in no fewer than 14 of the 22 samples as shown in figure 4.53., indicating that its concentrations in most samples exceed the instrument's calibration range. The eight samples yielding quantifiable values range from 2.3 ppm (US4) to 10.669 ppm (US8), with these representing a minimum estimate of the true iron concentration across the section. In PMJRSS, the two quantified samples (US3 at 7.110 ppm and US4 at 2.300 ppm) yield a mean of 4.705 ppm, while US1 and US2 are ADL. In KRSS, 7 quantified samples yield a mean of 6.290 ppm, with the highest single value being US8 at 10.669 ppm and US16 at 9.668 ppm. The consistent ADL readings in the majority of KRSS samples reinforce the interpretation that iron concentrations throughout the section are substantially elevated, likely above the 10–20 ppm range. The most geochemically revealing comparison in this dataset is between the oxidized and non-oxidized KRSS samples, the quantified oxidized samples a mean of 6.924 ppm, while the four quantified non-oxidized samples (US9 at 5.410 ppm, US10 at 5.145 ppm, US20 at 4.756 ppm, US22 at 3.424 ppm) average 5.815 ppm. The apparent higher iron in quantified oxidized samples is consistent with the well-known process of iron oxidation and immobilization. The ADL readings in multiple oxidized samples further suggest that the highest iron concentrations in the entire section are associated with the oxidized horizons.

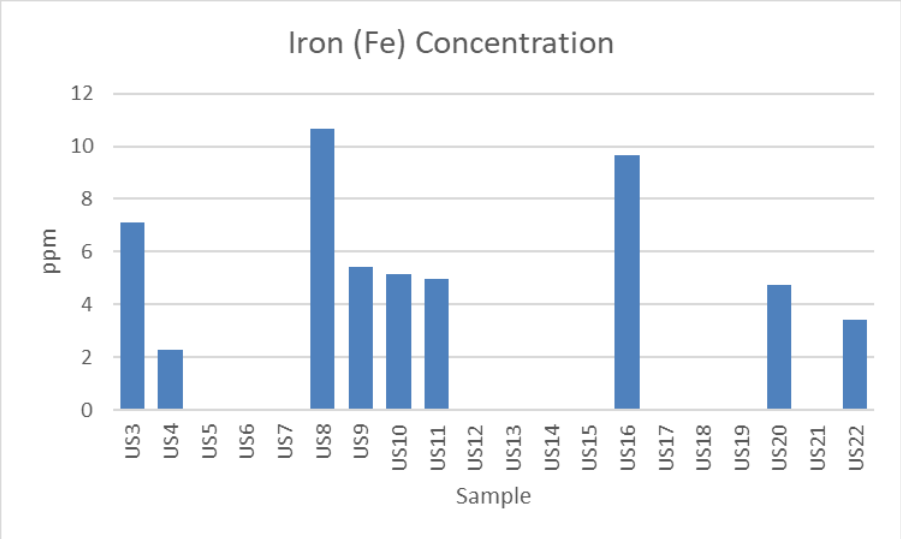

Figure 4.53. Iron concentration in samples

4.4.5 Mercury (Hg)

Mercury is entirely absent from all 22 samples in this dataset every sample return BDL without exception.

4.4.6 Sodium (Na)

Sodium presents a geochemically informative distribution in this dataset, with 12 of the 22 samples returning ADL readings and 10 samples yielding quantifiable concentrations ranging from 4.1304 ppm (US20) to 10.6351 ppm (US13) as shown in figure 4.54. The ADL readings in all four PMJRSS samples confirm that sodium concentrations in the section are extremely elevated, likely substantially higher than the maximum quantified KRSS value of 10.635 ppm. Within the Khushab road section, the 10 quantified samples yield a mean sodium of 7.687 ppm.

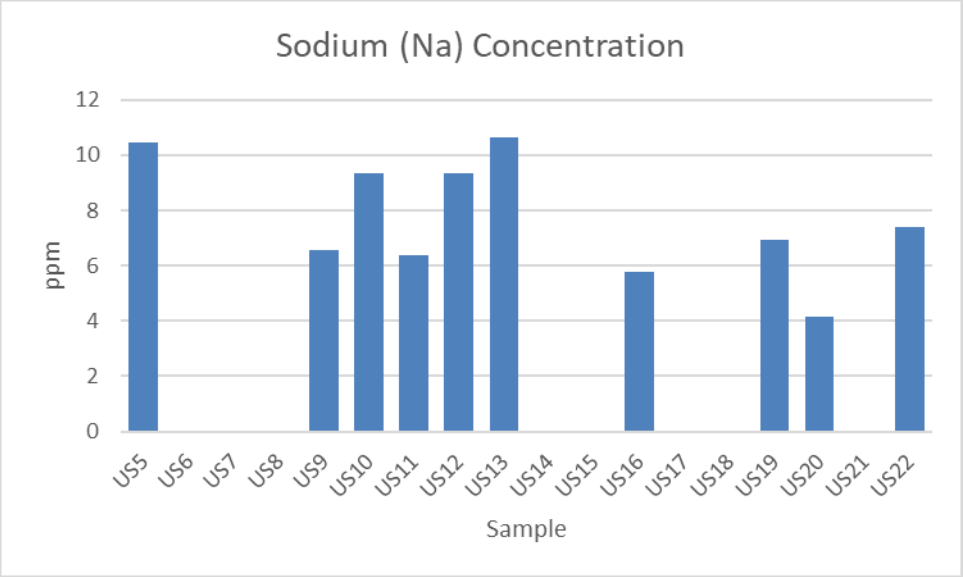

Figure 4.54. Sodium concentration in samples

4.4.7 Strontium (Sr)

Strontium is detected in 20 of the 22 samples as shown in figure 4.55., with US1 returning ADL and US21 also ADL. The remaining 20 quantifiable or BDL values range from 0.0007 ppm US4 to 10.8748 ppm US2. US2's value of 10.8748 ppm is the highest single quantified mineral value in the dataset (excluding ADL-capped elements), pointing to a strontium-rich phase. The PMJRS section exhibits a mean strontium of 3.6382 ppm (across US2 at 10.875 ppm, US3 at 0.039 ppm, and US4 at 0.0007 ppm; US1 ADL). The KRSS yields a more moderate mean of 0.7988 ppm across 17 detections, ranging from 0.1452 to 3.1025 ppm. Within the Khushab road section, oxidized samples yield a mean of 0.5781 ppm compared to 0.9951 ppm in non-oxidized samples.

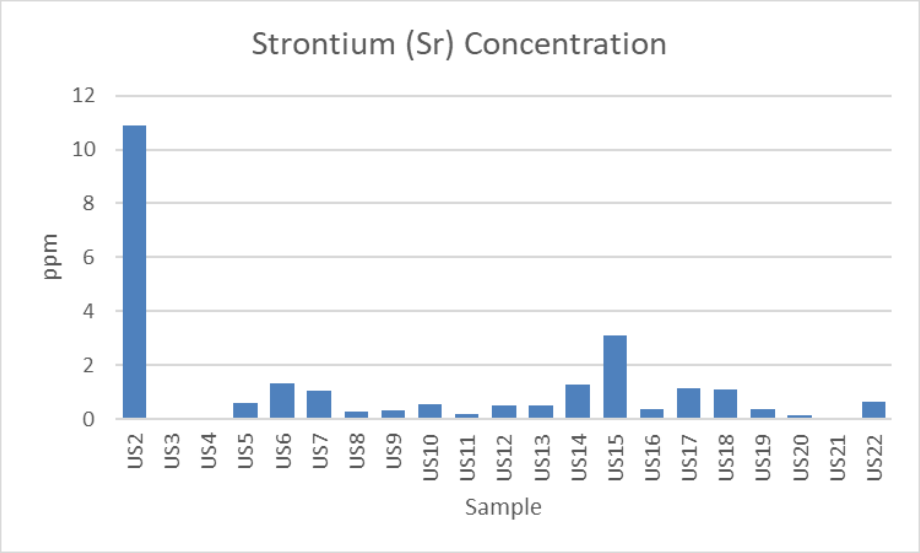

Figure 4.55. Strontium concentration in samples

4.4.8 Sulphur (S)

Sulphur is one of the most analytically constrained elements in this dataset, with 18 of the 22 samples returning ADL readings and only four samples yielding quantifiable concentrations: US1 (6.5975 ppm), US3 (6.8783 ppm), US11 (9619 ppm), and US20 (10.4283 ppm) as shown in figure 4.56. The uniform ADL dominance across the remaining 18 samples indicates that sulphur concentrations throughout both sections are extremely elevated, broadly uniformly above the instrument's upper calibration limit.

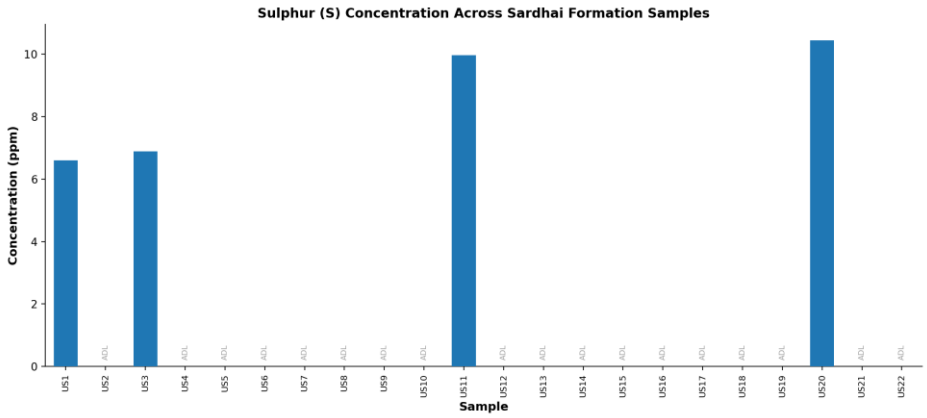

Figure 4.56. Sulphur concentration in samples

4.4.9 Thallium (Tl)

Thallium is detected in only 2 of the 22 samples, US13 (0272 ppm) and US18 (0155 ppm) with all other 20 samples returning BDL as shown in figure 4.57. The restriction of thallium detections exclusively to two oxidized samples, and their complete absence from both the PMJRSS section and the non-oxidized samples, creates a uniquely informative geochemical pattern.

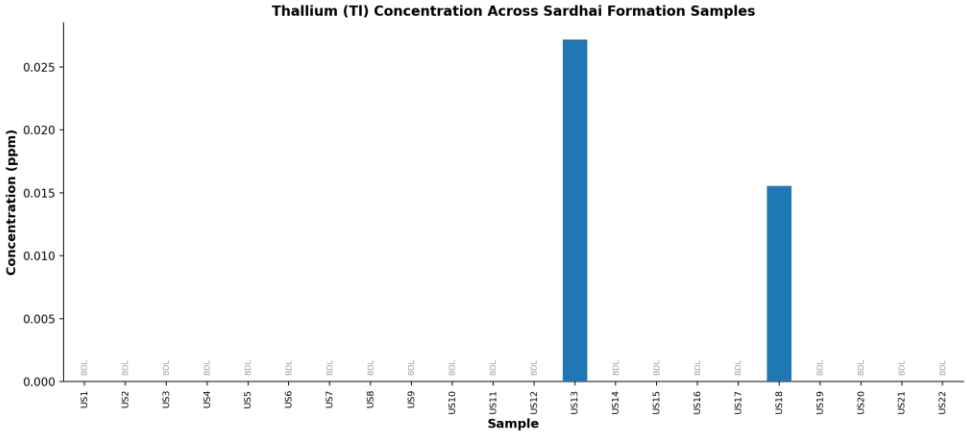

Figure 4.57. Thallium concentration in samples

4.4.10 Thorium (Th)

Thorium is detected in all 22 samples without exception in this study as shown in figure 4.58. Concentrations range from a minimum of 0.0085 ppm (US22) to a maximum of 0.8828 ppm (US2), with the PMJRSS mean of 0.3840 ppm substantially exceeding the KRSS mean of 0.0587 ppm. Within the Khushab road section, the oxidized samples yield a mean thorium of 0.0257 ppm compared to 0.0850 ppm in non-oxidized samples.

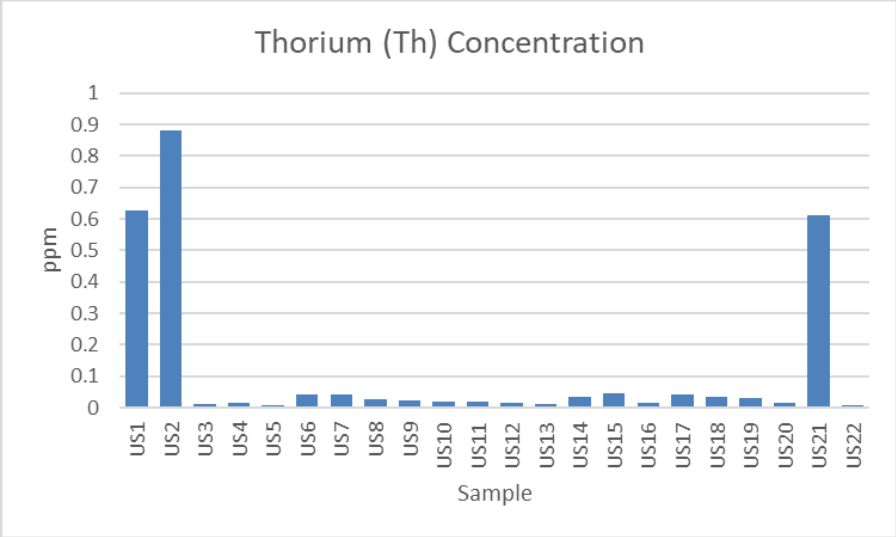

Figure 4.58. Thorium concentration in samples

4.4.11 Uses in the industry

Gold, cadmium, iron, thorium, calcium, mercury, sodium, sulphur, strontium, and thallium collectively represent a group of minerals that, while absent from the USGS 2025 Critical Minerals List, nonetheless fulfil highly significant and in several cases. They have importance in agricultural, chemical, and technological sectors. Iron is the most consumed metal in human history and is the foundational material of modern civilization, processed into steel for construction, transportation, pipelines, and machinery, with the global steel production reaching 1,904 million tonnes in

2023 (World Steel Association, 2024). Calcium carbonate minerals makes cement and lime production for the entire global construction industry, gypsum provides the raw material for plasterboard and soil amendment, and sodium, as soda ash and salt is the basis of the glass, detergent, chemical, and food production industries (Harben, 2002). Sulphur is converted into sulphuric acid and is the world's highest-volume industrial chemical essential to fertilizer manufacturing, metal leaching, petroleum refining, and battery acid production, while strontium carbonate is the primary feedstock for strontium ferrite which is used by permanent magnets, helping make loudspeakers and small motors. Strontium aluminate phosphors are long-persistence luminescent materials used globally in safety signage and emergency lighting systems (USGS, 2022). Cadmium telluride thin film photovoltaic technology, in which cadmium is an essential semiconductor component represents one of the lower cost solar technologies. Nickel cadmium batteries remain the preferred choice for aircraft emergency systems and telecommunications backup power due to their reliability at extreme temperatures. Thorium oxide serves as a high-performance refractory ceramic while thoriated tungsten electrodes are standard in tungsten inert gas welding applications due to their superior stability (USGS, 2022; Harben, 2002). Mercury, despite its progressive global phase-out under the Minamata Convention, retains critical applications in artisanal and small-scale gold mining, scientific instrumentation, and high intensity discharge lamps. Thallium activated scintillator crystals, particularly NaI(Tl) and CsI(Tl), remain the most widely used radiation detection materials in nuclear medicine gamma cameras, SPECT scanners, and security screening systems worldwide. This collectively demonstrates that minerals absent from formal criticality lists can nonetheless be significant across different industries (Nriagu, 1998; USGS, 2022).

CHAPTER 5
DISCUSSION

5.1 Discussion

The geochemical dataset presented here derives from 22 clay specimens of the Sardhai Formation (Nilawahan Group, Early Permian), collected across two outcrop localities and characterized using inductively coupled plasma mass spectrometry (ICP-MS). Because the formation is lithologically uniform and dominated almost entirely by clay, the study setting offers an unusually well constrained geochemical framework; any variability observed among samples US1–US22 between the two sites can reasonably be attributed to secondary controls i.e., post depositional alteration, differential surface weathering, and structural position within the fold and thrust belt, rather than to inherent differences in the original depositional material. The measured elemental concentrations across the suite remain consistently low in ppm, and the dataset is best regarded as reconnaissance level. These results should therefore not be interpreted as evidence of economic mineralization; rather, they constitute an initial geochemical baseline whose significance can only be properly assessed through further sampling, validation, and more detailed follow up investigations.

Cross-referencing the analytical results with the U.S. Geological Survey's 2025 List of Critical Minerals, which designates 60 minerals as essential to the U.S. economy and national security, including lithium, vanadium, manganese, niobium, nickel, chromium, beryllium, gallium, zirconium, hafnium, cobalt, uranium, copper, silver, lead, zinc, all rare earth elements, aluminium, magnesium, phosphate, silicon, rubidium, arsenic, boron, and iridium, the present dataset demonstrates that the Sardhai Formation clays serve as a geochemically heterogeneous host for a broad suite of critical minerals, whose distribution is systematically controlled by the interplay of redox conditions, structural fluid pathways, and diagenetic overprinting. This finding is broadly consistent with the proposition of Hatch and Leventhal (1992)

that fine grained sedimentary rocks function as geochemical catchers capable of concentrating critical minerals over geological time through adsorption onto particle surfaces and elemental substitution within crystal lattices, and the present study extends that framework by demonstrating that within a single sedimentary clay formation of Early Permian age, the degree of localized critical mineral enrichment can vary by factors of nearly twenty fold for beryllium and over twenty seven fold for lanthanum between sample positions making the point that lithological homogeneity at the formation scale does not guarantee geochemical homogeneity at the sample scale.

Lithium ranks among the most strategically significant critical minerals owing to its central role in lithium-ion battery technology for electric vehicles and grid-scale energy storage. It was detected in all 22 samples, although concentrations are low throughout, spanning from 0.031 ppm in US4 to a maximum of 1.843 ppm in US21. Even at these low levels, the universal presence of lithium across the suite supports the proposition of Hatch and Leventhal (1992) that fine grained aluminosilicates act as repositories for critical trace elements through lattice incorporation within clay minerals and surface adsorption. Notably, the average lithium content of samples US1–US4 (0.498 ppm) is roughly 2.35 times higher than that of US5–US22 (0.212 ppm); since both groups represent the same Sardhai Formation clay, this difference cannot be explained by any original variation in depositional lithium content. This pattern is reinforced by a 3.06-fold depletion of lithium in the oxidized sub-group (US7, US8, US10, US11, US13, US18, US19; mean 0.099 ppm) relative to the non-oxidized samples (US1–US6, US9, US12, US14–US17, US20–US22; mean 0.302 ppm), a contrast that, despite the overall low absolute concentrations involved, points to a clear and systematic process; oxidative weathering has preferentially stripped lithium from the oxidized horizons, while the non-oxidized samples retain a more faithful, if still modest, record of the formation's original lithium content. Benson et al., (2023) showed that lithium incorporated into illite clays during diagenesis can, under the right conditions, constitute an economically significant resource; although the depositional setting of the Sardhai Formation differs substantially from that caldera hosted system, the underlying mechanism being clay hosted lithium enrichment modified by diagenetic and weathering processes acting on fine grained

sedimentary sequences, appears broadly analogous. On this basis, the non oxidized sample positions within the formation can be regarded as preserving the lithium bearing clay fabric in a state more comparable to a primary signal than the surficially weathered, oxidized horizons.

Vanadium is also a critical mineral that shows the most dramatic inter sample contrast in the dataset where US2 yields 9.954 ppm and US1 yields 4.771 ppm, while most US5 through US22 samples fall below 1 ppm, with the mean of US1–US4 (3.746 ppm) being 8.6-fold higher than the US5–US22 mean of (0.434 ppm). Leventhal (1991) attributed anomalous vanadium concentrations in Devonian-Mississippian black shales of the Appalachian Basin to anoxic depositional conditions and organic complexation, a mechanism entirely consistent with the enrichment of vanadium in fine grained sedimentary sequences, where organic matter content is elevated, and the present V-Ni-Cr co-enrichment at US1 and US2, with nickel yielding 0.256 ppm and 0.379 ppm, and chromium 0.266 ppm and 0.746 ppm respectively, points towards a locally preserved organic-rich or anoxic sedimentary microenvironment at those specific horizons of the Sardhai Formation clays, which is entirely consistent with the sedimentary enrichment mechanisms as described by Leventhal (1991). The concentrations provided in the dataset are below the economic threshold.

The complete absence of chromium across all seven oxidized samples (US7, US8, US10, US11, US13, US18, US19), where it registers BDL throughout, reinforces the redox sensitive nature of transition metal distribution within the formation and parallels the sharp geochemical differences at redox boundaries documented by Leventhal (1991) in fine grained sedimentary sequences. Beryllium is detected in all 22 samples and is non-economical, with US1 yielding 0.480 ppm and the US1–US4 mean of 0.217 ppm being approximately 20 times higher than the US5–US22 mean of 0.011 ppm, thus being the largest localized intra-formation enrichment ratio of any individual critical mineral in the dataset, also confirms that post depositional geochemical processes operating within the same clay formation are capable of generating extreme elemental differences over short lateral distances. Manganese, niobium, gallium, titanium, and zirconium similarly display systematic

enrichment in non-oxidized over oxidized samples within the same Sardhai Formation clay, with niobium showing a 10.61-fold depletion in oxidized samples relative to non-oxidized equivalents. zirconium showing an 11.74-fold depletion, pointing to the deep control that near surface oxidative weathering have on fine grained sedimentary sequences and the effects which it exerts on their critical mineral concentration.

The most geochemically interesting evidence of localized intra-formational enrichment processes taking place in the Sardhai Formation clays is the rare earth elements, all of which are considered critical minerals and form one of the most strategically important subgroups in the USGS list, although are found to be low in ppm values in the present dataset. Lanthanum reaches 8.011 ppm in US1, with US1–US4 yielding a mean of 2.997 ppm compared to just 0.110 ppm across US5–US22 which is a 27-fold intra-formational contrast. Cerium registers ADL in US1 and 10.568 ppm in US2, and neodymium reaches 4.901 ppm in US1, all co-enriched alongside thorium with the US1–US4 group averaging 0.384 ppm compared to 0.059 ppm for US5–US22, representing a 6.5-fold difference within the same sedimentary clay unit. This pattern of thorium co-enrichment is consistent with the concentration of rare earth elements in secondary phosphate and organic-bearing phases within fine-grained sedimentary sequences, directly supporting the framework described by Chi and Tian (2011), who documented that REEs concentrate in phosphatic shales and organic-rich mudstones where redox conditions and clay mineralogy influence elemental partitioning, processes entirely applicable to a clay-dominated sedimentary formation such as the Sardhai Formation. The systematic depletion of all rare earth critical minerals in the oxidized samples relative to non-oxidized equivalents, with lanthanum showing 5.86-fold, neodymium 9.24-fold, yttrium 9.56-fold, and scandium 7.33-fold depletions, along with multiple others registering as BDL across the oxidized sample group demonstrates the light element stripping mechanism described by Chi and Tian (2011). The thorough detection of gadolinium across all 22 samples (0.008 to 1.810 ppm), thulium in all 22 samples (0.002 to 0.052 ppm), and europium in 20 of 22 samples reflects the diffuse clay mineral surface adsorption as described by Chi and Tian (2011) for ionic adsorption clay systems, thus being inherent to the Sardhai Formation clay.

The near perfect equivalence of uranium and phosphorus between the US1–US4 group (U mean 0.294 ppm, P mean 5.496 ppm) and the US5–US22 group (U mean 0.285 ppm, P mean 5.579 ppm), which are deemed to be below economic threshold level, shows these two elements as the formation wide geochemical invariants of the Sardhai Formation clays. This phosphorus uniformity confirms the presence of a uniformly distributed phosphate constituent throughout the Sardhai Formation clay, directly analogous to the systematic trace element geochemistry documented by Abubakar et al., (2024) for phosphate bearing Pakistani sedimentary sequences in Abbottabad, where phosphate controlled distributions provided the geochemical baseline upon which spatial wide lead, chromium, and zinc anomalies were detected, which is being a parallel directly replicated in the present dataset by the contrast between the formation uniform phosphorus signal and the heterogeneous lead, chromium, and zinc distributions across the 22 Sardhai Formation samples, where lead is BDL in 17 of 22 samples yet reaches 0.470 ppm in US1, 0.365 ppm in US2, and 0.655 ppm in US21, and chromium ranges from BDL across all oxidized samples to 0.746 ppm in US2.

The structural context of the Sardhai Formation, hosted within the Salt Range provides the tectonic framework necessary to explain the most anomalous geochemical observation in the entire dataset, the multi-element enrichment in US21, which simultaneously carries silver (1.238 ppm), bismuth (0.411 ppm), gold (0.133 ppm), palladium (~1.980 ppm), copper (0.894 ppm), lead (0.655 ppm), zinc (2.536 ppm), barium (3.472 ppm), lanthanum (1.387 ppm), and cerium (4.884 ppm), while simultaneously showing ADL readings for both vanadium and manganese within the same sedimentary clay unit that yields far lower concentrations of these elements at all other sample positions, still the above mentioned ppm values for US21 are of a non-economical nature. Sherkati et al., (2006) demonstrated in the Zagros fold-and-thrust belt that deformation induced fracturing significantly modifies the permeability architecture of clay rich strata, enabling the migration of mineralizing basinal fluids and generating geochemical heterogeneity within originally uniform sedimentary units, which is precisely the mechanism that most plausibly explains the US21 multi-element anomaly as a localized horizon within the Sardhai Formation clay that is intersected influenced by a structurally controlled fluid conduit that has concentrated

a diverse suite of critical minerals at levels anomalous relative to all other sample positions in the same formation.

The enrichment of nickel (0.420 ppm), chromium (0.623 ppm), copper (0.894 ppm), and zinc (2.536 ppm) in US21 alongside rare earth minerals and precious metals is broadly consistent with the style of multi element geochemical anomalism associated with mineralized zones in Pakistani sedimentary and basement sequences as documented by Shah et al., (2020), while the precious metal signature in the form of silver at 1.238 ppm, gold at 0.133 ppm, and bismuth at 0.411 ppm distinguishes US21 as a complex polymetallic enrichment horizon that goes beyond the simpler base metal enrichment documented in comparable settings. The broader geochemical context of the Sardhai Formation is supported by the work of Zeb et al., (2020) on the Chichali Formation in the Kohat sub-basin of Khyber Pakhtunkhwa, whose major and trace element geochemistry established a baseline framework for Pakistani sedimentary sequences that which the present Sardhai Formation study both parallels and extends. Particularly in the demonstration that within a single Pakistani sedimentary formation, co-occurring enrichments in different element suites at different sample positions reflect the combined influence of sedimentary depositional history and most importantly the post depositional fluid overprinting.

The findings of Khan et al., (2023) that coal bearing strata in Khyber Pakhtunkhwa contain elevated critical mineral concentrations hosted predominantly in clay minerals, above world average values are further on extended by the present study to an Early Permian, confirming that clay mineral hosted critical mineral enrichment is a broadly operating geochemical phenomenon across Pakistani sedimentary sequences of diverse age and depositional setting. The critical mineral potential of the Sardhai Formation reflects the same fundamental clay mineral adsorption and lattice substitution mechanisms identified by Khan et al., (2023) in a different sedimentary context.

The mineral systems framework advocated by McCuaig and Hronsky (2014), which integrates source, transport pathways, depositional traps, and preservation as a

system provides the most coherent conceptual architecture for synthesizing all these observations within the context of a single sedimentary clay formation, the source component is confirmed as shared and uniform across all 22 samples by the invariant uranium and phosphorus concentrations, the transport component is expressed by the redox driven critical mineral redistribution between the oxidized and non-oxidized clay horizons of the same formation, the depositional trap component is most dramatically expressed at US21 as a structurally focused multi-element concentration horizon where critical minerals including silver, copper, zinc, lead, bismuth, and multiple rare earth elements simultaneously reach their highest concentrations in the dataset and lastly the preservation component is systematically governed by oxidation state with the non-oxidised samples preserving the formation's full critical and rare earth mineral inventory while the oxidized samples (US7, US8, US10, US11, US13, US18, US19) show pervasive BDL and near-BDL values for chromium, niobium, beryllium, gallium, nickel, lanthanum, neodymium, yttrium, and scandium. Collectively pointing to the non-oxidized sample positions within the Sardhai Formation as the most geochemically prospective horizons for critical minerals within this Early Permian sedimentary clay unit of the Nilawahan Group.

Based on the present dataset, the Sardhai Formation does not exhibit economic mineralization of critical minerals. It does, however, display detectable, localized intra-formational enrichment anomalies, which contribute to a clearer understanding of trace element behavior within clay dominated successions and offer a foundation for more detailed follow up work. As such, this study advances the geochemical characterization of the Sardhai Formation, while its implications for resource potential remain preliminary and non-economical and should be substantiated through additional sampling, mineralogical characterization, and economic screening.

CONCLUSIONS

The ICP-MS geochemical analysis of the Sardhai Formation clay samples confirms that this Early Permian sedimentary unit of the Nilawahan Group hosts a detectable, analytically meaningful suite of critical minerals, whose distribution is governed primarily by post depositional oxidation state and structurally driven fluid rock interaction rather than by any primary lithological variation. Among the critical minerals analyzed, manganese (mean 2.19484 ppm), vanadium (mean 1.06501 ppm), and the light rare earth elements (mean 0.56496 ppm), particularly cerium (mean 0.81808 ppm), lanthanum (mean 0.63518 ppm), neodymium (mean 0.53616 ppm), and praseodymium (mean 0.66138 ppm), together with titanium (mean 0.35212 ppm) and uranium (mean 0.28650 ppm), return the highest and most consistently quantifiable concentrations in the dataset. These elements also display the clearest oxidation-controlled signal, with non-oxidized samples retaining markedly higher concentrations than their oxidized counterparts, in some cases by more than an order of magnitude for light REEs. Lithium (mean 0.26398 ppm), while present at comparatively lower concentrations, shows this same pattern with notable consistency across the suite and remains strategically relevant given its critical mineral status. Beryllium (mean 0.04840 ppm), nickel (mean 0.11183 ppm), niobium (mean 0.07946 ppm), and zirconium (mean 0.03512 ppm) exhibit the same relative depletion under oxidation, though only at trace levels, zinc (mean 0.64951 ppm) by contrast, shows an inverse trend, with mildly elevated concentrations in the oxidized subgroup. Sample US21 stands out as a multi element, REE enriched anomaly within the formation, with its manganese and vanadium values themselves exceeding the upper limit of instrumental quantification, a further indication of its anomalous character. Taken together, these results affirm the capacity of fine grained Early Permian clay units of the Salt Range to act as repositories of critical minerals, while the overall low absolute concentrations recorded place these findings firmly at a reconnaissance level, they do not, on their own, indicate economic mineralization and should be treated as a preliminary baseline. Subsequent work should therefore prioritize focused examination of the non-oxidized horizons of the Sardhai Formation.

RECOMMENDATIONS

Future work should expand sampling beyond the present 22 specimens to additional Sardhai Formation exposures, targeting fresh, non-oxidized horizons and densifying coverage around the US21 anomaly to confirm whether it reflects a localized anomaly or a broader trend. Samples taken in future can be re-evaluated using a different digestion technique like the “four acid total digestion” so elements strongly bounded within silicate lattices can be recovered, and they can be further cross checked with XRF and ICP-OES, to obtain properly quantified concentrations for these major and abundant elements.

Clay mineralogy should be resolved through XRD and SEM-EDS to identify the dominant phases (illite, smectite, kaolinite, or mixed-layer assemblages) and their textural relationship to trace metal hosting, while electron microprobe analysis could pinpoint the specific mineral sites at which critical elements reside.

Sr, S, and Pb isotopic analysis can be done to determine whether enrichment is diagenetic in origin or driven by externally sourced, fault focused fluids. Structural mapping of fracture and fault density across the outcrop should be paired with this geochemical and mineralogical work to test the proposed fluid-pathway control directly.

In summary, no determination of economic viability can be made until further data establish adequate grade, tonnage, spatial continuity, and mineral recoverability, together with a reasonable prospect of economic extraction, in conformity with established mineral resource reporting standards.

REFERENCES

Abubakar, M., Khan, S., & Azeem, M. (2024). Economic potential and health risks assessment of the trace elements in the recently discovered phosphate deposits of Paswal Mian, Banseri, and Shahkot Regions, Abbottabad, Khyber Pakhtunkhwa, Pakistan. Geologica, 7(2).

Ahmad, S., 2003. A comparative study of structural styles in the Kohat Plateau, Northwest Himalayas, NWFP, Pakistan. Unpublished Ph.D. Thesis, NCE in Geology, University of Peshawar.

Ahmad, S., Ullah, M., Ullah, S., Khan, S., Khan, Y., Jan, I. U., Rehman, K., Mohibullah, M., Attaullah, & Jan, S. (2018). Stratigraphic and paleoclimatic reconstruction of the Upper Carboniferous–Lower Permian strata from the southern Gondwanaland remnants in Pakistan. Stratigraphy, 15(2), 69–90.

Ammann, A. A. (2007). Inductively coupled plasma mass spectrometry (ICP MS): A versatile tool. Journal of Mass Spectrometry, 42(4), 419–427.

Asrarullah, P. (1967). Geology of the Khewra Dome. In Proceedings of the 18th and 19th combined session of All Pakistan Science Conference, University of Sind, Hyderabad, Part-III, Abstracts, F3-F4.

Baker, D.M., Lillie, R.J., Yeats, R.S., Johnson, G.D., Yousuf, M., and Zamin, A.S.H. (1988). Development of the Himalayan frontal thrust zone: Salt Range, Pakistan. Geology, 16(1), 3-7.

Balaram, V. (2021). Current and emerging analytical techniques for geochemical and geochronological studies. Geological Journal, 56(5), 2300–2359.

Benson, T. R., Coble, M. A., & Dilles, J. H. (2023). Hydrothermal enrichment of lithium in intracaldera illite-bearing claystones. Science Advances, 9(35), eadh8183.

Binnemans, K., Jones, P. T., Blanpain, B., Van Gerven, T., Yang, Y., Walton, A., & Buchert, M. (2013). Recycling of rare earths: A critical review. Journal of Cleaner Production, 51, 1–22.

Blisniuk, P. M. (1996). Tectonic Evolution of the NW-Himalayan Thrust Front: The Trans-Indus Ranges, Northern Pakistan. Dartmouth College.

Chi, R., & Tian, J. (2011). Weathered crust elution-deposited rare earth ores. Nova Science Publishers.

Coward, M. P., Rex, D. C., Asif Khan, M., Windley, B. F., Broughton, R. D., Luff, I. W., ... & Pudsey, C. J. (1986). Collision tectonics in the NW Himalayas. Geological Society, London, Special Publications, 19(1), 203-219.

Davies, L.M., and Pinfold, E.S. (1937). The Eocene beds of the Punjab Salt Range. Geological Survey of India Memoir, Palaeontologia Indica, New Series, 24.

Duncan, R. A., & Pyle, D. G. (1988). Rapid eruption of the Deccan flood basalts at the Cretaceous/Tertiary boundary. Nature, 333(6176), 841-843.

European Commission. (2020). Critical raw materials resilience: Charting a path towards greater security and sustainability (COM (2020) 474 final).

European Commission. (2023). Critical raw materials act: Commission proposes measures to ensure EU access to secure, diversified, affordable and sustainable supply of critical raw materials.

European Parliament. (2024). Regulation of the European Parliament and of the Council establishing a framework for ensuring a secure and sustainable supply of critical raw materials (Critical Raw Materials Act).

Executive Office of the President. (2017). A federal strategy to ensure secure and reliable supplies of critical minerals (Executive Order 13817). Federal Register, 82(246), 60835–60837.

Farah, A., Mirza, M. A., Ahmad, M. A., & Butt, M. H. (1977). Gravity field of the buried shield in the Punjab Plain, Pakistan. Geological Society of America Bulletin, 88(8), 1147-1155.

Fatmi, A.N. (1973). Lithostratigraphic units of Kohat-Potwar Province, Indus basin. Geological Survey of Pakistan Memoirs, 10.

Gansser, A. (1964). Geologic and tectonic maps of the Himalayan region.

Gaudino, S., Galas, C., Belli, M., Barbizzi, S., de Zorzi, P., Jaćimović, R., Jeran, Z., Pati, A., & Sansone, U. (2007). The role of different soil sample digestion methods on trace elements analysis: A comparison of ICP-MS and INAA measurement results. Accreditation and Quality Assurance, 12(2), 84–93.

Gee, E. R. (1964). Indus Basin Stratigraphy. Records of the Geological Survey of Pakistan.

Gee, E. R. (1989). Overview of the geology and structure of the Salt Range, with observations on related areas of northern Pakistan. Geological Society of America Special Paper, 232, 95–112.

Gee, E.R. (1945). The age of the Saline Series of the Punjab and of Kohat. Proceedings of the National Academy of Sciences, India, Section B, 14, 269-311.

Gee, E.R. (1947). Further note on the age of the Saline Series of the Punjab and of Kohat. Proceedings of the National Academy of Sciences, India, Section B, 16, 95-154.

Gee, E.R. (1980). Pakistan geological Salt Range Series. Directorate of Overseas Surveys, United Kingdom, for the Government of Pakistan and Geological Survey of Pakistan, 6 sheets, scale 1:50,000.

Gee, E.R. (1983). Tectonic problems of the Sub-Himalayan region of Pakistan. Kashmir Journal of Geology, 1, 11-18.

Ghazi, S., Ali, S. H., Sahraeyan, M., & Hanif, T. (2015). An overview of tectonosedimentary framework of the Salt Range, northwestern Himalayan fold and thrust belt, Pakistan. *Arabian Journal of Geosciences*, *8*(3), 1635-1651.

Ghazi, S., et al. (2020). Neogene kinematics of the Potwar Plateau and the Salt Range, NW Himalayan Front: A paleostress inversion and AMS study. Journal of Asian Earth Sciences.

Graedel, T. E., Harper, E. M., Nassar, N. T., Nuss, P., & Reck, B. K. (2015). Criticality of metals and metalloids. Proceedings of the National Academy of Sciences, 112(14), 4257–4262.

Grelaud, S., Sassi, W., de Lamotte, D. F., Jaswal, T., & Roure, F. (2003). Kinematics of eastern Salt Range and South Potwar Basin (Pakistan): A new scenario. Marine and Petroleum Geology, 19(9), 1127–1139.

Harben, P. W. (2002). The industrial minerals handybook: A guide to markets, specifications and prices (4th ed.). Industrial Minerals Information.

Hatch, J. R., & Leventhal, J. S. (1992). Relationship between inferred redox potential of the depositional environment and geochemistry of the Upper Pennsylvanian Stark Shale. Chemical Geology, 99, 65–82.

Hemphill, W. R., & Kidwai, A. H. (1973). Stratigraphy of the Bannu and Dera Ismail Khan areas, Pakistan (No. 716-B).

Hitzman, M. W., Selley, D., & Bull, S. (2010). Formation of sedimentary rock-hosted stratiform copper deposits through Earth history. Economic Geology, 105(3), 627–639.

Houk, R. S., Fassel, V. A., Flesch, G. D., Svec, H. J., Gray, A. L., & Taylor, C. E. (1980). Inductively coupled argon plasma as an ion source for mass spectrometric determination of trace elements. Analytical Chemistry, 52(14), 2283–2289.

International Energy Agency. (2021). The role of critical minerals in clean energy transitions. IEA Publications.

Johnson, G. D., Raynolds, R. G., & Burbank, D. W. (1986). Late Cenozoic tectonics and sedimentation in the north-western Himalayan foredeep: I. Thrust ramping and associated deformation in the Potwar region. Foreland basins, 273-291. Journal of Geosciences, 8(3), 1635-1651.

Kashani, A., & Mostaghimi, J. (2010). Aerosol characterization of concentric pneumatic nebulizer used in inductively coupled plasma—Mass spectrometry (ICP-MS). Atomization and Sprays, 20(5).

Kazmi, A. H., & Jan, M. Q. (1997). Geology and tectonics of Pakistan. (No Title).

Khan, M., Ali, L., Hussain, R., Khan, S., Khattak, S. A., & Ahmad, S. R. (2023). Geochemical investigation and modes of occurrence of critical elements and minerals

in the coal of Akkakhel, Akhorwal, and Sheikhan, KP, Pakistan. Episodes Journal of International Geoscience, 46(2), 177-194.

Khwaja, A. A., & Lisa, M. (2005). Seismic activity in the western extension of Salt Range. Pakistan Journal of Meteorology, 2(3), 35-39.

Leventhal, J. S. (1991). Organic matter and metal enrichment in black shales. U.S. Geological Survey Bulletin.

Lillie, R.J., Johnson, G.D., Yousuf, M., Zamin, A.S.H., and Yeats, R.S. (1987). Structural development within the Himalayan foreland fold-and-thrust belt of Pakistan. In C. Beaumont and A.J. Tankard (Eds.), Sedimentary basins and basin forming mechanisms (pp. 379-392). Canadian Society of Petroleum Geologists Memoir 12.

Linge, K. (2024). Quadrupole inductively coupled plasma-mass spectrometry. In GGR Handbook of Rock and Mineral Analysis (Chapter 7). Geostandards and Geoanalytical Research.

McCuaig, T. C., & Hronsky, J. M. A. (2014). The mineral system concept: The key to exploration targeting. Society of Economic Geologists Special Publication, 18, 153–175.

McDougall, J. W., & Khan, S. H. (1990). Strike-slip faulting in a foreland fold-thrust belt: The Kalabagh Fault and Western Salt Range, Pakistan. Tectonics, 9(5), 1061-1075.

Mertmann, D. (2003). Evolution of the marine Permian carbonate platform in the Salt Range (Pakistan). Palaeogeography, Palaeoclimatology, Palaeoecology, 191(3–4), 373–384.

Noetling, P. (1901). Beitrage zur Geologie der Salt Range, insbesondere der permichen und triasuchen Ablagerungen. Neues Jahrbuch für Mineralogie, Beilage Band, 14, 369-471.

Nriagu, J. O. (Ed.). (1998). Thallium in the environment. Wiley.

Patriat, P., & Achache, J. (1984). India–Eurasia collision chronology has implications for crustal shortening and driving mechanism of plates. Nature, 311(5987), 615-621.

Petterson, M. G., & Windley, B. F. (1985). RbSr dating of the Kohistan arc-batholith in the Trans-Himalaya of north Pakistan, and tectonic implications. Earth and Planetary Science Letters, 74(1), 45-57.

Powell, C. M. (1979). A speculative tectonic history of Pakistan and surroundings. Geodynamics of Pakistan.

Qureshi, M. K. A. (1980). Copper showing in Warchha Sandstone and Sardhai Formation, Salt Range. Contributions to the Geology of Pakistan, 61–87.

Robinson, P. (2025). Analysis of geological materials 1: Sample preparation methods. In GGR Handbook of Rock and Mineral Analysis (Chapter 2, Part 1). Geostandards and Geoanalytical Research.

Rowley, D. B. (1996). Age of initiation of collision between India and Asia: A review of stratigraphic data. Earth and Planetary Science Letters, 145(1-4), 1-13.

Sader, J. A., & Ryan, S. (2020). Advances in ICP-MS technology and the application of multi-element geochemistry to exploration. Geochemistry: Exploration, Environment, Analysis, 20(2), 167–175.

Schönbächler, M. (2016). Inductively coupled plasma mass spectrometry (ICP-MS). In W. White (Ed.), Encyclopedia of geochemistry. Springer

Schrijvers, D., Hool, A., Blengini, G. A., Chen, W. Q., Dewulf, J., Eggert, R., van Ellen, L., Gauss, R., Goddin, J., Habib, K., Hagelüken, C., Hokka, A., Huisman, J., Jamieson, H. E., Mao, J., McLellan, B., Nansai, K., Nassarr, N., Sykes, D., & Sonnemann, G. (2020). A review of methods and data to determine raw material criticality. Resources, Conservation and Recycling, 155, 104617.

Searle, M. P. (1991). Geology and tectonics of the Karakoram Mountains. (No Title).

Shah, A., Haneef, M., Hanif, M., & Jan, I. U. (2012). Lithofacies and palaeoenvironments of the Carboniferous-Permian Nilawahan Group, Salt Range Pakistan. J. Himal. Earth Sci, 45, 136.

Shah, S. M. I. (1977). Stratigraphy of Pakistan (Memoir 12). Geological Survey of Pakistan.

Shah, S. T. H., Qaiser, F. U. R., Khan, N. G., Mir, T., Jabir, M., Akram, W., & Muneeb ur-Rehman, M. (2020). Magnetic prospecting and geochemical analysis for the mineral exploration of Mali-Dera deposits, Kohistan Island ArcPakistan. Environmental Earth Sciences, 79(18), 406.

Sherkati, S., Letouzey, J., & Frizon de Lamotte, D. (2006). Central Zagros fold-thrust belt (Iran): New insights from seismic data and field observations. Tectonics, 25, TC4007.

Shimadzu Corporation. (2024). What is ICP-MS (inductively coupled plasma mass spectrometry).

Singh, T. (1987). Permian biogeography of the Indian subcontinent with special reference to marine fauna. In G. D. McKenzie (Ed.), Gondwana six: Stratigraphy, sedimentology, and paleontology (Geophysical Monograph 41, pp. 239–249). American Geophysical Union.

Tahirkheli, R. K. (1979). Geology of Kohistan and Adjacent Eurasian and Indo-Pakistan Continents, Pakistan. Journal of Himalayan Earth Sciences, 11(1), 1-30.

Thomas, R. (2013). Practical guide to ICP-MS: A tutorial for beginners (3rd ed.). CRC Press.

Treloar, P. J., & Izatt, C. N. (1993). Tectonics of the Himalayan collision between the Indian plate and the Afghan block: A synthesis. Geological Society, London, Special Publications, 74(1), 69-87.

Trusheim, F. (1960). Mechanism of salt migration in northern Germany. AAPG Bulletin, 44(9), 1519-1540.

U.S. Congress. (2020). Energy Act of 2020 (Pub. L. No. 116–260, Division Z).

U.S. Department of Energy. (2023). Critical materials assessment. Office of Energy Efficiency and Renewable Energy.

U.S. Geological Survey. (2022). 2022 final list of critical minerals. U.S. Department of the Interior.

U.S. Geological Survey. (2025). About the 2025 list of critical minerals. U.S. Department of the Interior.

Ullah, Z., Li, J. W., Robinson, P. T., Wu, W. W., Khan, A., Dac, N. X., & Adam, M. M. A. (2020). Mineralogy and geochemistry of peridotites and chromitites in the Jijal Complex ophiolite along the Main Mantle Thrust (MMT or Indus Suture Zone) North Pakistan. Lithos, 366, 105566.

Veevers, J. J., & Tewari, R. C. (1995). Gondwana master basin of Peninsular India between Tethys and the interior of the Gondwanaland Province of Pangea (Memoir 187). Geological Society of America.

Wardlaw, B. R., & Pogue, K. R. (1995). The Permian of Pakistan. In P. A. Scholle, T. M. Peryt, & D. S. Ulmer-Scholle (Eds.), The Permian of Northern Pangea (Vol. 2, pp. 215–224). Springer-Verlag.

World Bank. (2020). Minerals for climate action: The mineral intensity of the clean energy transition. World Bank Group.

World Steel Association. (2024). Steel Statistical Yearbook 2024.

Wynne, A. B. (1878). Notes on the Physical Geology of the Upper Punjáb. Quarterly Journal of the Geological Society, 34(1-4), 347-376.

Yeats, R. S., & Hussain, A. (1987). Timing of structural events in the Himalayan foothills of northwestern Pakistan. Geological society of America bulletin, 99(2), 161-176.

Yeats, R. S., Hussain, A., & Khan, S. H. (1984). Late Quaternary deformation of the Salt Range of Pakistan. Geological Society of America Bulletin, 95(8), 958–966.

Zeb, S. F., Zafar, M., Jehandad, S., et al. (2020). Integrated geochemical study of Chichali Formation from Kohat sub-basin, Khyber Pakhtunkhwa, Pakistan. Journal of Petroleum Exploration and Production Technology, 10(5), 2127-2144.

Zhang, W., & Hu, Z. (2019). Recent advances in sample preparation methods for elemental and isotopic analysis of geological samples. Spectrochimica Acta Part B: Atomic Spectroscopy, 160, 105690.

Umar MS Thesis

ORIGINALITY REPORT

7%	4%	4%	4%
SIMILARITY INDEX	INTERNET SOURCES	PUBLICATIONS	STUDENT PAPERS

PRIMARY SOURCES

1	Submitted to Higher Education Commission Pakistan Student Paper	3%
2	idoc.pub Internet Source	1%
3	www.econ-environ-geol.org Internet Source	1%
4	Natalia Yakovleva, Edmund Nickless. "Routledge Handbook of the Extractive Industries and Sustainable Development", Routledge, 2022 Publication	<1%
5	Gee, E. R., and D. G. Gee. "Overview of the geology and structure of the Salt Range, with observations on related areas of northern Pakistan", Geological Society of America Special Papers, 1989. Publication	<1%
6	Muhammad Yaseen, Sohail Wahid, Sajjad Ahmad, Gohar Rehman, Jawad Ahmad, Muhammad Naveed Anjum, Mubashir Mehmood. "Tectonic evolution, prospectivity and structural studies of the hanging wall of Main Boundary Thrust along Akhurwal-Kohat transect, Khyber Pakhtunkhwa: implications for future exploration", Arabian Journal of Geosciences, 2021 Publication	<1%

7	pl.boell.org Internet Source	<1 %
8	SHAHID GHAZI, NIGEL P MOUNTNEY, AFTAB AHMAD BUTT, SADAF SHARIF. "Stratigraphic and palaeoenvironmental framework of the Early Permian sequence in the Salt Range, Pakistan", Journal of Earth System Science, 2012 Publication	<1 %
9	Zaheen Ullah, Asad Khan, Shah Faisal, Tehseen Zafar, Huan Li, Muhammad Farhan. "Petrogenesis of peridotites in the Dargai Complex ophiolite, Indus Suture Zone, Northern Pakistan: Implications for two stages of melting, depletion, and enrichment of the Neo-Tethyan mantle", Lithos, 2022 Publication	<1 %
10	www3.open.ac.uk Internet Source	<1 %
11	J. AFZAL, M. WILLIAMS, R. J. ALDRIDGE. "Revised stratigraphy of the lower Cenozoic succession of the Greater Indus Basin in Pakistan", Journal of Micropalaeontology, 2009 Publication	<1 %
12	Submitted to National University of Singapore Student Paper	<1 %
13	blogs.edf.org Internet Source	<1 %
14	Syed Tallataf Hussain Shah, Arsalan Iftikhar, Syed Mohib Ali, Umair Inayat et al. "Evaluating Chromite Ore Deposits: An Integrated Magnetic and Geochemical Study in the	<1 %

	Kohistan Island Arc of Northern Pakistan", Physics and Chemistry of the Earth, Parts A/B/C, 2025 Publication	
15	Yin, A.. "Cenozoic tectonic evolution of the Himalayan orogen as constrained by along-strike variation of structural geometry, exhumation history, and foreland sedimentation", Earth Science Reviews, 200605 Publication	<1 %
16	www.doi.gov Internet Source	<1 %
17	Submitted to University of Reading Student Paper	<1 %
18	G Mahéo, S Guillot, J Blichert-Toft, Y Rolland, A Pêcher. "A slab breakoff model for the Neogene thermal evolution of South Karakorum and South Tibet", Earth and Planetary Science Letters, 2002 Publication	<1 %
19	www.science.gov Internet Source	<1 %
20	Ishtiaq A. K. Jadoon, Matthias Hinderer, Allah B. Kausar, Aziz A. Qureshi, Mirza S. Baig, Mohammad Basharat, Wolfgang Frisch. "Structural interpretation and geo-hazard assessment of a locking line: 2005 Kashmir earthquake, western Himalayas", Environmental Earth Sciences, 2014 Publication	<1 %
21	lobbymap.org Internet Source	<1 %

22	new.ijges.com Internet Source	<1%
23	prnigeria.com Internet Source	<1%
24	pubs.usgs.gov Internet Source	<1%
25	springboardatlantic.ca Internet Source	<1%
26	Khan, Muhammad Tufail. "Sedimentology and Biostratigraphy of the Chorgali Formation, Potwar and Hazara Sub-Basins, Upper Indus Basin of Pakistan: Implications for the Closing Stage of the Eastern Neo-Tethys Ocean", The University of Regina (Canada), 2023 Publication	<1%
27	chimatbera.web.app Internet Source	<1%
28	cleantechctv.com Internet Source	<1%
29	irlib.ambou.edu.et Internet Source	<1%
30	nanopdf.com Internet Source	<1%
31	Perkins, R.B.. "Trace-element budgets in the Ohio/Sunbury shales of Kentucky: Constraints on ocean circulation and primary productivity in the Devonian-Mississippian Appalachian Basin", Palaeogeography, Palaeoclimatology, Palaeoecology, 20080731 Publication	<1%

32	Jabir Hussain, Mumtaz Ali Khan, Ahmed E. Radwan, Tassawar Hayat. "Depositional and diagenetic evolution of the lower eocene homoclinic-ramp carbonates (a paradigm from the Salt Range, Pakistan): Sequence stratigraphic, petrographical, diagenetic, and geochemical attributes", Marine and Petroleum Geology, 2025 Publication	<1%

Exclude quotes	Off	Exclude matches	Off
Exclude bibliography	Off		